

UNIVERSITÀ DI PISA

Scuola di Dottorato in Ingegneria “Leonardo da Vinci”



Corso di Dottorato di Ricerca in
INGEGNERIA DELL'INFORMAZIONE

Tesi di Dottorato di Ricerca

Enhancements of MEMS design flow for Automotive and Optoelectronic applications

Autore:

Eleonora Marchetti _____

Relatori:

Prof. Luca Fanucci _____

Prof. Roberto Saletti _____

Anno 2010

Ai miei genitori

ACKNOWLEDGMENTS

I am a lucky woman, many are the people which have supported me during my course of study and during the three years of my PhD, but I have no doubt about which are the first two person whose I want to say thank you, my parents, because after many years of studies they are yet the “best teachers” that I have never had.

A big thank you is for the rest of my family, my wonderful sister Laura and her husband Michele which have always supported me and believed in me.

And a not smaller thank you is for another very important person in my life: Francesco which has constantly followed me during these years with his love and especially with his patient.

I would like also say thank you to the best friend that I have never had, Manuela for her friendship, complicity and constant support.

Then my gratitude goes to my tutors Prof. Luca Fanucci and Prof. Roberto Saletti both for their precious technical help, for the several chances of professional improving they provided to me, and their friendship.

A special thank goes to the SensorDynamics AG design centre of Navacchio (with particular appreciation to the R&D team and the evaluation team), the people working there taught me what is commitment and professionalism, but I can consider them as good friends too.

And a finally thank is for the research center Fraunhofer Institute for Silicon Technology where I have found several chances to improve my work.

ABSTRACT

In the latest years we have been witnesses of a very rapidly and amazing grown of MicroElectroMechanical systems (MEMS) which nowadays represent the outstanding state-of-the art in a wide variety of applications from automotive to commercial, biomedical and optical (MicroOptoElectroMechanicalSystems).

The increasing success of MEMS is found in their high miniaturization capability, thus allowing an easy integration with electronic circuits, their low manufacturing costs (that comes directly from low unit pricing and indirectly from cutting service and maintaining costs) and low power consumption.

With the always growing interest around MEMS devices the necessity arises for MEMS designers to define a MEMS design flow. Indeed it is widely accepted that in any complex engineering design process, a well defined and documented design flow or procedure is vital.

The top-level goal of a MEMS/MOEMS design flow is to enable complex engineering design in the shortest time and with the lowest number of fabrication iterations, preferably only one. These two characteristics are the measures of a good flow, because they translate directly to the industry-desirable reductions of the metrics “time to market” and “costs”.

Like most engineering flows, the MEMS design flow begins with the product definition that generally involves a feasibility study and the elaboration of the device specifications. Once the MEMS specifications are set, a Finite Element Method (FEM) model is developed in order to study its physical behaviour and to extract the characteristic device parameters. These latter are used to develop a high level MEMS model which is necessary to the design of the sensor read out electronics. Once the MEMS geometry is completely defined and matches the device specifications, the device layout must be generated, and finally the MEMS sensor is fabricated.

In order to have a MEMS sensor working according to specifications at first production run is essential that the MEMS design flow is as close as possible to the optimum design flow.

The key factors in the MEMS design flow are the development of a sensor model as close as possible to the real device and the layout realization. This research work addresses these two aspects by developing optimized custom tools (a tool for layout check (LVS) and a tool for parasitic capacitances extraction) and new methodologies (a methodology for post layout simulations) which support the designer during the crucial steps of the design process as well as by presenting the models of two cases studies belonging to leading MEMS applications (a micromirror for laser projection system and a control loop for the shock immunity enhancement in gyroscopes for automotive applications).

SOMMARIO

Negli ultimi anni abbiamo assistito ad una crescita rapida e sorprendente dei dispositivi MicroElettroMeccanici al punto che oggi rappresentano il più avanzato stato dell'arte in una grande varietà di applicazioni che spaziano dal campo automotive, a quello consumer, fino ad arrivare a quello biomedico ed ottico (Sistemi MicroOptoElettroMeccanici).

Il sempre crescente successo dei MEMS è dovuto essenzialmente a tre fattori: elevata capacità di miniaturizzazione (che permette una facile integrazione con i circuiti elettronici integrati), basso costo di fabbricazione (che deriva direttamente dal basso costo del singolo dispositivo ed indirettamente dall'ammortizzazione dei costi per ampi volumi di produzione) e basso consumo di potenza.

Dall'interesse sempre crescente attorno ai dispositivi MEMS nasce la necessità di definire in modo preciso il flusso di progetto di un MEMS. Infatti è noto che per un qualsiasi progetto nel campo dell'ingegneria l'esistenza di un flusso o una procedura ben definite e documentate è vitale per il buon esito del progetto stesso. L'obiettivo principale della definizione del flusso di progetto di un dispositivo MEMS/MOEMS è fornire al progettista gli strumenti e le linee guida necessarie per realizzare il progetto del dispositivo nel minore tempo possibile e con il minor numero di cicli di fabbricazione possibile, preferibilmente uno solo. Queste due caratteristiche definiscono un buon flusso di progetto perché si traducono direttamente in una riduzione dei costi di produzione e del tempo che il nuovo dispositivo impiega ad uscire sul mercato (time to market).

Come la maggior parte dei flussi di progetto anche quello di un dispositivo MEMS inizia con la definizione del prodotto che generalmente comprende uno studio di fattibilità e l'elaborazione delle specifiche del dispositivo. Una volta che tali specifiche sono state definite, si passa alla messa a punto di un modello ad elementi finiti (FEM) utilizzato per studiare la fisica del dispositivo e per estrarre i parametri caratteristici dello stesso. Questi ultimi saranno poi utilizzati per sviluppare un modello ad alto livello del MEMS che è fondamentale per la progettazione dell'interfaccia elettronica di lettura e condizionamento del dispositivo. Una volta che la geometria del MEMS è completamente definita ed è compatibile con le specifiche del dispositivo, si passa alla realizzazione del layout dello stesso ed infine alla fabbricazione del MEMS.

Per avere un sensore MEMS funzionante in accordo con le specifiche di progetto al primo ciclo di produzione, è essenziale che il flusso di progetto del MEMS sia il più vicino possibile al flusso di progetto ottimo.

I fattori chiave nel flusso di progetto di un MEMS sono lo sviluppo di un modello il più vicino possibile al dispositivo reale e la realizzazione del layout del dispositivo. Il lavoro di ricerca presentato in questa tesi affronta proprio questi due aspetti sia mediante lo sviluppo di tools e metodologie che supportino il progettista durante tutti i passi cruciali del progetto (saranno descritti lo sviluppo di un tool per effettuare il controllo del layout (LVS) e per l'estrazione delle capacità parassite del dispositivo insieme con una metodologia per effettuare simulazioni post layout), sia presentando i modelli sviluppati per due applicazioni leader nel campo dei dispositivi MEMS (un micro specchio per sistemi di proiezioni laser ed un anello di controllo per aumentare l'immunità ai disturbi nei giroscopi per applicazioni automotive).

CONTENTS

ACKNOWLEDGMENTS	- 5 -
ABSTRACT	I
SOMMARIO.....	III
CONTENTS.....	V
INTRODUCTION	VII
CHAPTER 1	- 1 -
MEMS TECHNOLOGIES AND APPLICATIONS.....	- 1 -
1.1. MEMS historical background	- 2 -
1.2. MEMS fabrication and technologies	- 5 -
1.2.1. Silicon etching and bonding.....	- 6 -
1.2.2. Surface micromachining.....	- 10 -
1.2.3. Bulk micromachining.....	- 11 -
1.3. MEMS leading applications	- 13 -
1.3.1. MEMS for automotive applications	- 14 -
1.3.2. MEMS for optical (MOEMS)	- 19 -
CHAPTER 2	- 25 -
MEMS DESIGN FLOW	- 25 -
2.1. MEMS design flow structure.....	- 26 -
2.2. CAD tools for MEMS design	- 30 -
2.3. MEMS modelling	- 32 -
2.3.1. Finite Element Method for MEMS modelling.....	- 34 -
2.3.2. Behavioural modelling: Simulink™ tool.....	- 36 -
2.4. MEMS layout	- 37 -
2.5. Challenges in MEMS design.....	- 39 -
CHAPTER 3	- 41 -
AUTOMATIC TOOLS AND METHODOLOGIES FOR MEMS DESIGN FLOW ENHANCEMENT.....	- 41 -
3.1. ASSURA tools for MEMS LVS check and connectivity extraction..	- 42 -
3.1.1. ASSURA tool for MEMS LVS: working principle.....	- 42 -
3.1.2. ASSURA tool for MEMS LVS: rules file.....	- 44 -
3.1.3. ASSURA tool for connectivity extraction: working principle..	- 46 -
3.1.4. ASSURA tool for connectivity extraction: executable file.....	- 48 -
3.1.5. ASSURA tool for connectivity extraction: rules file	- 49 -
3.1.6. ASSURA tool for connectivity extraction: RSF file.....	- 50 -
3.2. Methodology for post layout ANSYS simulation	- 51 -
3.3. ASSURA tool for parasitic capacitances extraction.....	- 54 -
3.3.1. Shield parasitic capacitances.....	- 55 -

3.3.2.	Substrate parasitic capacitances	- 55 -
3.3.3.	Tool working principle	- 56 -
CHAPTER 4	- 57 -
MEMS SYSTEMS: CASE STUDIES	- 57 -
4.1.	<i>Micromirror for laser projection system</i>	- 58 -
4.1.1.	Micromirror working principle	- 59 -
4.1.2.	FEM simulations	- 60 -
4.1.3.	Simulink™ model	- 65 -
4.1.4.	Model integration	- 68 -
4.2.	<i>Immunity enhancement in gyroscope for automotive applications</i> -	70 -
4.2.1.	Micromachined gyroscope working principle	- 71 -
4.2.2.	Closed loop control for shock immunity enhancement	- 72 -
4.2.3.	Closed loop control implementation: Simulink™ model.....	- 76 -
4.2.4.	Closed loop control implementation: enhanced model	- 83 -
4.2.5.	Simulation results	- 84 -
CONCLUSIONS	- 90 -
BIBLIOGRAPHY	- 93 -

INTRODUCTION

MicroElectroMechanical Systems (MEMS) are a logical extension of microelectronic and integrated circuit technology. While integrated circuits developed in the early 1960s, a number of laboratories worked to use the same technology base to form integrated sensors. The original idea was to reduce costs and then put the sensor and circuits together on the same chip.

With the introduction of new techniques of silicon micro processing we assist to the MEMS born. Indeed MEMS devices and systems involve some form of lithography-based microfabrication borrowed from the microelectronic industry and enhanced with specialized techniques generally called “micromachining”.

In practice microsystems are embedded systems involving both electronic and non-electronic components and performing a variety of functions that can include signal acquisition and processing, actuation, display and control.

Beginning in the late 80s, MEMS received increasing emphasis worldwide and many governments heavily funded the development of MEMS technology, particularly the United States, Japan and Germany.

Today MEMS and MOEMS (which are MEMS systems with the addition of optoelectronic) devices represent the outstanding state of art for a broad range of applications such as biomedical, communication, automotive, commercial and optical.

A so high level of interest in MEMS technology comes from both business and technical directions. In fact they are attractive to business because multiple emerging markets for MEMS promise large financial gain and they are also attractive from a technological point of view. More in detail MEMS technical attractiveness include multiple factors: low power consumption, low manufacturing cost (due to both batch fabrication and the possibility to use the same infrastructure already created for integrated circuits) and high miniaturization capability thus allowing for an easy integration with electronic circuits.

With the always growing interest around MEMS devices arises the necessity for MEMS designers to define a dedicated MEMS design flow. Indeed it is widely accepted that in any complex engineering design process, a well defined and documented design flow or procedure is a must.

The top-level goal of a MEMS/MOEMS design flow is to enable complex engineering design in *as short time as possible* and with *as few fabrication iterations as possible*, preferably only one. These two factors are the measures of a good flow, because they translate directly to the industry-desirable reductions of the metrics “*time to market*” and “*costs*”.

Like most engineering flows, the MEMS design flow begins with a product definition. The definition is based on an idea as well as a general architecture and feasibility studies and involves the definition of the device specifications. Once the MEMS specifications are set, a Finite Element Method (FEM) model is developed in order to define the MEMS geometry and study its physical behaviour. FEM simulations are also performed to extract the characteristic device parameters used to develop a high level MEMS model. A high level MEMS model is necessary

because the MEMS and the sensor read out electronics cannot be designed independently. Modelling the interaction of the MEMS with the electronics is essential to predict the complete system behaviour, and hence compatible models of the sensor and the system must be developed.

Once the MEMS geometry is completely defined and matches the device specifications, the device layout must be generated. The layout is usually realized by employing the same tools used for the electronic circuit layouts. The realization of the layout is the last step before the production.

In order to reduce as much as possible production costs and time to market, it is fundamental to have an optimized design flow, this means having at the first production run a right MEMS sensor which matches design specifications.

Unfortunately in most cases this does not happen. Indeed in practice more runs are necessary to obtain a working sensor due to errors in the sensor layout and/or wrong approximations in FEM simulations, and this results in increasing production costs and development time.

In order to have a design flow as close as possible to the optimum one, two are the key factors: to *have a model as close as possible to the real device*, to perform the *layout verification and simulation*.

Layout verification is necessary to check the layout before the production, indeed DRC (Design Rules Check) and LVS (Layout Versus Schematic check) are fundamental to find errors before tape-out.

In the same way layout simulations are very useful to guarantee a successful MEMS design, since in simulating the layout the designer can often better determine the mechanical properties thus allowing a fine tuning of the system level sensor model.

Development of algorithms/tools for MEMS layout verification is an active area of research, but currently no-shelf tools are available, hence custom tools must be developed.

In the same way even if layout simulations (also called post layout simulations) are very important, a well define methodologies to perform post layout simulations in a quick and reliable way are missing.

From these issues the necessity arises to support the MEMS designer with proper design tools and guidelines in order to verify correctness of the layout and to perform post layout simulations.

This research work deals with two main topics: the first is the development of new methodologies and automatic tools to optimize a generic MEMS design flow, the second highlights the importance of modelling in MEMS systems development by detailing two important application studies such as a micromirror for laser projection systems and a closed loop control for gyroscopes employed in automotive.

Chapter 1 presents the MEMS technology by describing its historical development, the factors that have made of this technology the outstanding state-of-the-art in a wide range of applications, and the principal technological processes involved in MEMS fabrication. The chapter is then concluded by showing the principal applications of MEMS in two leading field: automotive and optics.

In Chapter 2 the focus is on MEMS design flow, a generic MEMS design flow is described together with the tools currently available to assist the designers during the design and development phases. While the principle steps of a MEMS design

flow are described the open issues and the principal challenges in MEMS design are discussed as well.

Chapter 3 presents a possible solution of these issues by the description of new tools and methodologies developed in this research work to enhance MEMS design flow and to reach the challenging goal of a right working MEMS at first production run.

Finally since MEMS modelling is fundamental in MEMS design flow, Chapter 4 is dedicated to modelling of MEMS and their conditioning systems by referring to two leading applications: a micromirror for laser projection system and a gyroscope for automotive applications. Indeed in this chapter two important application studies are described that show the importance of model at different design levels. The first is the model of a torsional micromirror for laser projection systems and its employment in the design of the MEMS read out stage, and the second is the model of a new control system for shock immunity enhancement in gyroscopes for automotive applications.

CHAPTER 1

MEMS TECHNOLOGIES AND APPLICATIONS

In Europe they are called “Microsystems”, in the United States and increasingly elsewhere they are called “MicroElectroMechanical Systems” or MEMS. Nowadays the acronym MEMS is well known and adopted all over the world.

From a literal analysis of the term “Microelectromechanical Systems”: “*micro*” establishes a dimensional scale, “*electro*” suggests electricity or electronics (or both), and finally “*mechanical*” suggests the presence of moving parts. But MEMS concept has grown to encompass many other types of small things, including thermal, magnetic, fluidic and optical devices and systems.

In practice Microsystems/MEMS are embedded systems involving both electronic and non-electronic components and performing different functions that can include signal acquisition and processing, actuation, display and control.

The miniaturisation of sensors and systems has been made possible by the advances in semiconductor industry and the emergent field of MEMS has grown very rapidly during the last 20 years. The increasing success of MEMS system is due to the fact that they integrate smaller function together into a package of greater utility (e.g. an acceleration sensor integrated together with the electronic circuit for self-diagnostic) and they also bring cost benefits directly through low unit pricing or indirectly by cutting service and maintaining costs.

The emphasis in MEMS devices should be taken on “system” aspect, they are true systems in the sense that different components are integrated together to perform function of more and more increasing complexity. In fact building Microsystems is an evolutionary process, one notable example to support this assertion is the evolution of “crash sensors” for airbag safety systems. Early sensors were merely mechanical switches then they later evolved into micromechanical sensors that directly measured acceleration. The current generation of devices integrates electronic circuitry alongside a micromechanical sensor to provide self diagnostics and a digital output. It is anticipated that the next generation of devices will also incorporate the entire airbag deployment circuitry that decides whether to inflate the airbag. As the technology matures, the airbag crash sensor may be integrated one day with micromachined yaw-rate and other inertial sensors to form a complete microsystem responsible for passenger safety and vehicle stability.

In practice the great advantage of a MEMS solution is not the size reduction but is the chance to enable new functions and to have significant cost reduction.

Aim of this chapter is to present MEMS technology and its historical development (subchapter 1.1.and 1.2) together with MEMS principle applications in automotive field and optical field (subchapter 1.3).

1.1. MEMS historical background

The field of microelectronics began in 1948 when the first transistor was invented. This first transistor became obsolete in 1950s when the bipolar junction transistor (BJT) was developed. Then in 1952 Shockley proposed the first modern junction field-effect transistor (JFET) and these two types of electronic devices became the heart of all microelectronic components, but it was the development of integrated circuits (ICs) in 1958 that spawned today's computer industry.

IC technology has developed rapidly during the last 50 years and the number of transistor contained within a single IC has increased following what is commonly referred as "Moore's law" (Fig. 1).

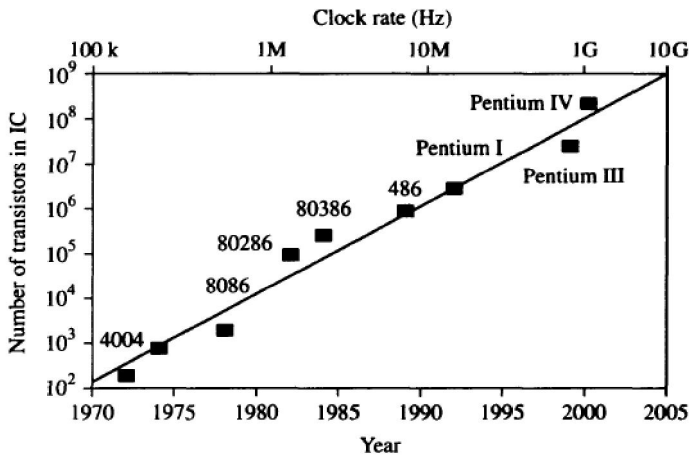


Fig. 1 Moore's law for integrated circuit: exponential growth in number of transistors in an IC from 1970 to 2005

Since 1970, the complexity of ICs has doubled every two to three years. The dimension of manufactured devices and ICs has decreased from 20 microns to the sub micron level of today. Current ultra large scale integration (ULSI) technology enables the fabrication of more than 10 millions transistors and capacitors on a typical chip.

IC fabrication is dependent upon sensors to provide input from the surrounding environment, just as a control system needs actuators (also referred as transducers) in order to carry out the desired outputs. Due to the availability of silicon as material (it can be produced from SiO_2), a large effort was spent into developing Silicon process and technologies to produce silicon sensors and actuators.

Attention in this area was focused on microsensors development. The first microsensor, which has been the most successful, was the silicon pressure sensor. In 1954 the piezoresistive effect in silicon and germanium was discovered [1], and many consider this discovery as the birth of MEMS. In the first decades MEMS products were limited to pressure and acceleration sensors, but in a short time they

started affecting the nation's economy and wealth. In the 1980s and 1990s, many governments heavily funded the development of MEMS technology, particularly the United States, Japan and Germany.

A so high level of interest in MEMS technology comes from both business and technical directions. In fact they are attractive to business because multiple emerging markets for MEMS promise large financial gain and they are also attractive from a technological point of view. More in detail MEMS technical attractiveness include multiple factors:

- cost of single device scales with its size as a result of batch manufacturing technology (batch fabrication involves the simultaneously manufacturing of hundreds or thousands of identical parts thus diluting the impact of fixed costs, including the costs of maintaining expensive cleanrooms and assembly facilities);
- MEMS devices are characterized by excellent mechanical properties due to their pure crystalline structure (eliminating mechanical fatigue and hysteresis makes silicon almost a perfect material for sensors, its mechanical properties are comparable to steel);
- MEMS can be fabricated by using the same technology infrastructure already created for IC industry. This involves to have processing equipment, sophisticated diagnostic and test equipment, design and simulation tools, high volume IC packaging technologies immediately available for MEMS production;
- there is potential for the MEMS integration with IC circuitry to create low cost integrated mechanical, optical and biological systems on a chip;
- there is an available pool of educated silicon processing technologists;
- MEMS can be used as a packaging vehicle for nano devices, thus suggesting synergy with nanotechnology which receives a high level of worldwide government funding.

Even though MEMS technology has been very promising, commercialization efforts have encountered multiple stumbling blocks that have significantly delayed the availability of commercial devices. A first stumbling block was the fact that the IC industry has not provided all process modules required to fabricate mechanical devices (such as wafer deep etching, double side wafer alignment and multiple wafer bonding) and the development of such MEMS processes was long and expansive. Secondly, the mechanical properties of IC materials were unknown and dependent on the fabrication process as well as electrical stability of silicon structures. The third point is that in the IC industry the structure thickness was not an issue, IC industry required an accuracy on thickness of about $\pm 10\%$, but in MEMS industry the thickness becomes a key point and a better control for mechanical thickness is required. Moreover high volume, low cost MEMS dedicated testing had to be developed entirely by the MEMS industry. And finally the compatibility with the real world was the major task to be developed by MEMS industry. All these factors have slow down the development of the first MEMS products and the volume implementation of the first devices was very slow, as shown in Tab. 1.

Product	First Prototype	Cum Volume 1M	Incubation
Pressure sensor	1961	1984	23 years
Acceleration sensor	1970 piezoresistive	1995	25 years
	1977 capacitive	1995	18 years
Ink jet printers	1977	1996	19 years
Displays	1979	2001	22 years

Tab. 1 Volume implementation of the first devices

The incubation periods shown in Tab. 1 may seem long, but they are similar to the incubation of other emerging technologies such as cell phones or satellite TV.

In the 1990s, MEMS programs had been established at all major university all around the world and several hundred MEMS fabrication facilities have been founded since 2005 in academic and commercial environments.

In 2007, 2 billion MEMS units have been produced and 2.5 billion have been produced in 2008. But by 2012, it is 6.7 billion of MEMS devices which will be shipped worldwide. An interesting fact is that, despite the large 2007/2008 increase in units for MEMS (25%), the market value growth is “only” 9%. This effect is justified by a strong price pressure MEMS devices are currently subject to. After 2009, RF MEMS and Si microphones will both contribute to the largest number of MEMS devices (over 45%).

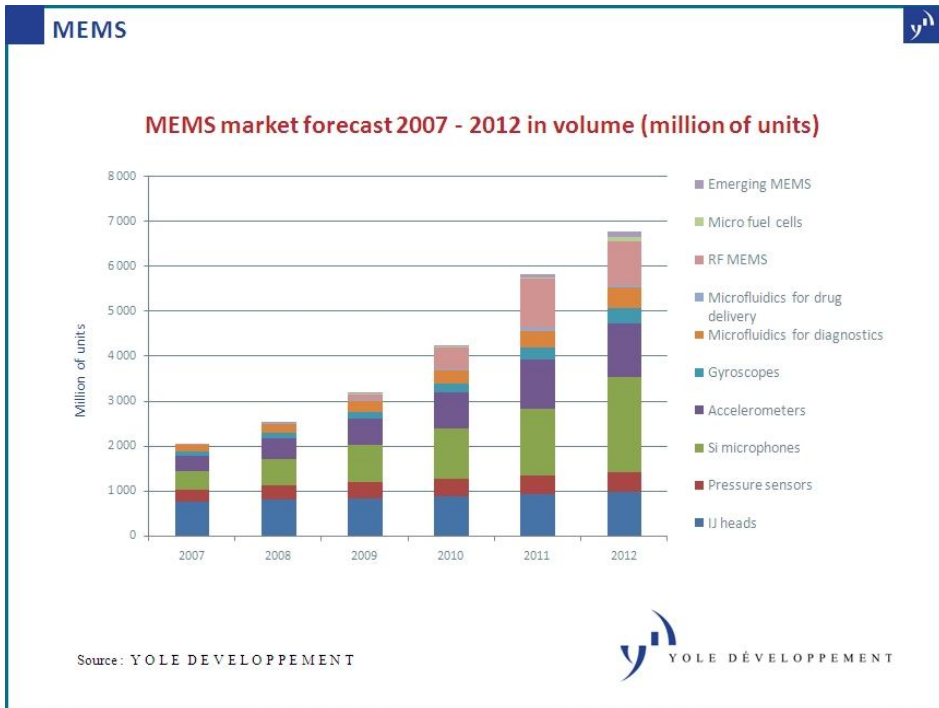


Fig. 2 Global MEMS market (Yole MEMS market forecast [2])

1.2. MEMS fabrication and technologies

MEMS devices and systems involve some form of lithography-based microfabrication borrowed from the microelectronic industry and enhanced with specialized techniques generally called “micromachining”. As mentioned in the previous section, the batch fabrication, that is characteristic of microelectronics industry, offers a potential for great cost reduction when manufacturing in high volume. Micromachining is a batch process in which dozen to tens thousands of identical elements are fabricated simultaneously on the same wafer.

Lithographic techniques generally require the use of flat substrates. Silicon is often used even when there are no electronic components in the device because the tools and the instruments needed for microfabrication are designed to match the characteristics of silicon wafers.

Silicon micromachining combines adding layers of material over a silicon wafer with etching (selectively removing material) precise patterns in these layers or in the underlying substrate. The implementation is based on a broad portfolio of fabrication processes including material deposition, patterning and etching techniques (see Fig. 3). Lithography plays a key role in the definition of accurate and precise patterns and it offers in-plane sub-micron precision on dimensional scales from micron to millimetre. Thin film deposition and etching techniques in combination with wafer-bonding techniques allow patterning of the third dimension, making possible the creation of movable parts. The combination of lithography with thin-film methods tends to result in structure characterized by extrusion of two-dimensional features into the third dimension.

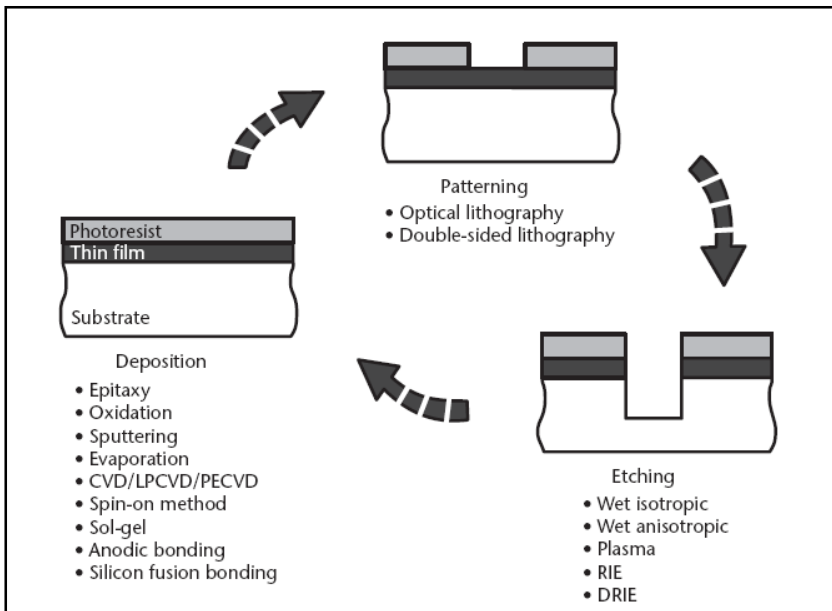


Fig. 3 Basic process flow in micromachining: layers are deposited; photoresist is lithographically patterned and then used as a mask to etch the underlying materials. The process is repeated until the completion of the microstructure.

From previous description is clear that microfabrication is based on planar technologies: constructing the electronic devices and MEMS components on substrates that are in the form of initially flat wafer. Starting from the silicon substrate, MEMS are fabricated using the same standard process steps used in integrated circuit manufacturing including photolithography, wet and dry etching, oxidation, diffusion, low-pressure chemical vapour deposition (LPCVD) and sputter deposition.

Common practice is to classify MEMS process flows into two primary types: *bulk micromachining* and *surface micromachining*. Bulk micromachining encompasses flows that etch deeply into the substrate, while surface micromachining collects flows that create microstructure with the removal of sacrificial layers from beneath thin-film structures, leaving free standing mechanical structures.

Requirements of a MEMS process flow are inclusion of one or more mechanical materials, steps process to shape these materials and, in most cases, steps process to release parts of the structural material from other anchored materials. The choice of micromachining process depends on the specifications on device dimensions and tolerances. Usually over 10 μ m thickness structures require bulk micromachining, while structures under 10 μ m incorporate surface micromachining or hybrid bulk/surface micromachining.

They are five main categories of micromechanical materials: substrate materials, surface materials, spacers, structural materials and finally active materials. The structural materials and substrate materials, which must be the same, must be able to survive to the various process steps. Spacer materials are usually completely etched or partially etched away to release microstructures and because of this function they are also called sacrificial materials. Surface materials may be used to protect the substrate or structural materials for certain etching steps, and they are also important to achieve electrical isolation. Finally active materials are incorporated on structures to exploit their special physical transduction characteristics. Probably every possible transduction mechanism has been explored in MEMS. Common transduction effects are silicon piezoresistance to measure stress, the piezoelectric effect in ZnO for both stress sensing and actuation, temperature coefficient of resistance and thermoelectric properties of silicon, aluminium and other conductors to measure temperature and various magnetic materials to couple mechanically to magnetic fields.

It is not possible to identify a single process flow which can be used to fabricate all possible MEMS devices, however some canonical process flows cover the basic MEMS fabrication concepts and form a basis for many other derivatives. These canonical process flows are: silicon etching and bonding, surface micromachining and bulk micromachining.

1.2.1. Silicon etching and bonding

Silicon is one of the few materials that are economically manufactured in single crystalline substrates. This crystalline nature provides significant electrical and mechanical advantages. In fact the precise modulation of silicon electrical conductivity using impurity doping is the very core of the operation of semiconductor devices, while from a mechanical point of view it is extremely robust and stable with mechanical characteristics similar to steel.

Silicon as an element exists with three different microstructures: *crystalline*, *polycrystalline*, or *amorphous*. Polycrystalline, or simply "polysilicon," and

amorphous silicon are usually deposited as thin films with typical thicknesses below 5 μm . Crystalline silicon substrates are commercially available as circular wafers characterized by 100-mm and 150-mm diameters, larger diameter used by the integrated circuit industry are currently economically unjustified for MEMS.

Silicon has a diamond-cubic crystal structure and its crystallographic planes play an important role in the design and fabrication of silicon based MEMS and deeply affect some material properties.

Silicon etching is one of fundamental process for MEMS fabrication. In etching the objective is to selectively remove material using imaged photoresist as a masking template. The pattern can be etched directly into the silicon substrate or into a thin film, which may be in turn used as a mask for subsequent etches. For a successful etch there must be sufficient selectivity between the material being etched and the masking material. Etch processes for MEMS fabrication deviate from traditional etch processes for the integrated circuit industry and remain to a large extent an art.

Several etching techniques exist, the most important for MEMS fabrication are:

- wet isotropic and anisotropic etching;
- electrochemical etching;
- plasma etching;
- reactive ion etching (RIE) and deep reactive ion etching (DRIE).

Wet chemical etching is widely used in semiconductor processing and it is the oldest form of etching. It consists in the immersion of a patterned substrate in a suitable chemical liquid that attacks the exposed regions of the substrate and leaves the protected regions alone. The rate of etching and the shape of the resulted etched region depend on many factors such as the type of substrate, the specific chemistry of the etchant, the choice of the masking layer, the temperature and whether or not the solution is well stirred. Wet etching can etch very deeply in the substrate and this is the motivation because it is common to refer to these processes as bulk micromachining. Most of the wet etching processes are *isotropic*, that means that are unaffected by crystallographic orientation and consequently the rate of the material removal does not depend on substrate orientation (the most common isotropic wet etchant is HNA which is a mixture of hydrofluoric, nitric and acetic acids).

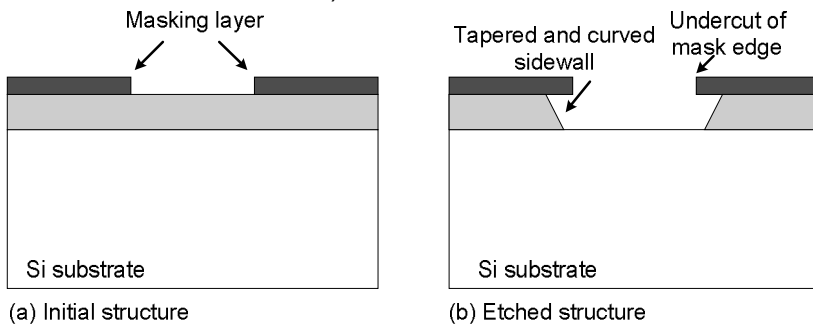


Fig. 4 Pattern transfer by isotropic wet etching through the openings in a mask layer. Because the wet etch is isotropic, the mask is undercut and the sidewall is typically tapered and curved

However some wet etchants exhibit orientation-dependent etch rate and they perform an *anisotropic wet etching*. Specifically strong bases such as potassium hydroxide (KOH), tetramethyl ammonium hydroxide (TMAH) and ethylene diamine pyrocatechol (EDP) exhibit preferential etching along the $\langle 100 \rangle$ and $\langle 110 \rangle$ crystallographic directions and orders of magnitude smaller etch rate in the $\langle 111 \rangle$ direction. Consequently a long etch of a silicon wafer with orientation $\langle 100 \rangle$ will determine $\langle 111 \rangle$ planes everywhere, as shown in Fig. 5.

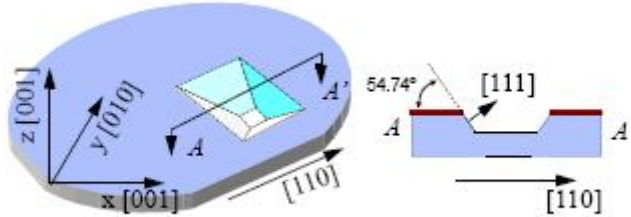


Fig. 5 Anisotropically wet etched pit in $\langle 100 \rangle$ silicon wafer

For these kind of etchants a silicon oxide or silicon nitride mask must be used in general.

The relative large etch rates of anisotropic wet etchants ($>0.5 \mu\text{m}/\text{min}$) make it difficult to achieve uniform and controlled etch depths. Some applications, such as bulk-micromachined pressure sensors, demand a thin silicon membrane (5 to $20\mu\text{m}$) with dimensional thickness control and uniformity better than $0.2\mu\text{m}$, which is very hard to achieve using timed etching. Instead the thickness control is reached using a precisely grown epitaxial layer and controlling the etch reaction with an externally applied electric potential. This method is commonly referred as *electrochemical etching*.

Another etching technique widely used in MEMS fabrication is the *plasma etching* technique. Plasma etching involves the generation of chemically reactive neutrals and ions that are accelerated under the effect of an electric field toward a target substrate. The reactive species are formed by collision of molecules in a reactant gas (e.g., SF_6 , CF_4 , Cl_2 , NF_3) with a cloud of energetic electrons excited by a RF electric field. When the etch process is purely chemical, powered by the spontaneous reaction of neutrals with silicon, it is colloquially referred to as plasma etching. But if ion bombardment of the silicon surface plays a synergistic role in the chemical etch reaction, the process is then referred to as *reactive ion etching (RIE)*. In RIE, ion (e.g., SF_x^+) motion toward the substrate is nearly vertical, which gives RIE vertical anisotropy. Moreover starting from 1990s the *deep reactive ion etching (DRIE)* technique has been developed in order to have an etch process capable of obtaining vertically etching high-aspect-ratio trenches.

As well as etching, *bonding* is another fundamental process used in MEMS fabrication and packaging. Wafer bonding is a method for firmly joining two wafers to create a stacked wafer layer. There are three types of wafer bonding techniques:

- direct bonding;
- field assisted bonding;
- bonding with an intermediated layer.

In *direct bonding* the first step is the cleaning of the surfaces to be bonded, then the surfaces are contacted and pressed together, using hydrogen bonding to

provide a modest degree of adhesion. Finally the contacted pair is placed in a high temperature furnace to fuse the two wafers together. The resulting bond is as strong as silicon itself. An alternative method, which is restricted to certain glasses bonded to conductors is called *field assisted bonding* or *anodic bonding*. The mechanism responsible for anodic bonding is the mobility of sodium ions in the glass. When the silicon wafer is placed on the glass, and the two are heated to temperature in order of 500°C, a positive voltage applied to the silicon repels sodium ions from the glass surface creating a negative charge at the glass surface. The attraction force between positively charged silicon wafer and the negatively charged glass surface brings the two surfaces intimate contact. Finally another common bonding technique adopted in MEMS fabrication is the *bonding with an intermediate layer*. This technique is similar to the common use of adhesive to bond structural elements together. In the case of microelectronics the adhesive elements must meet the thermal and cleanliness requirements of microfabrication and they are in general special glasses, or gold layer or polymeric adhesive.

An example of MEMS processes that combines together two techniques described above is the dissolved wafer process. The dissolved wafer process combines wet silicon etching and wafer bonding to form boron doped microstructures on a glass substrate. An example of dissolved wafer process flow is shown in Fig. 6 for an inertial latch. This inertial latch closes a gold contact when exposed to threshold acceleration [3]. The “handle” silicon wafer is a sacrificial mold for defining the height of the microstructures. Thin silicon oxide layer is deposited to make electrically isolating springs as shown in Fig. 6. The front side of silicon wafer with the patterned structural layers is anodically bonded to a glass substrate with gold interconnect. The glass substrate has excellent bond strength to silicon. For capacitive sensor applications, the use of a glass eliminates capacitive parasitic that would be present if a conductive silicon substrate were used instead. The structures are released by etching the entire handle wafer with a wet silicon attack.

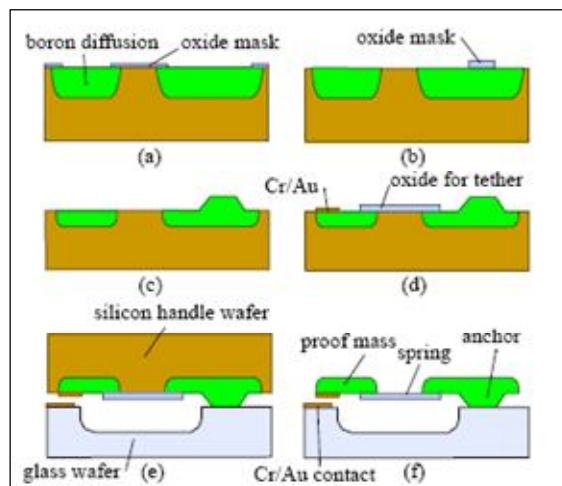


Fig. 6 A dissolved wafer process. (a) Masked boron diffusion. (b) Silicon oxide deposition and patterning for silicon etch. (c) Silicon etch and mask strip. (d) Silicon oxide deposition and patterning; Chromium and gold deposition and patterning. (e) Anodic bonding. (f) Dissolve handle wafer for release.

1.2.2. Surface micromachining

Since the beginning of the 1980s much interest has been directed toward micromechanical structures fabricated by a technique called *surface micromachining* which is based on deposition and subsequent attach of sacrificial layers on the silicon substrate, in order to create the MEMS components (the sacrificial material is employed during the fabrication process to realise the microstructure but does not constitute any part of the final miniature device).

The main advantages of this technique are that the surface micromachined structures can be an order of magnitude smaller than the bulk micromachined ones, and can be easily integrated with integrated circuit components.

There are several approaches for surface micromachining: the first approach is the sacrificial layer technology for the realisation of microstructures, the second approach incorporates IC technology and wet anisotropic etching and finally the third approach uses plasma etching to fabricate microstructures at the silicon wafer surface.

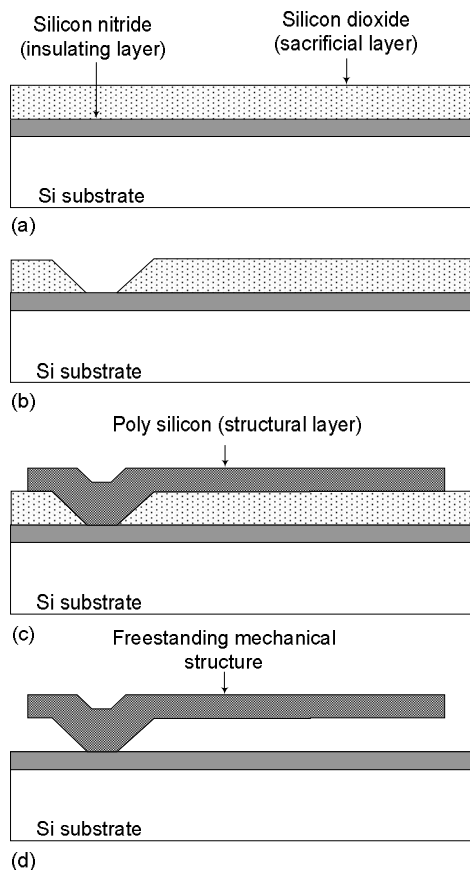


Fig. 7 Process flow for a freestanding cantilever beam

The most widely used is the sacrificial layer approach. This technology uses in most situations polycrystalline silicon instead of single-crystal silicon as the structural material, in fact low pressure chemical vapour deposition (LPCVD) of polysilicon (poly-Si) is well known in standard IC technologies and polysilicon has excellent mechanical properties that are similar to single-crystalline silicon. When polycrystalline silicon is used as structural layer, silicon dioxide (SiO_2) is usually employed as the sacrificial material.

The principal process steps in sacrificial technology are:

- Deposition and patterning of a sacrificial SiO_2 layer on the substrate.
- Deposition and definition of a poly-Si film.
- Removal of the sacrificial oxide by lateral etching in hydrofluoric acid (HF), which means etching away the oxide underneath the poly-Si structure.

A typical example of surface micromachining application is the creation of a freestanding beam anchored to a silicon substrate via an insulating nitride layer (Fig. 7). A layer of silicon nitride is first deposited by LPCVD on a silicon wafer. The nitride film will be the base on which the beam will lie and it acts as a protective layer for the substrate. A layer of sacrificial SiO_2 is deposited by chemical vapour deposition (CVD) on the top of nitride layer (Fig. 7(a)) and patterned as shown in Fig. 7 (b). The thickness of the patterned oxide is equal to the distance between the final freestanding beam and the silicon nitride layer. At this point polysilicon is deposited by LPCVD on the patterned oxide as shown in Fig. 7(c) and finally the sacrificial SiO_2 is laterally etched and the freestanding beam is created.

1.2.3. Bulk micromachining

Bulk micromachining is the most used of the two principal silicon micromachining technologies. It emerged in the early 1960s and has been used since then in the fabrication of many different structures. Bulk micromachining is used in the manufacture of the majority of commercial devices (almost all pressure sensors and silicon valves and 90% of silicon acceleration sensors).

The term *bulk micromachining* suggests the fact that this micromachining technique realizes microstructure within the bulk of a single-crystal silicon (SCS) wafer by selecting removal the wafer material.

The microstructures fabricated by using bulk micromachining may cover the thickness range from submicrons to the thickness of the full wafer (200 to 500 μm) and the lateral size ranges from microns to the full diameter of a wafer (75 to 200 mm).

Etching is the key technological step for bulk micromachining, and the etching techniques used several of the aforementioned techniques:

- wet isotropic and anisotropic etching;
- plasma isotropic etching;
- reactive ion etching ;
- etch-stop technique.

Some of these etch processes have already been used as a standard technology in the microelectronics industry (e.g. reactive ion etching). In addition to etch process, bulk micromachining often utilises wafer bonding technology and buried oxide-layer technology.

Bulk micromachining is typically used to obtain membranes used in pressure sensors. The process steps used to realize a typical membrane is shown in Fig. 8.

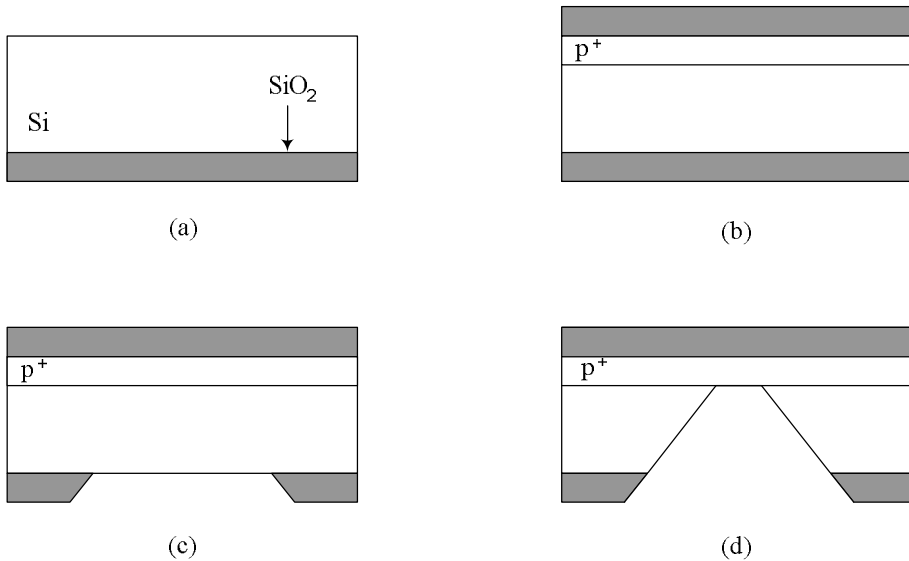


Fig. 8 Process steps for the realization of a silicon membrane

The starting structure is a silicon single-crystal silicon substrate with a silicon oxide layer on the inferior surface (Fig. 8 (a)). Then a Boron diffusion is realized to create an etch stop p⁺ doped region, and a silicon oxide layer is grown on the upper wafer surface in order to protect the wafer surface during the etching phase (Fig. 8(b)). The third step is the creation of the mask used to obtain the desired geometry and finally the last step is the creation of the membrane by etching the silicon from the backside opening. This etch is typically performed by using KOH etchant and the attack will stop in correspondence of the p⁺ region.

With the structure described above piezoresistive pressure sensor can be realized by simply building polysilicon resistors on the top of the membrane [4]. Any deflection due to pressure differences between the two membrane sides will induce either compressive or tensile stress on the resistors changing slightly their resistances.

1.3. MEMS leading applications

Microelectromechanical systems represent the outstanding state of art for a broad range of applications such as biomedical applications, communication applications, automotive, and optical applications.

Indeed micromachining and MEMS technologies can be used to produce complex electrical, mechanical, fluidic, thermal, optical and magnetic structures, devices and systems on a scale ranging from organs to subcellular organelles. This miniaturization ability has enabled MEMS to be applied in many areas of biology, medicine and biomedical engineering, a field generally referred as BioMEMS. BioMEMS research fields and applications are the most disparate: realization of microsensor arrays that act as electronic nose or tongue, microfabrication of neural systems capable of controlling motor or sensory prosthetic devices, painless microsurgical tools, complete microfluidic systems for total chemical or genetic analysis and drug delivery systems are only some examples.

In order to report some examples of BioMEMS applications we can mention the commercially successful low-cost disposable medical pressure sensor developed by Lucas NovaSensor NPC-107 [5]. The development of surgical microgrippers actuated by shape-memory-alloy forces which are capable of grasping tissues during endoscope surgical procedures [6]. And finally scalpel driven by a piezoelectric microactuator which is an innovative example of using MEMS technology in surgical tools [7]. The aforementioned devices are only few examples of BioMEMS systems, but are sufficient to show the variety and the incisiveness of MEMS applications in medical field.

Another field in which MEMS have shown to be a winning choice is RF applications. Indeed MEMS applications in RF and microwave electronics are revolutionizing wireless communications and promise to provide innovative applications. The term "RF MEMS" encompasses several distinct types of devices, including RF switches and relays, resonators, varactors (variable capacitors) and inductors. Applications of RF MEMS include all types of wireless communications, radar, satellites, military radio, instrumentation and test equipment. Compared to conventional RF components, RF MEMS offer significant benefits, including lower power consumption, lower insertion loss, smaller form factor and enhanced re-configurability which can result in superior functionality and performance.

RF MEMS have come to market more recently than other types of MEMS, but the RF MEMS market is now growing rapidly. RF MEMS switches can be classified by actuation method (electrostatic, magnetic, piezoelectric, thermal), by contact mechanism (capacitive, metal-to-metal), or by anchor mechanism (cantilever, fixed-fixed beam) [8]. And they are typically composed by a thin metal cantilever, a bridge, a diaphragm (or some similar structure) to open an RF transmission line or shunt it to ground. MEMS switches feature excellent RF characteristics, thus outperforming many traditional RF circuits.

Even if MEMS devices find employ in a wide range of applications, such we have seen before, the two leading MEMS applications are without any doubt automotive applications and optical applications. Then it's important to have a more detailed description of these application fields, as will be shown in next two paragraphs.

1.3.1. MEMS for automotive applications

The automotive market has been a key driving market for the development of microelectromechanical systems.

Automotive MEMS applications began with the manifold absolute pressure sensor (MAP), developed by many companies in the mid-80s. The MAP sensor was used together with a manifold air temperature sensor (MAT) to compute the density of air entering the engine. The product of air density and engine speed gave the mass of air entering the engine, this information was used to control the engine air-to-fuel ratio thus efficiently minimizing the tailpipe emissions, and bringing them into compliance with federal regulations.

Only the non-invasive blood pressure sensor and the ink jet print head rivalled this application as the initial high-volume micro-electromechanical device. The first MAP sensor was a uncompensated bulk micromachined piezoresistive pressure sensors, then continuous progress in technology allowed improving the sensor structure and the conditioning read out electronic until having a CMOS-integrated, bulk micromachined pressure sensor with non-volatile memory allowing the incorporation of state-of-the art digital signal processing to add features like three-wire interface, changeable rail voltages, and improved accuracy [9]. Today, the volumes of MAP sensors continue to grow and are measured in millions of units per year, matching the total volume of cars and trucks produced by the automotive industry each year. Further, newer versions of these MAP sensor devices have been designed, which take advantage of the advances in the MEMS processing technology.

A similar scenario was played out in the mid-1990's, when air-bag restraint systems were introduced. Non-MEMS, ball-in-tube acceleration sensors were used for relatively high-cost, inflatable restraint systems when these were vehicle options. When mandated, the need for a lower cost motion sensor became apparent. Micromachined accelerometers were able to fill this need, and are replacing most original sensing technologies in the automobile. Then in the 1990s the airbag-deployment accelerometer started high volume production and several companies developed capacitive accelerometer fabricated with surface micromachining technique (Fig. 9).

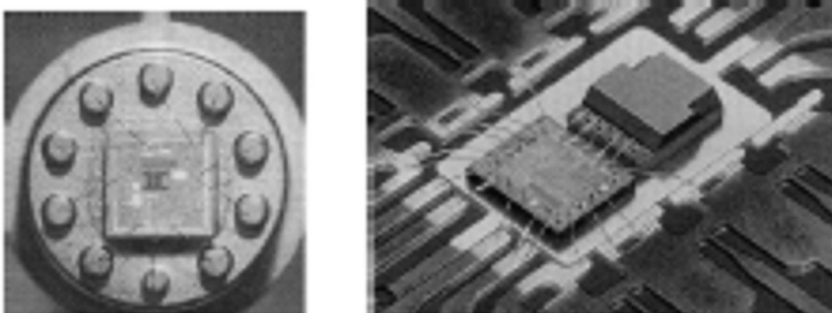


Fig. 9 The initial Analog Devices (left) and Motorola (right) accelerometers for airbag deployment.

Automotive applications have some stiff requirements, indeed they have to guarantee high quality and exceptional reliability in addition to low costs.

Even with the challenging requirements of the automotive market, its high volumes (15 million cars/year in the US alone), have provided incentive for continued development of MEMS automotive applications. Today's high-end vehicles feature up to 100 different sensors among which about 30 these are now MEMS, and the percentage is forecasted to grow. The market is composed by accelerometers, gyroscopes, pressure and flow sensors. Latest applications comprise IR sensors for air quality and micro-mirrors for displays. The automotive segment is accounted for \$1.6 billion, making this the second biggest opportunity after IT peripherals and inkjet print heads. By 2011 the market will top \$2.2 billion, with a compound annual growth rate (CAGR) of roughly 7%.

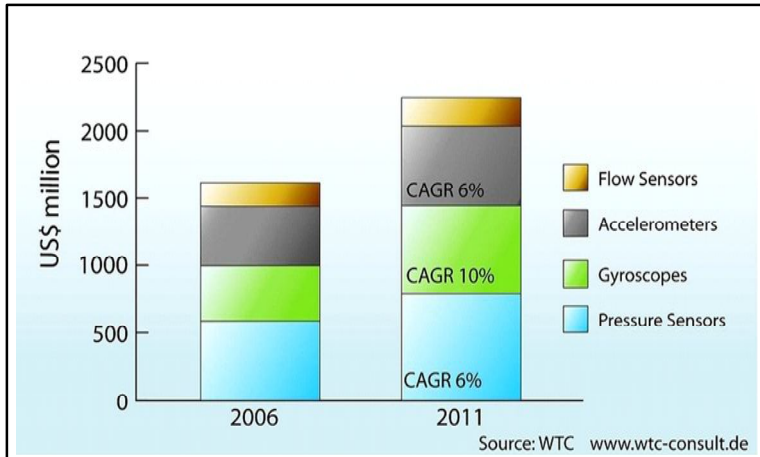


Fig. 10 Market for Automotive MEMS sensor (source wtc-consult).

The intelligent vehicle is provided by sensors and systems for collision avoidance, accident prevention and severity reduction. The main automotive sensor applications can be classified in: active safety, passive safety, navigation and drive assistance.

Active safety

Active safety represents the most important requirement in modern vehicles. The MEMS accelerometers and gyroscopes are both sensors which can perfectly fit active safety requirements in the automotive domain.

Some examples of active systems which employ MEMS technology are the well known ABS (Anti-lock Braking System) which prevents the wheels from locking while braking, Cornering Brake Control (CBC) which performs stabilisation during partial braking whilst cornering and Traction control system (TCS) which is designed to prevent loss of traction. Furthermore sensor systems are employed in the correction of drive trajectory: Electronic (Dynamic) Stability Control (ESC, ESP) compares the driver's intended direction, to the vehicle's response, via lateral acceleration, rotation (yaw) and individual wheel speeds. ESC then brakes individual front or rear wheels and/or reduces engine power as needed to get correct under steer or over steer.

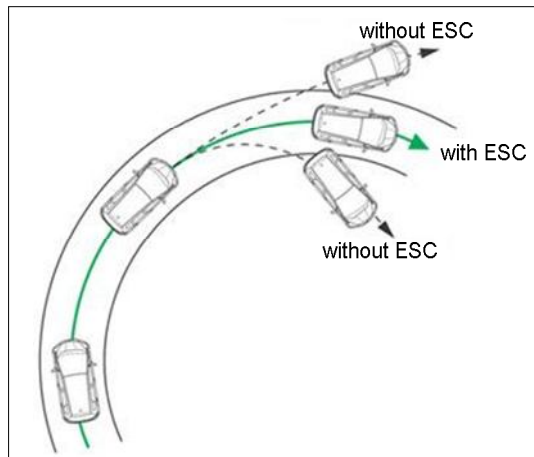


Fig. 11 Effect of ESC

Passive safety

The main examples of passive safety system are the intelligent airbags. They care to soften impact for passengers during car crashes. Since the airbag system must act at the right instance and also with the proper force toward the car occupants, the identification of type of collision, collision direction, g-force impact assumes critical importance. The adoption of MEMS accelerometer, thanks to their high integration capability and accuracy, can lead to detection system of new generation replacing standard electromechanical system, achieving enhanced passenger care. Since the instant of the impact cannot be predicted in advance, it is extremely important to detect for each passenger the seat position and if at the moment in which the crash happens the occupant is lifted from the seat. The MEMS accelerometer can determine the correct positioning of car occupants to dose the force of airbags bang.

Inertial navigation system

The satellite navigation system in vehicles allows determining the position of the car anywhere on the world by radio signals from Global Positioning System (GPS) satellites. Nevertheless, data from satellite is not sufficient to constantly determine the correct positioning since the satellite signal could not be always available due to shadowing by buildings and overpasses especially in crowded urban areas. In this scenario, a dead reckoning GPS system can replace the navigation system continuing tracking movements during the time when satellite signals are not available. MEMS-based gyroscope and a magnetometer can path the motion direction and together with an accelerometer which gives information about velocity of the moving object can implement complementary tracking system to GPS. These systems are called *inertial navigation systems* (INS) and they can detect a change in the geographic position (a move east or north for example), in the velocity (speed and direction of the movement) and in the orientation (rotation about an axis) of a moving object.

The working principle of an INS is described in the following. MEMS gyroscopes measure the angular velocity of the system in the inertial reference frame. By using the original orientation of the system in the inertial reference frame as the initial condition and integrating the angular velocity, the system's current orientation is

known at all times. Accelerometers measure the linear acceleration of the system in the inertial reference frame, but in directions that can only be measured relative to the moving system (since the accelerometers are fixed to the system and rotate with the system, but are not aware of their own orientation). However, by tracking both the current angular velocity of the system and the current linear acceleration of the system measured relative to the moving system, it is possible to determine the linear acceleration of the system in the inertial reference frame. Performing integration on the inertial accelerations (using the original velocity as the initial conditions) using the correct kinematic equations yields the inertial velocities of the system, and integration again (using the original position as the initial condition) yields the inertial position.

Driver assistance

Driver assistance systems are systems studied to help the driver in the driving process. Some example of drive assistance systems are Adaptive Cruise Control (ACC), Intelligent Speed Adaptation (ISA), Intelligent Light Positioning, or Automatic Parking.

Adaptive or Autonomous Cruise Control (ACC) is an optional cruise control system appearing on some more upscale vehicles. The system goes under many different trade names according to the manufacturer. These systems use either a radar or laser setup allowing the vehicle to slow when approaching another vehicle and accelerate again to the preset speed when traffic allows. ACC technology is widely regarded as a key component of any future generations of intelligent cars.

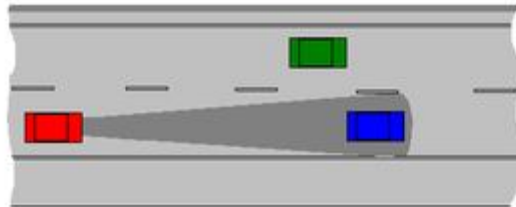


Fig. 12 Schematic of automatic cruise control (the read car automatically follow the blue car)

Intelligent Speed Adaptation (ISA), also known as Intelligent Speed Assistance, is any system that constantly monitors vehicle speed and the local speed limit on a road and implements an action when the vehicle is detected to be exceeding the speed limit. This can be done through an advisory system, where the driver is warned, or through an intervention system where the driving systems of the vehicle are controlled automatically to reduce the vehicle's speed.

Intelligent speed adaptation uses information about the road on which the vehicle travels to make decisions about what the correct speed should be. This information can be obtained through use of a digital maps incorporating roadway coordinates as well as data on the speed zoning for that roadway at that location, through general speed zoning information for a defined geographical area (e.g., an urban area which has a single defined speed limit), or through feature recognition technology that detects and interprets speed limit signage. ISA systems are designed to detect and alert a driver when a vehicle has entered a new speed zone, when variable speed zones are in force (e.g., variable speed limits in school

zones that apply at certain times of the day and only on certain days), and when temporary speed zones are imposed (such as speed limit changes in adverse weather or during traffic congestion, at accident scenes, or near roadworks). Many ISA systems will also provide information about locations where hazards may occur (e.g., in high pedestrian movement areas, railway level crossings or railroad grade crossings, schools, hospitals, etc.) or where enforcement actions is indicated (e.g., speed camera and red light camera locations).

The purpose of ISA is to assist the driver in keeping to the lawful speed limit at all times, particularly as they pass through different speed 'zones'. This is particularly useful when drivers are in unfamiliar areas or when they pass through areas where variable speed limits are used. There are several types of technology currently available for determining local speed limits on a road and determining the speed of the vehicle, in particular we focus on the one which uses MEMS sensors: dead reckoning technology.

Dead reckoning (DR) uses a mechanical system linked to the vehicle's driving assembly in order to predict the path taken by the vehicle. By measuring the rotation of the road wheels over time, a fairly precise estimation of the vehicle's speed and distance travelled can be made. Dead reckoning requires the vehicle to begin at a known, fixed point. Then, by combining speed and distance data with factors such as the angle of the steering wheel and feedback from specialized sensors (e.g., accelerometers, flux gate compass, gyroscope) it can plot the path taken by the vehicle. By overlaying this path onto a digital map, the DR system knows approximately where the vehicle is, what the local speed limit is, and the speed at which the vehicle is travelling. The system can then use information provided by the digital map to warn of upcoming hazards or points of interest and to provide warnings if the speed limit is exceeded.

Intelligent light positioning is gaining relevance in high end cars and is expanding down to more market segments. MEMS sensors like accelerometer and gyroscope can lead to a new generation of head lights enhancing road illumination and guaranteeing safer driving conditions. Thanks to motion detection, and assisted by GPS systems alignment of head light to various road conditions (e.g. asphalt, curves, uphill, downhill) and on vehicle condition (e.g. speed type pressure, suspensions, number of occupants).can be automatically performed.

Automatic parking is an autonomous car manoeuvring from a traffic lane into a parking place to perform parallel parking, perpendicular or angle parking. The automatic parking aims to enhance the comfort and safety of driving in constrained environments where much attention and experience is required to steer the car. The parking manoeuvre is achieved by means of coordinated control of the steering angle and speed which takes into account the actual situation in the environment to ensure collision-free motion within the available space.

The more recently system developed for automatic parking are Intelligent Parking Assist System (IPAS), also known as the Advanced Parking Guidance System (APGS) for Lexus models in the United States.

The IPAS/APGS uses computer processors which are tied to the vehicle's (sonar warning system) feature, backup camera, and two additional forward sensors on the front side fenders. The sonar park sensors, known as "Intuitive Parking Assist" or "Lexus Park Assist", includes multiple sensors on the forward and rear bumpers which detect obstacles, allowing the vehicle to sound warnings and calculate optimum steering angles during regular parking.[10] These sensors plus the two

additional parking sensors are tied to a central computer processor, which in turn is integrated with the backup camera system to provide the driver parking information.[11]. When the sonar park sensors feature is used, the processor(s) calculate steering angle data which are displayed on the navigation/camera touchscreen along with obstacle information. The Intelligent Parking Assist System expands on this capability and is accessible when the vehicle is shifted to reverse (which automatically activates the backup camera). When in reverse, the backup camera screen features parking buttons which can be used to activate automated parking procedures. When the Intelligent Parking Assist System is activated, the central processor calculates the optimum parallel or reverse park steering angles and then interfaces with the Electric Power Steering systems of the vehicle to guide the car into the parking spot.

1.3.2. MEMS for optical (MOEMS)

Micro –Opto-ElectroMechanical systems (MOEMS) are optical MEMS, this means that they are systems involving micromachining of structures in the micro to millimetre range whose purpose is to manipulate light.

Micro-Opto-ElectroMechanical systems represent a subset of the MEMS family that has been developed since the '90s for fibre optics telecommunication applications as consequence of the unprecedented growth of optical communications in the late 1990's due to the growth of the internet connections. This period of speculative growth was followed in 2001-2004 by one of the most significant market crashes in history, in which many start-up companies in who experienced unprecedented growth inaugurated with great fanfare at the end of 20th century were unceremoniously shut down at the start of the 21st century. Nevertheless the new MOEMS technology born in this period has not stopped its growth but has changed its perspective.

Historically, optical MEMS have been successfully used for TV and projection systems (this is the case of TI DLPs' technology). Following the telecom downturn, some companies have succeeded to explore several new applications that are wide spreading the use of optical MEMS. Despite the difficulties global market has encountered in the last part of the 2008 MOEMS market has increased from 2003 to 2008 with an outstanding Compound Annual Grow Rate (CAGR) of more than 30% passing from 780 million dollar in 2003 to more than 3 billion dollar in 2008.

Actually the most important fields were MOEMS are employed include: display (DMD), spectrometry, barcode scanners and picoprojectors.

Display (DMD)

Digital Micromirror Device (DMD) is a spatial light modulator developed at Texas Instruments that is the core of Digital Light Projection (DLP) projection technology, and was invented by Dr. Larry Hornbeck and Dr. William E. "Ed" Nelson in 1987.

A DMD chip has on its surface several hundred thousand microscopic mirrors arranged in a rectangular array which correspond to the pixels in the image to be displayed [12]. The mirrors can be individually rotated ± 10 - 12° , to an on or off state. In the on state, light from the projector bulb is reflected into the lens making the pixel appear bright on the screen. In the off state, the light is directed elsewhere (usually onto a heatsink), making the pixel appear dark.

To produce greyscales, the mirror is toggled on and off very quickly, and the ratio of on time to off time determines the shade produced (binary pulse-width

modulation). Contemporary DMD chips can produce up to 1024 shades of gray. The mirrors themselves are made up of aluminium and are around 16 micrometres across. Each one is mounted on a yoke which in turn is connected to two support posts by compliant torsion hinges. In this type of hinge, the axle is fixed at both ends and literally twists in the middle.

The two main applications of DLP systems are front projectors (small standalone projection units) and DLP rear projection television.

Projectors can be equipped with a single DMD chip or with three chips.

The first solution employs a spinning colour wheel between the light source and the DMD. The colour wheel is usually divided into multiple sectors: the primary colours (red, green, and blue) and the secondary colours usually employed to enhance the brightness. The DMD chip is synchronized with the rotating motion of the colour wheel so that the green component is displayed on the DMD when the green section of the colour wheel is in front of the lamp. The same is true for the red and blue sections. The red, green, and blue images are thus displayed sequentially at a sufficiently high rate that the observer sees a composite "full colour" image. In early models, this was one rotation per frame. Later models spin the wheel at two or three times the frame rate and some also repeat the colour pattern twice around the wheel, meaning the sequence may be repeated up to ten times per frame.

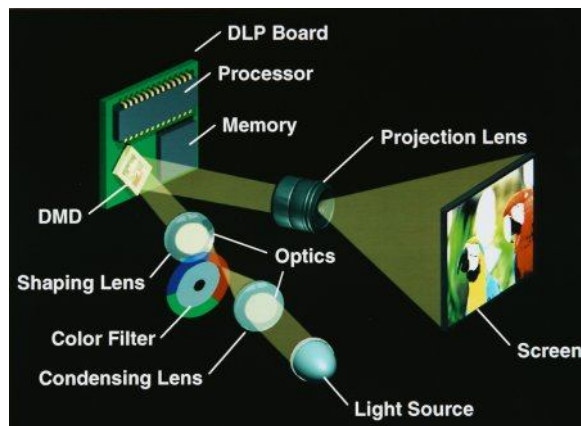


Fig. 13 One-DMD DLP Projector

A three-chip DLP projector uses a prism to split light from the lamp, and each primary colour of light is then routed to its own DMD chip, then recombined and routed out through the lens. Three-chip DLP projectors can resolve finer gradations of shade and colour than one-chip projectors, because each colour has a longer time available to be modulated within each video frame; furthermore, there won't be any flicker or rainbow effect like with the single chip solution. Like three-tube CRT (cathode ray tube) projectors, the optics for some three-chip DLP projectors must be carefully aligned.

The three-chip projectors are used in higher-end home theatre projectors, large venue projectors and DLP cinema projection systems. They can produce 35 trillion colours, which many suggest is more than the human eye can detect. The human eye is suggested to be able to detect around 16 million colours, which is theoretically possible with the single chip solution. However, this high colour precision does not mean that DLP projectors are capable of displaying the entire

gamut of colours we can distinguish (this is fundamentally impossible with any system composing colours by adding three constant base colours).

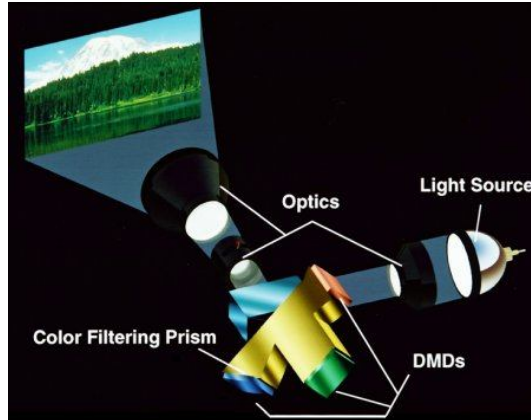


Fig. 14 Three-DMD DLP Projector

Spectromoter

A spectrometer is an optical instrument used to measure properties of light over a specific portion of the electromagnetic spectrum, typically used in spectroscopic analysis to identify materials [13]. The variable measured is most often the light's intensity but could also, for instance, be the polarization state. The independent variable is usually the wavelength of the light, normally expressed as some fraction of a meter, but sometimes expressed as some unit directly proportional to the photon energy, such as wave number or electron volts, which has a reciprocal relationship to wavelength. A spectrometer is used in spectroscopy for producing spectral lines and measuring their wavelengths and intensities. Spectrometer is a term that is applied to instruments that operate over a very wide range of wavelengths, from gamma rays and X-rays into the far infrared. If the region of interest is restricted to near the visible spectrum, the study is called spectrophotometry.

The use of a MOEMS in spectrometry leads to the miniaturization of device for spectrometry thus allowing the fabrication of microspectrometers such the example shown in Fig. 15.

By using the microspectrometer as key component, has been possible to develop an analytical apparatus for non-invasive, early detection of jaundice in new-born babies. After placing the hand-held device on the skin of the baby's forehead, the measuring operation starts. The instrument exposes a small area of the skin to white light and measures the specific intensity of the reflection. The concentration of bilirubin in the blood can thus be determined exactly and within a very short time. The measurement is independent of both skin colour and the exact age of the babies.

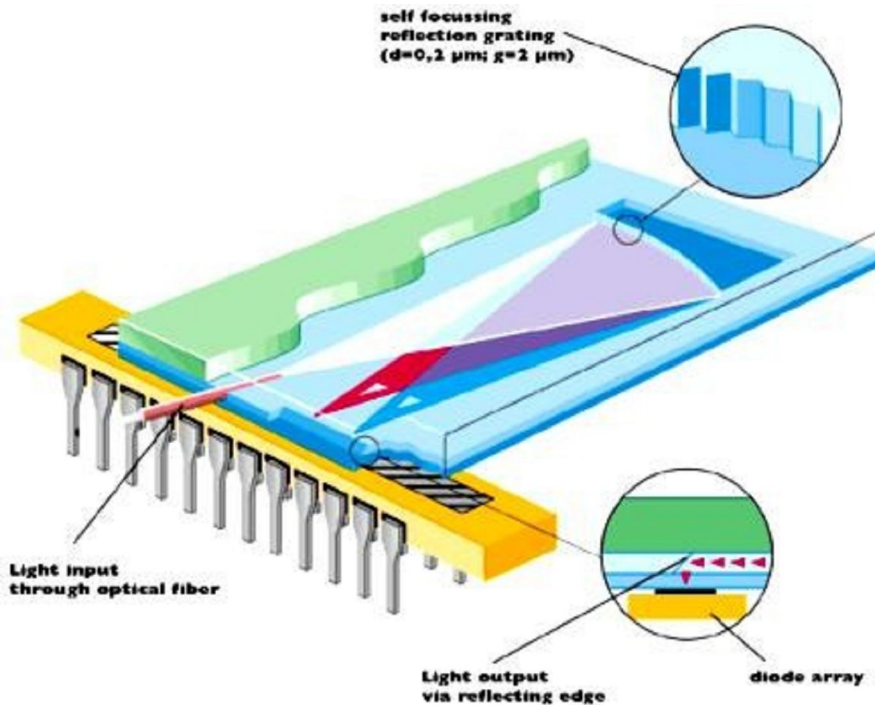


Fig. 15 Example of MOEMS spectrometer

Bar code scanners

The bar code scanners are available in various types; the basic principle of all the types is projecting light to the bar code and identifying the width of each bar based on the quantity of reflected light from the bar.

This bar code scanning can be done by either of the following two methods. The first method employs a fine beam spot which is scanned perpendicularly to code bars and reflected from each bar. Each bar is scanned one after the other by a single photodetector element. The second method is to project light evenly on the bar code surface and scanning the reflected lights from the code bars simultaneously by a photodetector or CCD (character coupled device) image sensor composed of a plural photodetector elements provided correspondingly to the code bars.

In both cases an optical system is needed to handle the scanning beam or the reflected light. Due to the size reduction and high integration of this system MOEMS are the best choice for this type of optical system. And in particular scanning micromirrors are attractive for this kind of applications due to their capability to reach large scan optical angles ($\pm 20^\circ$) and high operative frequency.

MEMS devices have proven their value and reliability in other markets and products, such as medical applications, consumer applications and automotive market. Thus we can assert that improved reliability is a key benefit of a MOEMS based bar code scanner compared to other bar code scanner technologies. Even after millions of scan, the integrity of the MEMS engine does not degrade due to the inherent properties of silicon. The oscillating silicon mirror is extremely small

and lightweight, reducing susceptibility to performance degradation resulting from bumps and vibrations often experienced with a handheld device.

Pico projectors and head-up displays

Today, the need for thinner TVs, portable electronics devices and more compact optical devices requires innovative optical technologies to shrink the light management module at the heart of many applications.

Mixing MOEMS technology with solid state lighting (LEDs, HBLEDs and/or laser diodes) is a new, unique solution to achieve a potential low cost and compact light engine. The successful development of a compact and low cost light engine will improve existing products and drive new markets such as pico projectors or head-up displays.

The aim of pico projectors is to realize low size, high performance portable projectors for notebook or palm PC and to realize integrated projector for handheld devices, like cell phones or digital cameras. This is a very promising market, which is destined to grow in the next years. In pico projectors MOEMS devices are used to deflect the light beam on a screen in accordance with the video signal read from a RAM memory. The MOEMS most suitable in being used as scanner are scanning micromirrors and in particular two dimensional scanning micromirrors which can deflect around two spatial directions [14].



Fig. 16 Example of pico projector integrated in a cell phone (source [15])

Head-up displays are the next generation of vehicle displays. The aim of head-up displays is to place visual information (provided from a GPS navigation system for example) where the driver can use it, they project the image directly on the vehicle windscreen thus creating a new level of driver delight and increasing safety in and around the vehicle.

However mixing solid state lighting and MOEMS require innovative solutions mixing optics, thermal management, electrical power conversion, electronic drive circuitry. Although there are many open technical issues to be solved regarding packaging, thermal management, cost/performance ratio, green laser lifetime and market access the first pico projectors suitable for use in a mobile phone has been demonstrated by US firm Microvision at the Global press Summit Conference in San Francisco in April 2008.



Fig. 17 Example of head-up display (source [15])

CHAPTER 2

MEMS DESIGN FLOW

It is widely accepted that in any complex engineering design process, a documented flow or procedure to go from a high-level design abstraction to a detailed manufacturing description suitable for fabrication is essential.

Flows offer several advantages over a more haphazard approach, first of all they inherently provide a structured and manageable design environment (this is essential in any complex design process in which hierarchy and partitioning can be used to reduce complexity and in which more than one individual works on the same project). Secondly, these structured design environments extend the usability of a technology to a large audience. Moreover design flows detail the input and output data for every step in the design process, as well as the flow of these data between the required tools.

The top-level goal of a design flow is to enable complex engineering design in as *short time as possible* and with *as few fabrication iterations as possible*, preferably only one. These two characteristics are the measures of a good flow, because they translate directly to the industry-desirable reductions of the metrics “*time to market*” and “*costs*”.

The exact nature and components of a design flow depends on the engineering technology in question. In the case of MicroElectroMechanical systems (MEMS) one strategy has been to embed the required design tools into a traditional analogical VLSI flow. This approach stems from the need to have a workable solution right away. While it has helped somewhat, it fails to address the significant differences between the design of MEMS and VLSI circuits.

With some exceptions, electronic circuits almost exclusively involve a single physical domain: the electric domain. Other physical domain can be important, but they are not in general, fundamental for the operation of the circuit; instead they manifest themselves as unwanted perturbations of the device behaviour. On the other hand, MEMS can incorporate multiple domains and all these domains are integral to the proper functioning of the device.

Another distinction is the manner in which design intent maps to manufacturing description, namely, a layout. In digital design, intent is described by functionality, using, for example, a hardware description language. In analogical circuits, an explicit description of connectivity is required to capture design intent, usually in the form of a schematic. In both cases, the device connectivity is then mapped into layout, either automatically or manually. In contrast, layout itself is an essential

component in the design intent description for the majority of MEMS devices, because connectivity as well as geometry, orientation, and position of the basic elements is required to adequately describe functionality.

What is more, the system-level or schematic-level view used in the electrical world cannot elegantly capture this information, since the data structures employed are tailored to represent only connectivity information. With such a restriction, it is impossible to adequately study many important aspects of a MEMS design; hence, a new approach is required.

Many efforts have been spent and is currently being spent in proposing specific MEMS design flow [16], and good progress is being made in this area. There is a large body of research devoted to developing tools, engines, algorithms and methodologies to support these flows [17], however, not all that is required is yet available.

In this chapter the key steps of a MEMS design flow are presented together with the tools available on the market to support each step and the open issues in MEMS design.

Indeed section 2.1 describes a generic MEMS design flows by underlying which are the fundamental steps to reach an optimum design flow (a design flow which allows having a right device at first production run).

Section 2.2 presents a brief overview of the tools available on the market to assist the designer during each design phase.

Then section 2.3 and 2.4 are dedicated to the two fundamental steps in MEMS design: modelling and layout. And finally section 2.5 underlines which are the principal challenges in MEMS design.

2.1. MEMS design flow structure

Like most engineering flows, the MEMS design flow begins with a product definition. The definition is based on an idea as well as a general architecture and a feasibility study. Generally the definition also includes an estimation of price and leads to the elaboration of device specifications, that in the specific case of MEMS are parameters such as sensitivity, noise, temperature stability and desired die size.

Once the MEMS specifications are set, a Finite Element Method (FEM) model is developed in order to define the MEMS geometry.

FEM simulations are also performed to extract the characteristic device parameters used to develop a high level MEMS model. A high level MEMS model is necessary because the MEMS and the sensor read out electronics cannot be designed independently. Modelling the interaction of the MEMS with the electronics is often essential to predict the complete system behaviour, and hence compatible models of the sensor and the system must be developed.

In practice does not exist a single level of MEMS model, but modelling occurs at many levels and uses a variety of modelling paradigms, each one selected to be appropriate for that level.

Once the MEMS geometry is completely defined and respects the device specifications, the device layout must be generated. The sensor layout is usually realized by employing the same tools used for the electronics layout and the realization of the layout is the last step before the production as shown in Fig. 18.

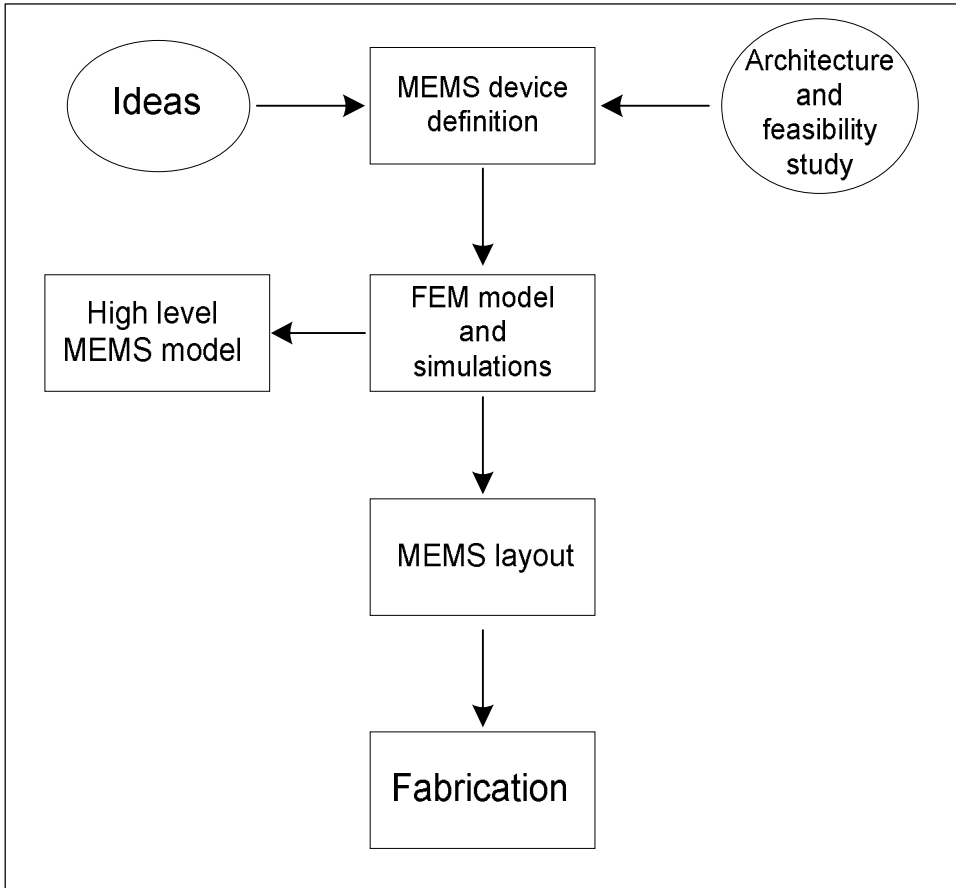


Fig. 18 MEMS design flow block diagram

Before the production step is very important to perform the layout verification in order to discover and correct errors.

Then in order to have an idea of a complete MEMS design flow, it's better modifying the design flow of Fig. 18 by adding a step for the layout check, as shown in Fig. 19: Indeed two actions are fundamental before the production: to verify that the process specifications have been respected in the layout realization through a Design Rule Check (DRC) of the sensor layout and to verify the compliance between the layout realized and the sensor schematic with a Layout Versus Schematic (LVS) check.

Algorithms and tools for MEMS verification are active area of research, but currently no off-the-shelf tools are available. About this argument our proposal to perform a MEMS layout LVS will be presented in the next chapter (Chapter 3).

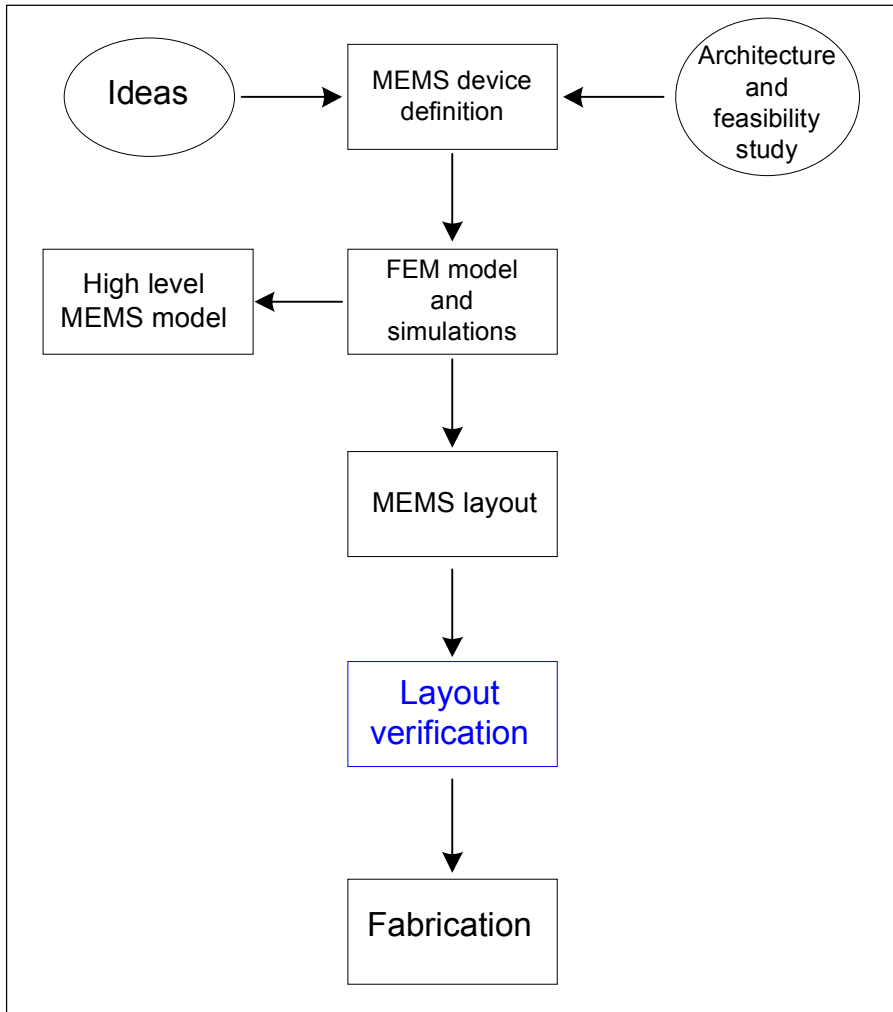


Fig. 19 MEMS design flow block diagram with layout verification step added

Moreover another step that is not mandatory in MEMS design flow but that could be very useful is the layout simulation (this kind of simulations are also called *post layout simulations*). Indeed simulating the layout could be very useful to verify the design correctness. In simulating the layout, the designer will often find some fine-tuning of the mechanical device properties employed in the system level description of the sensor, thus obtaining the information needed to enhance the MEMS high level model. Moreover simulating the layout means simulating a geometry as close as possible to the real device and could be useful to find error in the previous models due to too high approximations.

In conclusion a complete MEMS design flow must included the two additional steps of layout verification and simulation as shown in Fig. 20.

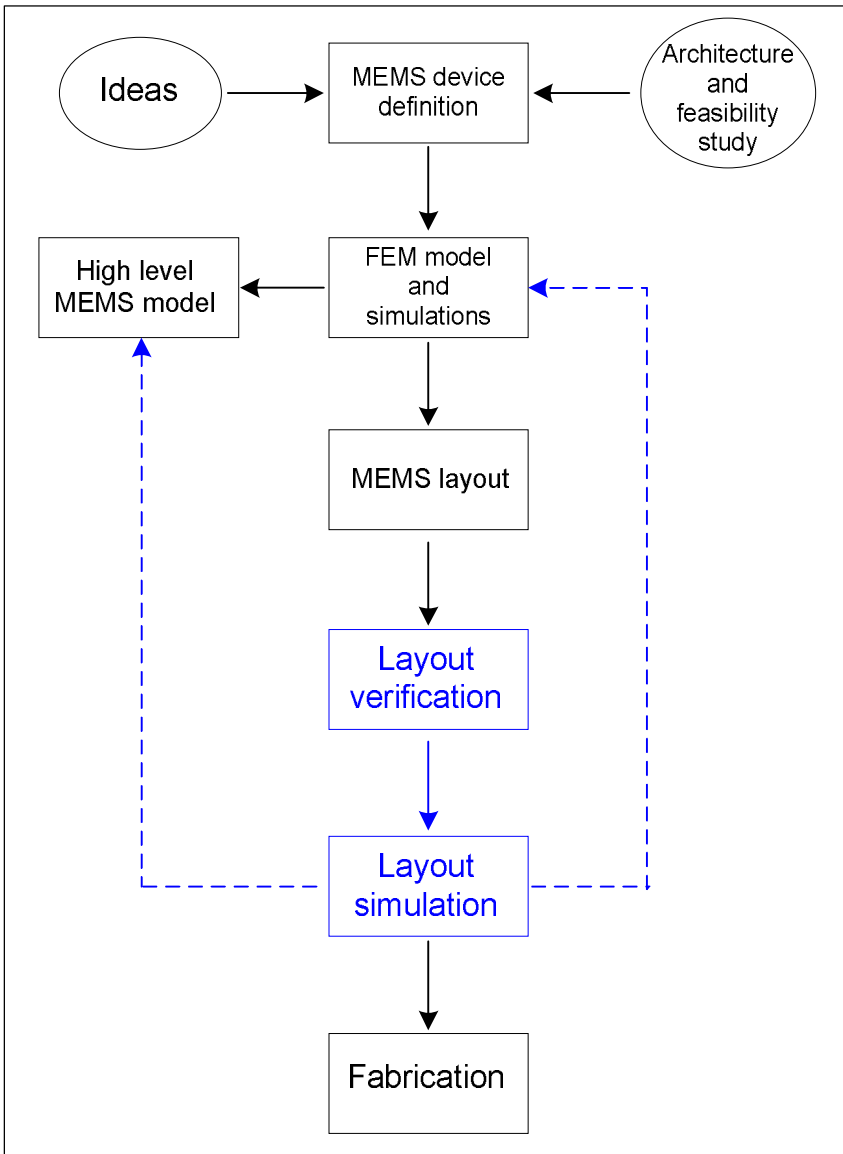


Fig. 20 Complete MEMS design flow. Dashed lines show the interaction between layout simulation and modelling phase.

2.2. CAD tools for MEMS design

In the previous section we have seen which are the fundamental steps in a generic MEMS design flow. Each step could origin a range of problems that the designer must be able to overcome: process simulation, solid-body geometric renderings from photomasks and process descriptions, energetically correct simulation of behaviour across multiple coupled energy domains, extraction of models of device behaviour, optimization of geometry and process sequence, and design compatibility with the full systems that include MEMS devices.

For these motivations is fundamental that for each design flow step the MEMS designer is assisted by the support of Computer-Aided Design (CAD) tools for automating, where is possible, and for helping in creating models which describe in an accurate way the device behaviour at different levels.

The ultimate goal, of course, is to have a device which works as desired at first production run. This goal can be reached more easily if the device behaviour is anticipated through simulation and modelling (also called “computational prototyping”), thus reducing fabrication costs and incrementing fabrication effectiveness.

The strongest driving forces behind the development of CAD tools come from competitive industries, where time and cost-efficient computational prototyping can reduce the total time for a device concept to be converted into a marketable product. The cost of the CAD tools is justified by multiple factors: the net reduction in development cost, earlier market entry, improved understanding of device behaviour and optimization through critical comparison between measured and simulated device performance. CAD tools can play an essential role here in understanding or identifying subtle second-order effects that can easily be missed in the first phases of product design.

A second set of driving forces for MEMS CAD development come from researchers working on advanced concepts, who need CAD tools to try out ideas, even if the primary interest is only to get estimates of device performance rather than the accurate simulations needed for product specifications.

In other words, there are two rather different types of CAD requirements: in the first conceptual phase of a new device, to assist in finding practical configurations, and in the second product-level phase, to enable careful attention to physical behaviour and parasitic phenomena.

In this latter phase, there is a great benefit if the actual device masks and process description can be used as input to the simulations. Rendering of three-dimensional solid models from mask and process data, both to permit checking of geometries and as input to physical simulation, assures that the device being simulated is also the one being built.

In this chapter the focus is on the most common tools available on the market to assist the designer during the phase of simulation of the physical device behaviour, development of a high level model and creation of the layout of the lithographic masks for the final device fabrication.

Due to the physical interdisciplinary nature of MEMS devices the study of their physical behaviour is not an exact analytical process but involves developing engineering models with appropriate CAD tools. A number of available programs, such as **Ansys**TM (ANSYS, Inc. of Canonsburg, Pennsylvania [18]),

CoventorWare™ (Coventor, Inc. of Cary, North Carolina [19]) and **IntelliSuite** [20] can simulate mechanical, thermal, and electrostatic structures (see Fig. 21).

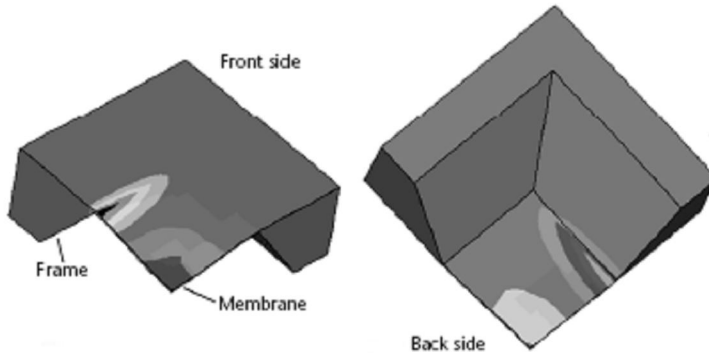


Fig. 21 A finite element simulation using ANSYS modelling program of a quarter of bulk micromachined silicon pressure sensor showing contours of mechanical stress in response to an applied pressure load.

Ansys™ is essentially a comprehensive general-purpose finite element computer program (finite element tool will be described more in detail in section 2.3.1) capable of performing static, dynamic, heat transfer, fluid flow and electromagnetism analysis. It has been a leading finite element analysis tool for well over 20 years and today is in use in many engineering fields such as aerospace, automotive, electronics and nuclear.

On the other hand Coventor Inc. is a developer of MEMS design automation software which proposes an alternative solution to traditional finite element analysis tools: CoventorWare. **CoventorWare™** is a fully integrated design environment for MEMS design. It includes different modules: a first module called “architect” to quickly evaluate the MEMS behaviour and the surrounding electronics within a schematic-based system-level modelling environment, a second module called “designer” to create layout masks, to define the fabrication process and automatically generate a 3D model as input for a third module which is called “analyzer” and is used to understand and verify MEMS design. Finally a fourth module called “integrator” is used to create linear and non-linear reduced order models that are compatible with standard IC simulators.

Another MEMS CAD package currently present on the market is **IntelliSuite™** commercialized by Intellisense Corning. It is a FEM-based simulation and design tool specifically developed for MEMS and it runs on a standard PC under Windows. The user starts drawing the masks in IntelliMask, which is a standard drawing package with typical features for mask design. Each mask is drawn on separate layer and saved in a different file. The next step is to define the fabrication process in a tool called IntelliFab. It contains a large database of silicon base materials, deposition steps of various materials, and etching steps for all commonly used materials in MEMS. The previously defined masks are used to define areas in which material is removed or added. Once the user has created the full process flow (referred to as Process Table) IntelliFab visualizes the fabricated device in an easy-to-use viewer that allows zooming, panning, and three-dimensional rotation of the virtual prototype. The various simulation solvers, which are mechanical,

electromagnetic, electromechanical and electrostatic, can be run either from IntelliFab or directly and allow studying and analyzing of the MEMS behaviour.

An alternative to the use of complete tools suites such as CoventorWare and Intellisuite, which allow to simulate MEMS behaviour at different design levels and to build up the layout, is the integration of FEM tools such Ansys with other tools for high level model development and layout realization.

CADs which are widely used to build up a system model of MEMS device in order to design the conditioning and read out MEMS circuitry are **Matlab**TM and a particular MatlabTM module which is called **Simulink**TM. SimulinkTM is an environment for multi domain simulation and model-based design, it is integrated with MatlabTM and it is suitable for system design, implementation, verification and validation tasks as will be seen more in detail in section 2.3.2.

Finally a CAD class essential for building MEMS is represented by the tools specialized in the realization of the mask for the fabrication of the device. In this field for example **Cadence**TM is an integrated circuit CAD package that also provides MEMS layout synthesis tools (such as **Virtuoso**). Indeed even if Cadence package is not specific for MEMS application it can be used also to perform MEMS layout.

2.3. MEMS modelling

Modelling and analysis of devices and systems is a complex subject. Modelling occurs at many levels and uses a variety of modelling paradigms, each one selected for the appropriate level.

We can identify four modelling levels: System, Device, Physical and Process each linked to the next with double-headed arrows symbolizing iterative exchange of information between levels (see Fig. 22).

At the top is the system level, we start from the system level because a MEMS must be always integrated in a conditioning or read out system, then is essential to model the MEMS behaviour together with the system. The system level is the home of block-diagram descriptions and lumped-element circuit models, either of which can be used and both of which lead to a coupled set of *ordinary differential equations* (ODE's) to describe the dynamical behaviour of the system. Often these equations are written in a specific form as a coupled set of first-order ordinary differential equations for the state variable of the system. In this form the equations are referred as *state equations* for the system. The tool usually employed for system level models is SimulinkTM.

At the bottom is the process level. This is where the process sequence and photomask designs for device manufacturing are created. Process modelling at this level is a highly sophisticated numerical activity for which a number of commercial CAD tools have been developed, they are generically referred as *technology CAD* or *TCAD* [21]. For the MEMS designer the importance of TCAD is that it can predict device geometry from the mask and process sequence. Moreover, because the material properties can depend on the detailed process sequence, the designer must know the proposed process in order to assign the correct material properties when modelling the device.

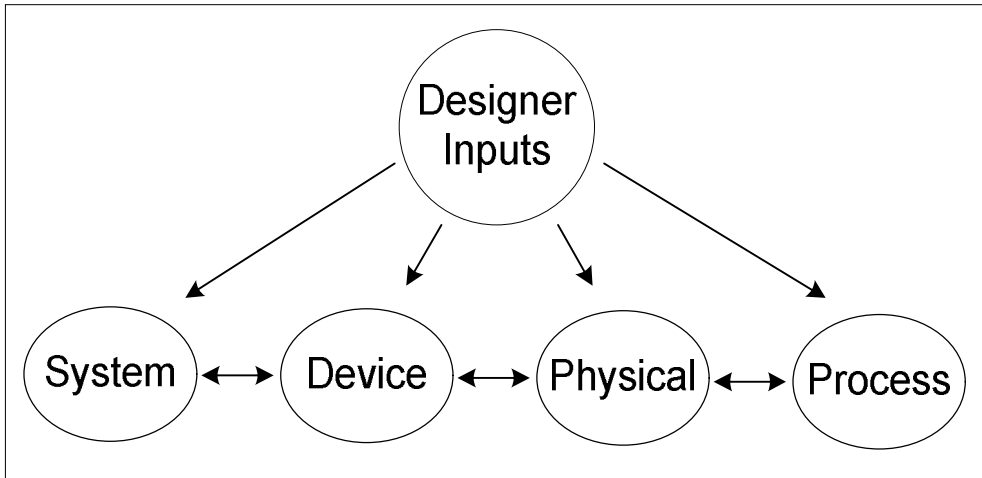


Fig. 22 Different modelling levels for microsystems

The *physical level* addresses the behaviour of real devices in the three dimensional continuum. The governing equations are typically *partial differential equations (PDE's)*. Various analytical models can be used to find closed-form solutions in ideal geometries, but the modelling of realistic devices usually requires either approximate analytical solutions to the PDE's or highly meshed numerical solutions. A variety of numerical modelling tools using either finite-element, boundary-element or finite-difference methods are available for simulations at the physical level. Indeed modelling of electrostatic forces [22], mechanics behaviour, coupled electromechanics and damping effects is relatively mature with commercial finite-element and boundary-element tools available to construct reduced-order behavioural models. Examples of finite element method tools for MEMS simulation are AnsysTM, Comsol MultiphysicsTM, MEMSCAP and CoventorWaveTM package.

While the numerical representations of PDE's of the continuum physics are useful in physical simulations, such representations are typically too cumbersome when dealing with the entire device and their associated circuitry. Instead we go the *device level* and we create what are called *macro-model* or *reduced-order-model*. These models capture the essential behaviour of the components of the system and simultaneously are compatible with a system level description. An ideal macro model is analytical rather than numerical, the macro model should capture the essential device behaviour in a form that permits rapid calculations and insertions into a system level simulator (again for the device model either a block diagram description in SimulinkTM and a lumped element circuitual description can be used). The macro-model should be energetically correct, conserving energy when it should and dissipating energy when it should. It should have the correct dependence on material properties and device geometry. It should represent both static and dynamic device behaviour, both for small-amplitude (linear) excitation and large-amplitude (non linear) excitation. Finally the macro-model should agree with the results of 3D simulation at the physical level, and with the results of experiments on suitable test structures.

Fig. 22 shows an important feature: the fact that the “designer inputs” may occur at every level. The designer can create models directly at the system level, or directly at any other lower level. For example, the designer could start from a physical device description with all the device dimensions and the material properties and then use physical simulations tools to calculate device behaviour, capture this behaviour in a reduced-order model and finally insert it into a system-level block diagram. Or alternatively the designer could simply use a parameterized reduced-order model to represent a particular device and defer until later the specification on device dimensions to achieve the desired performance.

In conclusion modelling is fundamental in MEMS design because through modelling the designer hopes to learn a deal about system and device before the relatively costly step of building experimental prototypes this is why modelling is often called “numerical prototype”.

2.3.1. Finite Element Method for MEMS modelling

In the previous paragraphs we have seen that numerical methods are suitable for the analysis of the physical MEMS behaviour. Indeed due to both the complex nature of MEMS governing differential equations and the difficulties in dealing with the boundary and initial conditions for most of MEMS problems we cannot obtain an exact solution and we need a numerical approximation.

In contrast to analytical solutions, which show the exact behaviour of a device at any point within the system, numerical solutions approximate exact solutions only at discrete points called nodes. There are two common classes of numerical methods: *finite difference method* and *finite element methods*.

With *finite difference method*, the differential equations are written for each node, and the derivatives are replaced by difference equations. This approach results in a set of simultaneous linear equations. Although finite difference methods are easy to understand and employ in simple problems, they become difficult to apply to problems with complex geometries or boundary conditions.

On the other side, the *finite element method* uses integral formulation rather than difference equations to create a system of algebraic equations. With this method, a continuous function is assumed to represent the approximate solution for each element. The complete solution is generated by connecting the individual solutions thus allowing for continuity at the interelemental boundaries.

Finite element method can be applied to obtain solutions for a wide variety of problems in engineering. Steady, transient, linear, or non linear problems in stress analysis, heat transfer, fluid flow and electromagnetism problems may be analyzed with finite element methods.

The modern finite element method is born in the early 1900 when some researchers approximated and modeled elastic continua using discrete equivalent elastic bars. However Courant (1943) has been credited with being the first person to develop the finite element method [23]. In a paper published in the early 1940s, Courant used piecewise polynomial interpolation over triangular subregions to investigate torsion problems.

The next significant step in the story of finite element method was in the 1950s, when Boeing, followed by others, used triangular stress elements to model airplane wings. But only in the 1960s Clough made the term *finite element* popular. During 1960s the finite element method began to be applied to others engineering areas,

such as heat transfer and seepage flow problems. Zienkiewicz and Cheung (1967) wrote the first book entirely devoted to the finite element method in 1967.

Nowadays one of leading finite element method toll is Ansys, it was released for the first time in 1971 and today is used in a wide variety of engineering problems and also in MEMS developing and analysis.

Indeed Ansys Multiphysics has an extremely broad physics capability applicable to many areas of microsystem design. Coupling between these physics enables accurate, real world simulation of devices such as electrostatic comb drives for example. Moreover the ability to compute fluid structural damping effects is critical in determining the switching response time of devices such as digital micromirrors. Electro-thermal-structural effects are employed in thermal actuators and many others examples could be listed. While not specifically written for the simulation of MEMS, many of these analyses apply equally well in the microdomain, and ANSYS has been widely used throughout the MEMS community. The software interface has evolved over many years, and the latest ANSYS Workbench environment is now relatively straightforward to use even for the novice. The software also allows CIF files to be imported, thus enabling MEMS designs to be input from other software packages. By selecting the correct element, the anisotropic material properties of silicon can input in matrix form enabling accurate materials specification in the simulation.

Another finite element method tool presents on the market which allows multithysics simulations to be performed is Comsol Multiphysics. Also this tool has the capability to coupling different physical worlds which is a key issue in simulation of the microelectromechanical system. Comsol Muthiphysics is younger then Ansys and less diffused but in the last years it is expanding in university environment, research group and industry.

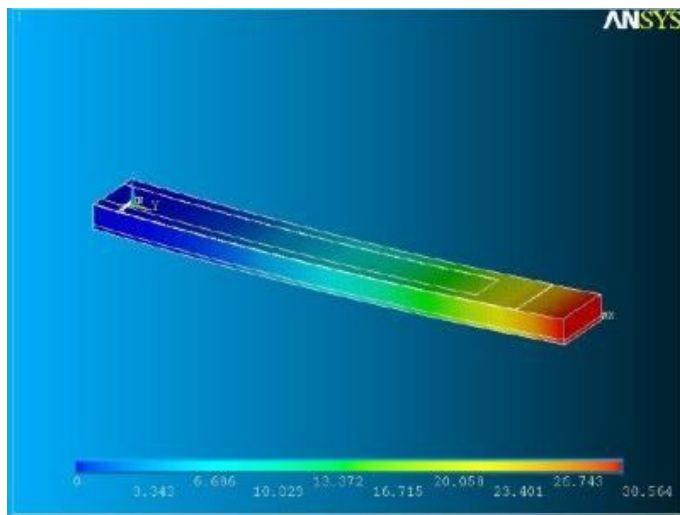


Fig. 23 Strain distribution at neutral stage of a microprobe study and modeled with Ansys [24]

2.3.2. Behavioural modelling: Simulink™ tool

One of the most popular behavioural modelling tools is Simulink™, which is a toolbox within Matlab [25]. It allows the user to perform system level simulations in the time domain. The user chooses blocks from a library that includes linear and nonlinear functions, which are either time continuous or discrete. Examples include gain, integrators and differentiators, z- and s-domain transfer functions, limiters, samplers, mathematical functions, switches, and many others.

Each block has a range of input and outputs. An input can be the output of another block or a source that can be an arbitrary waveform. Any output of a block can be visualized by different types of plots in the time or frequency domain; alternatively it can be stored as a variable to be analyzed or filtered further in Matlab. The software allows user-defined library and hierarchal modelling by defining parameterized subsystems. The software has a purely graphical interface; blocks are chosen by drag and drop and connected by wires drawn on the screen.

As an example the model of the mechanical sensing element of an accelerometer is shown in Fig. 24. The mechanical sensing element can be described by the differential equation of a mass-dashpot-spring system. Furthermore, it will be assumed that the proof mass is limited in its travel range by mechanical stoppers and that it has an optional deflection from its rest position at the start of the simulation. The input is an external inertial force and the outputs are the displacement, velocity, and acceleration of the proof mass as a response to the input force. The model contains a user-defined submodel (“displacement limit controller”) that has two inputs: the input acceleration acting on the sensing element and the displacement of the proof mass. It models the nonlinear behaviour of the sensing element in case the proof mass touches the mechanical stoppers (i.e., the displacement x exceeds a certain x_{max}). In this case the velocity of the proof mass is reduced to zero, hence Integrator1 in Fig. 24 is reset to zero until an acceleration in the direction away from the limit stopper is detected.

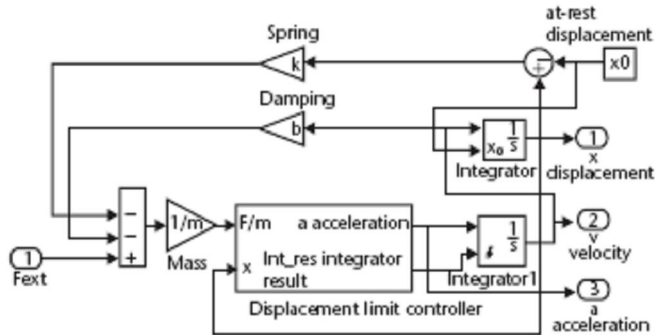


Fig. 24 Simulink model of the sensing element of a micromachined accelerometer. The sensing element is a mass-dashpot-spring system including mechanical stoppers and initial deflection.

Another feature of the model is that a nonzero initial displacement of the proof mass can be set by x_0 , which puts an initial condition on the second integrator. The summing block at the input sums up all external and internal forces acting on the proof mass.

The model of the sensing system can be included in the whole sensor model together with the model of a force-feedback control loop, thus allowing an optimization of the sensor parameters, prediction of the control loop stability and study of secondary order effects. A typical methodology is to start with a basic model, capturing only first order effects, then adding various second order effects and evaluating their influence on the performance of the device. Those that have a negligible effect on the sensor can subsequently be discarded again to speed up the simulation.

The accuracy and merits of such an approach obviously rely on the analytical understanding of the underlying physics of the sensor to be simulated. The modelling process typically is done analytically by the designer, often by hand calculations. Nevertheless certain FEM software tools automate this process by performing, for example, a full mechanical modal analysis, and then extracting a lump parameter model that is suitable for implementation in a system model and in a system simulation tool.

2.4. MEMS layout

The MEMS layout is the last step before the device production.

In Chapter 1 we have seen which are the main MEMS microsystem technologies which lead to the fabrication of a MEMS device.

Briefly a MEMS process is based on the different steps of deposition, pattern and etching whose result is a device similar to the one shown in Fig. 25.

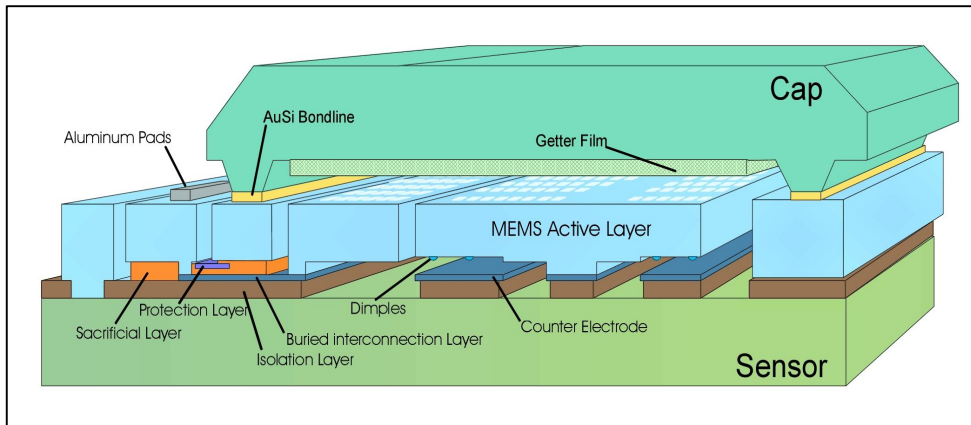


Fig. 25 Schematic representation of a MEMS physical process

A structural layer of polysilicon (called epi poly and characterized by typical thickness of 11 μm) is used to build the moving structure of the MEMS (light blue in Fig. 25). This moving structure is suspended over an etched pit and is anchored to the substrate with well defined anchor points. The position of these anchors define the MEMS motion which can be characterized by a rotating motion or/and a tilting motion. If the device is a capacitive structure, as the device shown in Fig. 25, electrodes positioned under the moving structure are used to detect the motion through the capacitance variation between the moving structure and the electrodes

themselves. The electrodes are made up of thin polysilicon (typical 100nm thick) defined as buried poly (blue layer in Fig. 25.).

The different signals are applied to the different mechanical structures by using appropriate connections between the mechanical parts and the MEMS pads. These connections are realized with both epi poly and buried poly paths which are vertically connected through “vias”.

Finally the MEMS is covered with an appropriate package.

In conclusion all MEMS processes are based on the same phases which basically are: deposition, patterning and etching. These standard steps allow the developing of a layered abstraction, where each layer represents a process step. For the process described in Fig. 25 the correspondent layers are shown in Fig. 26.






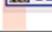

Mask	Layer	Polarity	Function	Color Code (LSW)
S1	BP	c	Definition of first metallization level	 BP <input type="text" value="dg"/>
S2	OX	d	Contact definition between BP and EP	 OX <input type="text" value="dg"/>
S3	UO	d	Contact between EP and Substrate	 UO <input type="text" value="dg"/>
S4	EP	c	Definition of thick Epi-Poly	 EP <input type="text" value="dg"/>
S6	AL	c	Definition of Pad-Contact	 AL <input type="text" value="dg"/>
S7	PL	c	Protection of BP-wiring inside capframe at sawing process	 PL <input type="text" value="dg"/>
S8	DI	d	Definition of dimples to avoid vertical contact of moving structure with BP	 DI <input type="text" value="dg"/>

Fig. 26 Layout layers characteristic of a typical MEMS process

Then each process can be defined in terms of the manufacturing steps needed for each layer together with the characteristic properties of the material used and the geometrical dimensions of the layers.

In the MEMS design methodology this information is captured in a layout technology file and a layout design rules file which customize an appropriate layout toll.

Layout tools for MicroElectroMechanical systems (MEMS) have often posed a challenge for the MEMS designer due to the interdisciplinary nature of MEMS development.

Various types of software programs that were not originally intended for MEMS purposes have been used as layout tools (e.g. the Virtuoso tool of Cadence™ environment). Most of these tools have evolved from the IC world, where rectangles make up typical geometries. Although there have been recent innovations in the development of MEMS layout tools, MEMS layout designers still face some common issues and roadblocks while attempting to create lithographic masks that correspond with the original device design, specifically in the areas of drawing, design rule checking (DRC) and output.

In many cases, the mechanical/optical/fluidic nature of MEMS structures involves arbitrary geometries composed of arcs, curves, circles and other multi-polygonic shapes. Unfortunately, such geometries have not traditionally been the focus of IC layout tools. For example, if the software supports full curves and multi-polygons, the layout designer must still have a thorough understanding of how the data is

fractured by the mask house to ensure that the electronic file resolution is replicated on the physical quartz mask.

In addition, understanding the three-dimensionality of the topography is required. This is because unlike most VLSI (very large-scale integration) processes, MEMS processes have a much wider range in the thickness of the thin film (about 10 micrometers versus one micrometer).

Then a host of features differentiate MEMS layout tools from those of the IC field, due to the free-form nature of MEMS structures. First, the ability to draw curves or all-angle polygons (i.e. commands that enable arcs, circles, Bezier curves) is a departure from the rectangle-focused IC tools. Most IC-based layout tools do not support the precision drawing of curves and often times the user must create additional macros in order to define accurately the geometry. Second, the ability to snap, measure and accurately edit these free-form polygonic shapes becomes tedious because most layout tools are grid-based. Third Boolean operations are very important in MEMS layout realization. Indeed Boolean drawing operations enable the designer to use logical and other operations (e.g. AND, OR, NOT, XOR, GROW, SHRINK, SUBTRACT) to create new shapes from arbitrary polygons. These operations can be used to create entirely new layers (derived layers) from existing ones. For example, a mask for a flow channel may require a 10micron border of metal all around it. Using the Boolean algorithm, the designer would only require one command to grow a new layer and subtract it from the original layer. Any subsequent change in the original flow channel would automatically be generated in the new derived layer.

Another main difference between IC geometries and MEMS geometries is the magnitude of range in size. While typical transistor blocks may cover 20x20 micrometers areas, MEMS geometries may have 5 micrometers features, and an overall dimension of 1mm. This wide range in size can result in constant zooming in and out during the design process. Thus, some MEMS designs require the ability to snap to corners, midpoints or user specified relative distances without zooming in.

Finally as MEMS processes become more standardized and devices gain complexity, DRC (Design rules check) and LVS (layout versus schematic check) can be used to find errors before tape-out. While these tools have always existed for IC designers, they typically are not used in MEMS. The free-form nature of the MEMS processes results in varying design rules depending on the MEMS fab and associated tooling, and many DRC tools are not able to perform operations on all-angle polygon geometries. The implementation of these tools also for MEMS is required to have a more reliable design flow.

2.5. Challenges in MEMS design

As described in the previous sections the design flow of a microelectromechanical sensor (MEMS) is made up by four fundamental steps:

1. MEMS definition (starting from an idea the device specifications are defined);
2. elaboration of a FEM (Finite Element Method) model to simulate and understand the physical MEMS behaviour;
3. design of the sensor layout (for the physical sensor realization);
4. MEMS fabrication.

In order to reduce as much as possible production costs and time to market it is fundamental to have an optimized design flow..

The top-level goal of a design flow is to enable complex engineering design in *as short time as possible* and with *as few fabrication iterations as possible*, preferably only one. These two characteristics are the measures of a good flow, because they translate directly to the industry-desirable reductions of the metrics “*time to market*” and “*costs*”.

Then the optimum design flow allows having a right MEMS sensor which matches design specifications with only one production run.

Unfortunately in most cases this does not happen. Indeed in practice more runs are necessary to obtain a working sensor due to errors in the sensor layout and/or wrong approximations in the FEM simulations, resulting in increasing production costs and development time.

In order to have a design flow as close as possible to the optimum one, two steps must be added before the production, the *layout verification* and the *layout simulation*.

Layout verification is fundamental to check the layout before the production, indeed DRC (Design Rules Check) and LVS (Layout Versus Schematic check) are fundamental to find errors before tape-out that otherwise can not be found due to the complexity of the MEMS designs.

In the same way layout simulation are very useful to guarantee a successful MEMS design, since in simulating the layout the designer can often better determine the MEMS mechanical properties thus allowing a fine tuning of the system level sensor model.

Algorithms tools for MEMS layout verification are active area of research, but currently no-shelf tools are available, hence custom tools must be developed.

In the same way even if layout simulations (also called post layout simulations) are very important, there is not a well define methodology to perform post layout simulations in a quick and reliable way.

From these issues the necessity arises to support the MEMS designer with proper design tools and guidelines in order to verify correctness of the layout and to perform post layout simulations. These issues need to be addressed developing ad hoc solutions as shown in the next chapter.

CHAPTER 3

AUTOMATIC TOOLS AND METHODOLOGIES FOR MEMS DESIGN FLOW ENHANCEMENT

As shown in the first chapter, nowadays MEMS (Micro Electro Mechanical Systems) devices are employed in many areas, such as biomedics, communication, automotive, and optic. The increasing success of these systems is due to their low power consumption, low manufacturing cost and high miniaturization capability thus allowing for an easy integration with electronic circuits.

In order to have a further reduction of production costs and time to market the MEMS design flow must be as close as possible to an optimum design flow, where optimum design flow means to have a working MEMS ready for the market at first production run.

A MEMS design flow generally is organized as follows: definition of the MEMS geometry and the device specifications, elaboration of a Finite Element Method (FEM) model that can be simulated with appropriate finite element method tools, MEMS layout realization and finally physical sensor production.

In the case of optimum design flow measures performed on the manufactured sensor should match the results obtained from simulations performed on the sensor model, but unfortunately in most cases this does not happen. The reasons of this failure lie in wrong model approximations, which lead to unreliable simulation results, and/or layout errors. If the sensor produced is wrong or does not match the design specifications a redesign step is needed (to fix the errors) together with a new production run, resulting in higher production costs and development time.

From these issues arises the necessity to support the MEMS designer with appropriate tools and guidelines which allow the precision of the simulation model and the correctness of the layout to be verified before the production.

In this chapter an automatic tool for performing LVS (layout versus schematic) check of MEMS is presented (section 3.1), the tool has been developed within the same environment usually adopted to realize the MEMS layout (Virtuoso tool of Cadence package) and its working principle is based on the comparison between the sensor layout and a schematic which represents the sensor itself. In addition an extension of the tool allows the generation of a GDSII file where sensor regions characterized by different electric potentials are highlighted with different colours thus providing a quick way for checking shortcuts.

As mentioned before another crucial step in MEMS design flow is the elaboration of a model as close as possible to the real device. In order to reach this goal, a

methodology to perform post layout simulations has been developed and is presented in the second section of this chapter (section 3.2). Post layout simulations are FEM simulations performed on the real sensor layout extracted from Cadence environment and are very useful in better discovering mechanical properties of the sensor thus allowing a fine tuning of the sensor model in order to obtain a model as close as possible to the real sensor device.

Moreover to reach the goal to have a sensor model that reflects the real sensor behaviour, some secondary effects that can only be known after the layout realization must be taken into account, such as the parasitic capacitances. In order to address this issue a further tool has been developed for the automatic extraction of the MEMS parasitic capacitances (section 3.3).

Both LVS check and post layout simulations together with the tool for parasitic capacitance extraction were successfully applied to real gyroscopes manufactured at Fraunhofer Institute for Silicon Technology (Itzehoe, Germany). Indeed LVS check has been very useful in detecting shortcuts and other layout errors before producing the devices while post layout simulations were useful to correct the sensor model and, when required, redesign the sensor before manufacturing.

3.1. ASSURA tools for MEMS LVS check and connectivity extraction

3.1.1. ASSURA tool for MEMS LVS: working principle

The tool to perform the sensor layout check has been developed in the same environment offers by Cadence™ to perform the layout of electronic circuit (the Virtuoso™ tool) and its working principle is based on the comparison between the sensor layout and the schematic which represents the sensor itself. In practice the tool performs a LVS (layout versus schematic) check of the sensor by using the same environment already present to perform the LVS of an electronic circuit (ASSURA™ tool for physical verification) and by customizing this environment with an appropriate rules file created ad hoc for electromechanical sensors.

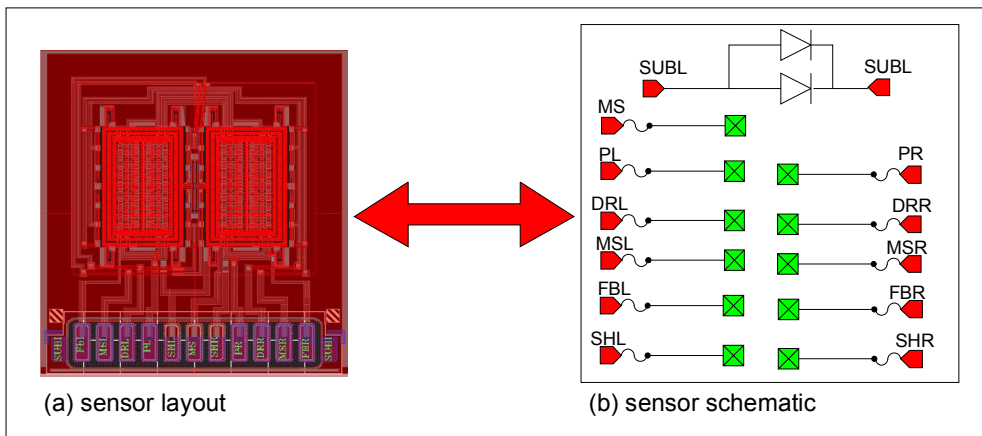


Fig. 27 LVS tool working principle (comparison between sensor layout and sensor schematic)

This rules file is developed in ASSURA language and establishes the connectivity inside the sensor layout in order to realize the following features:

1. verify shortcuts between different sensor pads;
2. verify if any structure is not biased (floating);
3. verify if each pad is connected to the correct sensor structure;
4. other secondary features (e.g. to calculate electric field between structures characterized by different electric potential).

With the support of this tool the layout designer can keep under control his work and correct errors before the production. Let's see now in detail how this working principle is implemented.

The steps needed to perform the MEMS LVS are:

1. create a new sensor layout in which PIN names are added;
2. open the tool already present in Cadence to perform the electronic circuit LVS (Assura tool);
3. load the rules file created ad hoc for electromechanical sensors.

Starting from the sensor layout ready for the foundry, a new layout view must be created in which the sensor pin names are added to the original layout together with a dummy resistor for each sensor pin (Fig. 28). This step is fundamental because otherwise the LVS tool can not establish the connectivity inside the sensor.

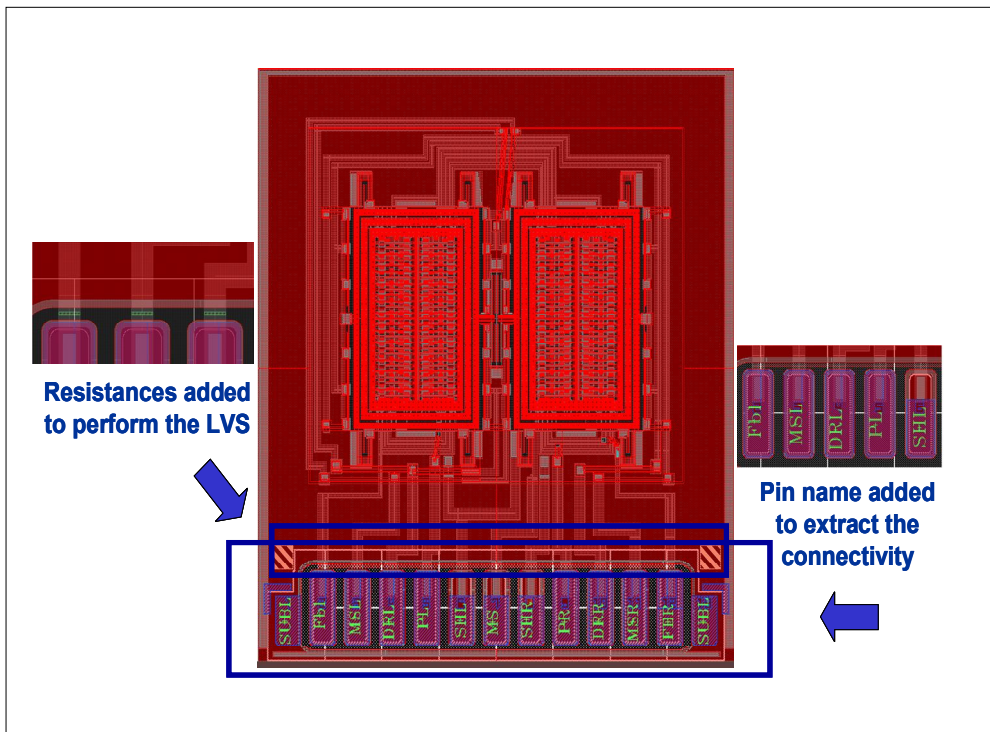


Fig. 28 A Dummy resistance for each pin and the pin names must be added to the sensor layout before performing the LVS

Once the sensor layout has been prepared as described at step 1, the LVS check can be performed by opening the LVS window in ASSURA environment and by loading the rules file developed ad hoc for electromechanical sensors. At this point the LVS can be performed and as result will be produced a report in which all the errors are reported.

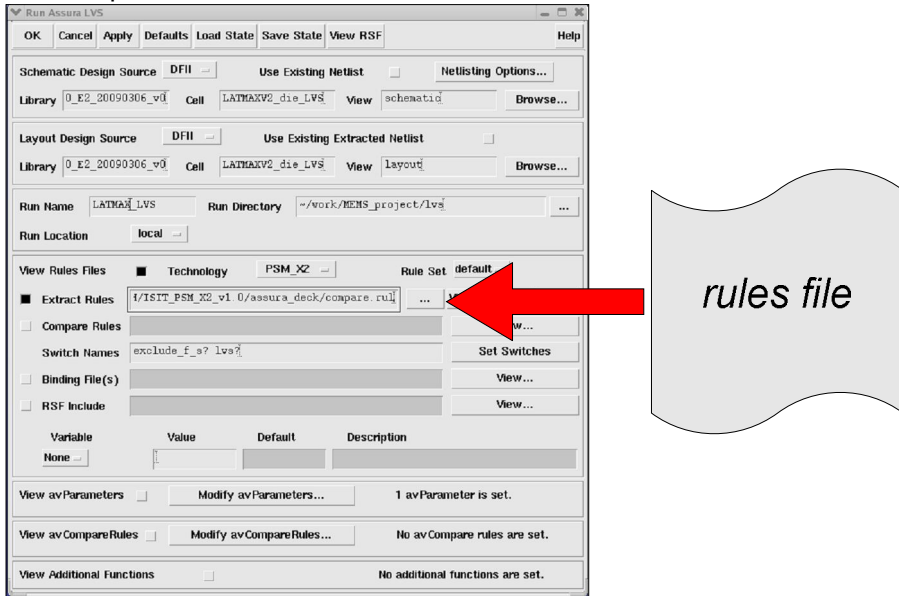


Fig. 29 Rules file loading in LVS Cadence environment

3.1.2. ASSURA tool for MEMS LVS: rules file

The rules file is the core of the LVS tool, it extracts the connectivity inside the MEMS layout and verifies that there are not layout errors. The file structure can be divided in three sections:

1. in the first section there are the commands for the physical layers declaration (the physical layers are the ones used in the sensor layout) and for the creation of derived layers used to perform LVS check (Fig. 30 (a)).
2. In the second section there are the commands which perform the fundamental LVS operations. This sequence of commands extracts the connectivity inside the sensor layout and checks the presence of shortcuts or floating structures. In presence of one of the two aforementioned situations a layer error is generated that is used to have a visual indication of where the error is (Fig. 30 (b)).
3. In the third section some switches are defined to enable or disable further LVS features. From the LVS window is possible to enable for example the switch defined as “high_E”. (high electric field). This switch enables the calculation of electric field between structures with different potential in the sensor in order to find the sensor zones affected by high electric field. Another example is the switch defined as “exclude_fo” (false open exclusion), this switch customizes the LVS run in order to exclude false open in the sensor layout, this means that all the geometric structures that have a

distance lower than the process resolution are considered as one single structure (Fig. 30 (c)).

```

;data/tools/DKIT/ISIT_TECH/ISIT_PSM_X2_v1.0/assura_deck/compare.rul
File
Help 160

;metall_df2 = layer( "metall" )
;metall_dg = layer( "metall" type( "drawing" ) )

drcExtractRules(
  layerDefs( "df2"
    EP_d = layer( "EP" type( "drawing" ) )           ;; buried poly
    PL_d = layer( "PL" type( "drawing" ) )           ;; protection layer
    OX_d = layer( "OX" type( "drawing" ) )           ;; oxide
    EP_d = layer( "EP" type( "drawing" ) )           ;; epi poly
    AL_d = layer( "AL" type( "drawing" ) )           ;; aluminum for pads
    UO_d = layer( "UO" type( "drawing" ) )           ;; unknown
    Al_pin_text = textTOPin( "AL" type( "pintext" ) ) ;; label definition
    BP_s = layer( "BP" type( "markerR" ) )           ;; layers to extract resistances
  )
  BULK1 = geomBkgnd()
  BULK = geomSize( BULK1 0.005)

  ;;;;;;;;;;;;;;EP_UO_d = geomAnd( EP_d UO_d )

  ;; extraction of neg. protection layer to extract diodes for bulk connection
  ;;PL_neg = geomNot( PL_d )
  ;;UO_ext = geomEnclose( PL_neg UO_d )
  UO_device = geomAnd( UO_d BULK)

  ;; definition of layer to extract resistances immediately after pad connection (except for SUB connection)
  BP_d_red = geomAndNot( BP_d BP_s )
  pad_connection = geomAnd( BP_d BP_o)

  ;; when OX is over PL the contact between EP and BP is not active
  OX_red = geomAndNot( OX_d PL_d )

  ;; definition of vias between epi and buried poly
  BP_vias = geomAnd( BP_d_red OX_red )
  EP_BP_vias = geomAnd( EP_d BP_vias)

  ;; check EP and BP overlap of oxide
  )
  
```

(a)

```

;data/tools/DKIT/ISIT_TECH/ISIT_PSM_X2_v1.0/assura_deck/compare.rul
File
Help 160

;;;;;;;;;;;;;; lvs? switch section ;;;;;;;;;;;;;;

)

if( avSwitch( "lvs?" ) then
  BP_PL_mixed = geomAnd( BP_d_red PL_d )
  geomStamp( BP_PL_mixed BP_d_red )
  EP_conn_sub = geomNodeRelate( EP_d UO_d conn )
  geomStamp( EP_conn_sub UO_d )
  EP_conn_intnode = geomNodeRelate( EP_d BP_PL_mixed conn )
  geomStamp( EP_conn_intnode BP_PL_mixed )
  EP_conn = geomOr( EP_conn_sub EP_conn_intnode )
  FP_sconn = geomAndNot( EP_d EP_conn )
  geomStamp( EP_conn EP_d )

  BP_conn_sub = geomNodeRelate( BP_d_red EP_conn_sub conn )
  geomStamp( BP_conn_sub EP_conn_sub )
  BP_conn_int_node = geomNodeRelate( BP_d_red BP_PL_mixed conn )
  geomStamp( BP_conn_int_node BP_PL_mixed )

  BP_conn = geomOr( EP_conn_int_node BP_conn_sub )
  BP_sconn = geomAndNot( BP_d_red BP_conn )
  geomStamp( BP_conn BP_d_red )

  errorLayer( BP_sconn "floating BP" )
  errorLayer( EP_sconn "floating EP" )

  extractDIODE( "diode" UO_device EP_d( "PLUS" ) BULK( "MINUS" ) cellView "diode symbol" flagMalformed )
  extractRES( "short" pad_connection BP_d_red( "PLUS" "MINUS" ) cellView "short symbol" flagMalformed )
  saveProperty( pad_connection "R" 100 0e-6 )
)
)

```

(b)

```

..... exclude_f_s? switch section .....
if( avSwitch( "exclude_f_s?" ) then
    ;;layers extracted to avoid false short due to few nm separation between same conductive layers
    geomConnect(
        label( AL_pin_text AL_d )
        butt0rOver( AL_d EP_d )
        via( U0_d BULK EP_d )
        via( EP_BP_vias BP_d_red EP_d )
    )
    EP_patch = drc( EP_d_sep < 0.5 diffNet opposite )
    BP_patch = drc( BP_d_red_sep < 0.5 diffNet opposite )
    geomConnect(
        label( AL_pin_text AL_d )
        butt0rOver( AL_d EP_d )
        via( U0_d BULK EP_d )
        via( EP_BP_vias BP_d_red EP_d )
        butt0rOver( EP_d EP_patch )
        butt0rOver( BP_d_red BP_patch )
    )
    else
    geomConnect(
        label( AL_pin_text AL_d )
        butt0rOver( AL_d EP_d )
        via( U0_d BULK EP_d )
        via( EP_BP_vias BP_d_red EP_d )
    )
)
..... high_E? switch section .....
if( avSwitch( "high_E?" ) then
    EP_patch = drc( EP_d_sep < 0.8 diffNet )
    EP_electrical = geomOr( EP_d EP_patch )
    geomStamp( EP_electrical EP_d )
    drc( EP_electrical 0.8 < sep < 1.8 diffNet "attention possible high electric field between different nodes in epi poly" )
)
    
```

(c)

Fig. 30 Rules file for MEMS layout versus schematic check

3.1.3. ASSURA tool for connectivity extraction: working principle

The Assura tool for connectivity extraction can be considered an extension of the Assura tool to perform LVS. The aim of the ASSURA tool for connectivity extraction is to have a simple procedure to create, starting from the sensor layout, a GDSII file in which each sensor layer corresponds to a pin connection. In this way simply visualizing the “GDSII connectivity file” with a layout viewer (such as CleView™ or KLayout™) it’s possible to see the different sensor connections in order to check the layout (investigating errors, shorts or asymmetries). This tool is not thought for who makes the layout (which can check the layout simply performing an LVS run) but for the designer who studies the FEM model of the sensor. In fact usually who studies the MEMS model and performs FEM simulations is not who realizes the MEMS layout, and is not familiar with tool such Virtuoso. In this way the model engineer can visualize the GDSII connectivity file provided by the layout engineer and check how the sensor has been realized without using tools and procedures specific for layout realization.

As in the previous case the tool uses the environment already present in Cadence™ to perform the design rules check (DRC) of electronic circuits (Assura tool in Virtuoso environment), this environment is customized with a rules file and an RSF file created ad hoc for the GDSII extraction.

The ASSURA tool working principle is the following: basically a DRC run is performed in which the rules file (file used for connections definition and extraction) and the RSF file (Run Specific file, used to customize the specific DRC run) loaded

in the DRC run window are customized by the user for the extraction of the “GDSII file containing the sensor connections”. In fact the rules files and the RSF files depend on sensor pin out and must be produced by using an executable file called “gds_generator.csh”.

The procedure for the GDSII extraction is the following:

1. the user must prepare the layout for the net extraction (this means to create a new layout view in which pin name labels are added) and a file where the MEMS pins are listed;
2. the user must run the executable file “gds_generator.csh” in a working directory where he has previously put the three files “header_connection_highlight.txt” (used to generate the rules file), “RSF_header.txt”(used to generate the RSF file), and the file where the MEMS pins are listened (created at the previous step). The syntax is the following:

./gds_generator.csh argument1 argument2 argument3 argument4

- argument1 is the name of a file in which MEMS pin names are listened;
 - argument2 is the name of the rules file that will be generated;
 - argument3 is the name of the RSF file that will be generated;
 - argument4 is the name of output GDSII modified file that will be produced by the DRC run;
3. the user must open the MEMS layout and run a DRC process loading as RSF file and rules file the two files produced at the previous step (named argument2 and argument3);
 4. once the DRC run is finished the user will found the file called “argument4” in the run directory. This is the GDSII file which represents the connection in the sensor and that can be visualized with a layout viewer.

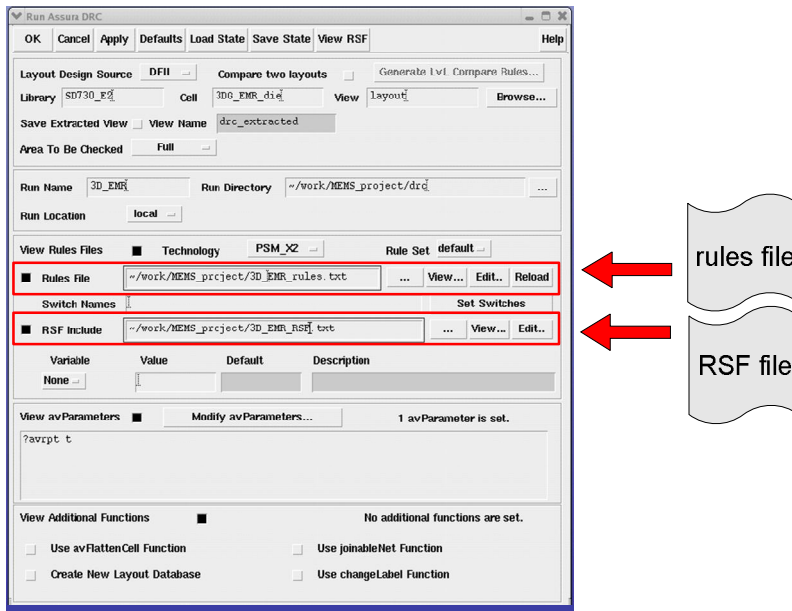


Fig. 31 ASSURA tool for connectivity extraction working principle

3.1.4. ASSURA tool for connectivity extraction: executable file

In the ASSURA tool for MEMS LVS the rules file used to perform LVS is the same for each MEMS sensor (once the process has been assigned) because the check performed by the tool does not depend on pin names. On the contrary in the ASSURA tool for connectivity extraction the tool must create a layer for every specific pin connection and it is important do not lost the correspondence between the layer created and the pin name.

Then a RSF for each sensor class must be created and in order to make the procedure as fast as possible, an executable file called “gds_generator.csh” has been created that starting from a file containing the pin name list creates the rules file and the RSF file necessary for the connectivity extraction.

The executable file “gds_generator.csh” can be divided in two sections: the first section generates the rules file while the second one generates the RSF file.

The rules file together with the RSF file is the core of the ASSURA tool for connectivity extraction. In fact the first one extracts the different pin connections and creates for each connection a new layer while the second one customizes the output file generation.

```
#!/bin/csh

set input_file = $1
set rules_file = $2
set RSF_file = $3
set gds_name = $4

#if $output_file = ""
#echo "help...."
#end

cat header_connection_highlight.txt > $rules_file

foreach pad ( `cat $input_file` )

    set pad1 = \"$pad\"
    echo "EP_$pad"CON = geomGetNet( EP_d "$pad1")" >> $rules_file
    echo "BP_$pad"CON = geomGetNet( BP_d "$pad1")" >> $rules_file
    echo "AL_$pad"CON = geomGetNet( AL_d "$pad1")" >> $rules_file
    echo $pad"_NET = geomOr(EP_"$pad"CON BP_"$pad"CON AL_"$pad"CON)" >> $rules_file

end

echo ")" >> $rules_file

cat RSF_header.txt > $RSF_file
set count = 0
set gds2 = \"gds2\"
set LibName = \"LIB_GDS.DB\"

echo "outFile("$gds2 $LibName' ""./"$gds_name'" >> $RSF_file

foreach pad ( `cat $input_file` )

    @ count = $count + 1
    echo "outLayer( \"$pad"_NET" $count" type( 0 ) )" >> $RSF_file
end

echo ")" >> $RSF_file
```

Fig. 32 Executable file for the generation of the rules file and the RSF file needed for ASSURA tool for connectivity extraction

3.1.5. ASSURA tool for connectivity extraction: rules file

The rules file is the file used for connection definition and extraction. It is generated from an executable file as seen in the previous section and it is organized as follows:

1. a first section in which there is the physical layer declaration;
2. a second section in which the connectivity inside the sensor is extracted;
3. a third section in which the new “connectivity” layers are defined (a layer for each pin connection is created).

```

HrcExtractRules(
  layerDefs( "df2"
    BP_d = layer( "BP" type( "drawing" ) )           ;;buried poly
    PL_d = layer( "PL" type( "drawing" ) )           ;;protection layer
    OX_d = layer( "OX" type( "drawing" ) )           ;;oxide
    EP_d = layer( "EP" type( "drawing" ) )           ;;epi poly
    AL_d = layer( "AL" type( "drawing" ) )           ;;aluminium for pads
    UO_d = layer( "UO" type( "drawing" ) )           ;;unknown
    AL_pin_text = textToPin( "AL" type( "pintext" ) ) ;;label definition
    BP_s = layer( "BP" type( "markerR" ) )           ;;layers to extract resistances
  )

  BULK1 = geomBkqnd()
  BULK = geomSize( BULK1 0.005 )
  ;; extraction of bulk connection
  UO_device = geomAnd( UO_d BULK )

  ;;definition of layer to extract resistances immediately after pad conection (except for SUB connection)
  EP_d_red = geomAndNot( BP_d BP_s )
  pad_connection = geomAnd( EP_d BP_s )

  ;;when OX is over the protection layer the contact between EP and BP is not active
  OX_red = geomAndNot( OX_d PL_d ) ;;OX_red is the region in which EP and BP are connected

  ;;definition of via between epi and buried poly
  EP_vias = geomAnd( EP_d_red OX_red )
  EP_BP_vias = geomAnd( EP_d BP_vias )           ;;region in which EPI and BP are overlapped and there is a via

  ;;creation of the layer connectivity
  geomConnect( label( AL_pin_text AL_d )
    buttOrOver( AL_d EP_d )
    via( UO_d BULK EP_d )
    via( EP_BP_vias BP_d EP_d )
  )
  EP_SUBCON = geomGetNet( EP_d "SUB" )
  BP_SUBCON = geomGetNet( BP_d "SUB" )
  AL_SUBCON = geomGetNet( AL_d "SUB" )
  SUB_NET = geomOr( EP_SUBCON BP_SUBCON AL_SUBCON )
  EP_MSLCON = geomGetNet( EP_d "MSL" )
  BP_MSLCON = geomGetNet( BP_d "MSL" )
  AL_MSLCON = geomGetNet( AL_d "MSL" )
  MSL_NET = geomOr( EP_MSLCON BP_MSLCON AL_MSLCON )
  EP_DRLLCON = geomGetNet( EP_d "DRL" )
  BP_DRLLCON = geomGetNet( BP_d "DRL" )
  AL_DRLLCON = geomGetNet( AL_d "DRL" )
  DRL_NET = geomOr( EP_DRLLCON BP_DRLLCON AL_DRLLCON )
  EP_PSL1CON = geomGetNet( EP_d "PSL1" )
  BP_PSL1CON = geomGetNet( BP_d "PSL1" )
  AL_PSL1CON = geomGetNet( AL_d "PSL1" )
  PSL1_NET = geomOr( EP_PSL1CON BP_PSL1CON AL_PSL1CON )
  EP_PSL2CON = geomGetNet( EP_d "PSL2" )
  
```

physical layers declaration

connectivity extraction

new connectivity layers definition

Fig. 33 Example of rules file for the connectivity extraction and the definition of new layers which represent the different sensor connections

The rules file of Fig. 33 is the file that must be loaded in the DRC window in order to have the generation of the “GDSII connectivity file” in which each layer represents a sensor connection.

3.1.6. ASSURA tool for connectivity extraction: RSF file

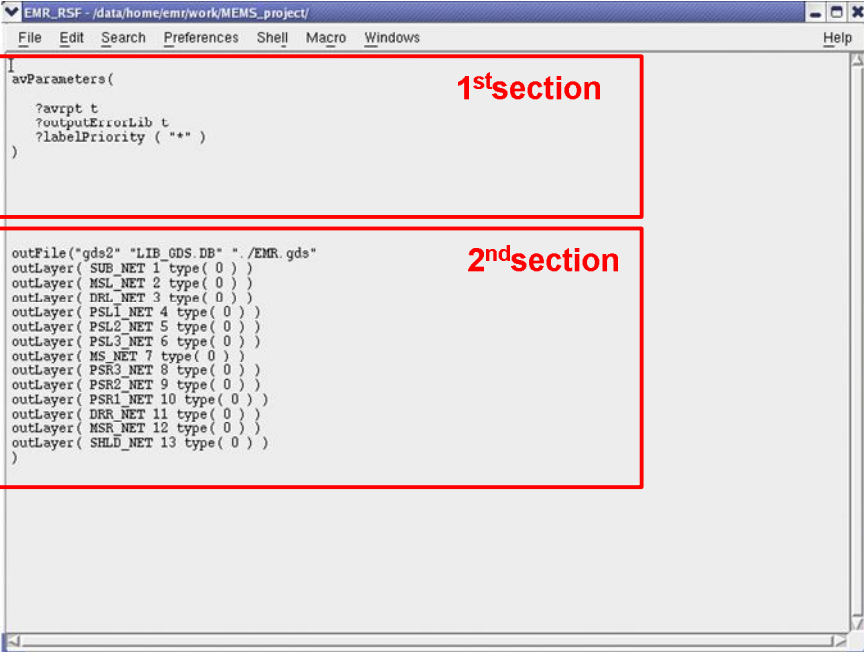
The RSF file customizes the DRC run in order to obtain the desired output.

In the picture below an example of RSF file is shown.

In the first section of the RSF file the “avParameters” command set the parameters associated with the current DRC run. More in detail:

- “?avrpt” parameter allows the user to control the number of error messages reported per cell. Setting this parameter to true (t) the errors are reported at the end of the error list (this is the default setting).
- “?outputErrorLib” enables or disables the “outFile” command that outputs layers to a GDSII file. If “outputErrorLib” is set to true (t) the “outFile” command is executed.
- “?labelPriority” defines label priority to resolve conflicts between multiples label on a net during connectivity extraction. “?labelPriority” overrides the default label priority conflict. The syntax “?labelPriority(“ * ”)” means that each conflict is resolved alphanumerically. This command is needed because in some MEMS designs two nets with different labels are connected together (for example the right and the left substrate connection). The command forces the tool to ignore the conflict and to extract the net. Without this command the two nets which are involved in the conflict are not extracted.

The second section of the RSF file creates a GDSII output stream file in the specified location (in this case the file is created in the current directory). Layers that must be output are specified in the “outLayer” field (as shown in Fig. 34). In this case the layers that are output are the new connectivity layers defined in the rules file.



```

EMR_RSF - /data/home/emr/work/MEMS_project/
File Edit Search Preferences Shell Macro Windows Help

1
avParameters(
    ?avrpt t
    ?outputErrorLib t
    ?labelPriority ( ** )
)

outFile("gds2" "LIB_GDS.DB" ". /EMR.gds"
outLayer( SUB_NET 1 type( 0 ) )
outLayer( MSL_NET 2 type( 0 ) )
outLayer( DRL_NET 3 type( 0 ) )
outLayer( PSL1_NET 4 type( 0 ) )
outLayer( PSL2_NET 5 type( 0 ) )
outLayer( PSL3_NET 6 type( 0 ) )
outLayer( MS NET 7 type( 0 ) )
outLayer( PSR3 NET 8 type( 0 ) )
outLayer( PSR2 NET 9 type( 0 ) )
outLayer( PSR1 NET 10 type( 0 ) )
outLayer( DRR_NET 11 type( 0 ) )
outLayer( MSR_NET 12 type( 0 ) )
outLayer( SHLD_NET 13 type( 0 ) )
)

```

Fig. 34 Example of RSF file.

3.2. Methodology for post layout ANSYS simulation

As mentioned in the chapter introduction a crucial step in MEMS design flow is the elaboration of a FEM model as close as possible to the real device. In fact simulations on the FEM micro sensor model are fundamental for a correct design and sizing of the MEMS device.

For this purpose a *post layout simulation methodology* has been developed. Post layout simulations are FEM simulations performed on the real sensor layout extracted from layout environment. Information is extracted from a GDSII file which represents the real sensor and then used in a FEM environment to build a model.

Elaborating a methodology for post layout simulations is not trivial and the main issues are often two:

- the complexity of the sensor structure that must be simulated;
- the compatibility problem between the FEM simulation environment and MEMS layout environment.

These issues, especially the second one, make post layout simulations not really diffused although they are very useful.

The methodology for post layout simulations proposed in the following overcomes the aforementioned issues and shows the possibility to have a linear, quick and reliable flow for performing post layout simulations.

The compatibility problem has been overcome by adopting an intermediate tool which converts the file format typical of MEMS layout (*GDSII*) in a file format compatible with FEM tool (file extension *.anf*), while the complexity problem has been overcome by the following approach. Most of the MEMS sensors has a symmetric structure, so instead of exporting the whole MEMS layout only a part of the geometry (an half geometry or a quarter geometry for example) is exported and subsequently imported in simulation environment where is simulated by applying particular symmetrical condition on the model boundaries.

Let's see how the proposed methodology can be applied to a real z-gyroscope fabricated at Fraunhofer Institute for Silicon Technology (Itzehoe, Germany) (Fig. 35).

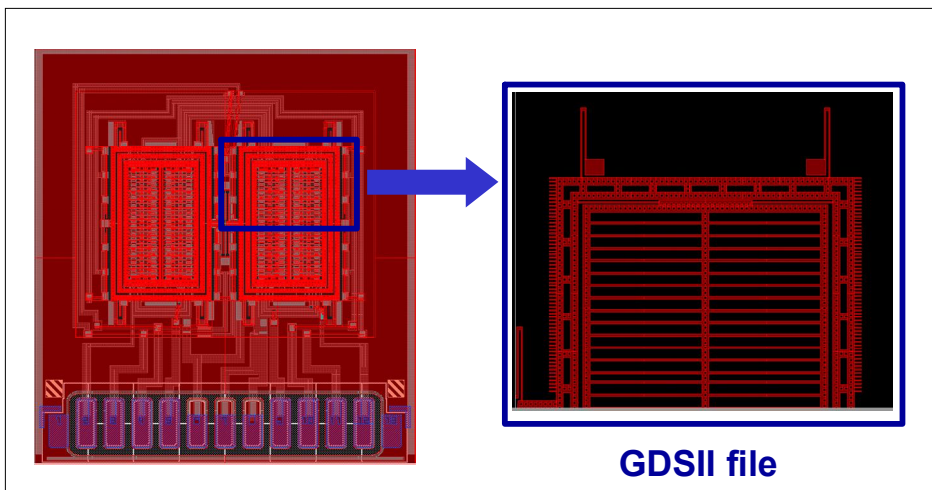


Fig. 35 Layout of a LATMAX z-gyroscope and export of a quarter of the geometry

The first step is the extraction of the GDSII file which represents the sensor layout. The z-gyroscope chosen as example has a symmetric structure, then in order to reduce the complexity of the model only a quarter of the geometry is exported. The second step is the conversion of the GDSII file in a format compatible with the FEM tool chosen for post layout simulations (in our case ANSYS™). The GDSII file is imported in an appropriate conversion tool (LinkCad™) and is converted from GDSII to a “.anf file”. In the conversion step there is a key point that must be taken into account. It's no convenient to convert the whole GDSII file in a single .anf file , but the GDSII file must be converted in several .anf file, one for each sensor structure. In our example four .anf files are generated: one for sensor springs, one for driving mass, one for sensor frame and one for sensor anchors.

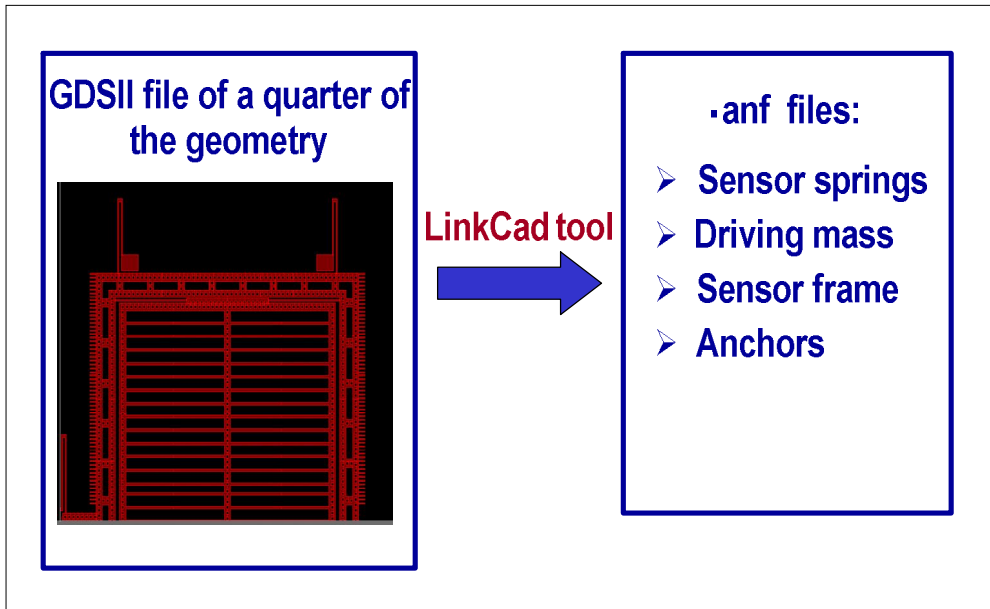


Fig. 36 Conversion of the GDSII file which represents the sensor in several .anf files which represent the different sensor structures

In this way the import and subsequent simulation in ANSYS environment becomes simpler. In fact for each sensor structure we have a single .anf file which can be imported individually and individually treated before simulation.

Once the conversion step has been performed the “.anf files” are imported in ANSYS environment to build the model of a quarter sensor geometry.

At this point the model can be simulated by applying appropriate symmetry boundary conditions. Symmetry boundary conditions are necessary to emulate the behaviour of the whole geometry.

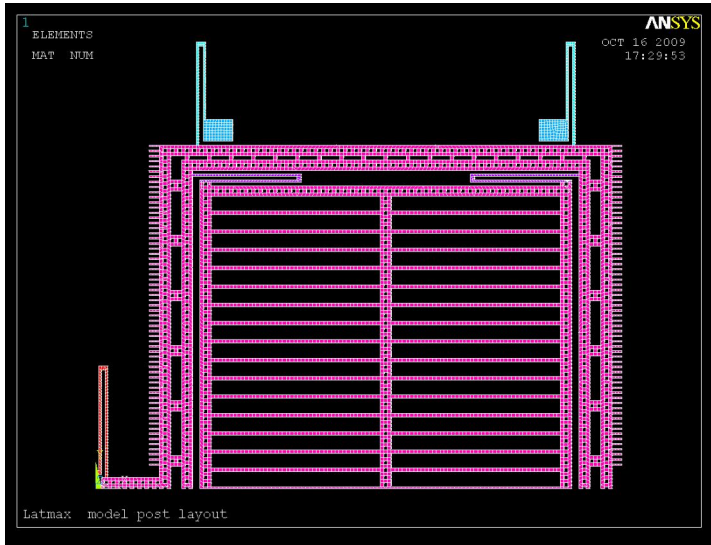


Fig. 37 ANSYS model of a quarter sensor geometry

In order to evaluate the reliability of the developed methodology, the results of post layout simulations can be compared with the measurements performed on a real gyro prototype. Tab. 2 shows the comparison between post layout modal simulations and measurement performed on a LATMAX z-gyroscope in the laboratories of Sensordynamics AG. The percentage error is always lower than 1.2% thus demonstrating a very good reliability of the methodology adopted for post layout simulations.

LATMAX motion	Modal simulation	Measurement	Difference %
Primary motion (Hz)	18335	18500	+0.9%
Secondary motion (Hz)	19224	19000	-1.16%
First parasitic mode (Hz)	20281	20200	-0.4%

Tab. 2 Comparison between modal post layout simulation results and measurement results performed on a LATMAX z-gyroscope

3.3. ASSURA tool for parasitic capacitances extraction

Another important aspect in the design of MEMS devices is the impact of secondary effect such as parasitic capacitances. These parasitic capacitances can be properly estimated only after the layout phase because they depend on physical characteristics of the sensor (e.g. physical interconnections).

Parasitic capacitances can heavily affect the MEMS behaviour and uncertainty on their value can lead to a wrong design of the electronic for MEMS conditioning and reading out.

In order to have a reliable and quick method to calculate parasitic capacitances an ASSURA tool has been developed which starting from the MEMS layout extracts the parasitic capacitance values.

The tool working principle can be better explained by referring a real gyroscope, then let's consider the LATMAX z-gyroscope already mentioned in the previous sections (Tab. 3 shows the pin out of the gyro under study).

PIN number	PIN name	Description
1	SUB	Substrate connection
2	FBL	Feedback Left
3	MSL	Motor sense left
4	DRL	Driving left
5	PL	Plate sense left
6	SHL	Shield left
7	MS	Moving structure
8	SHR	Shield right
9	PR	Plate sense right
10	DRR	Driving right
11	MSR	Motor sense right
12	FBR	Feedback right

Tab. 3 Pin out of a z-gyroscope LATMAX

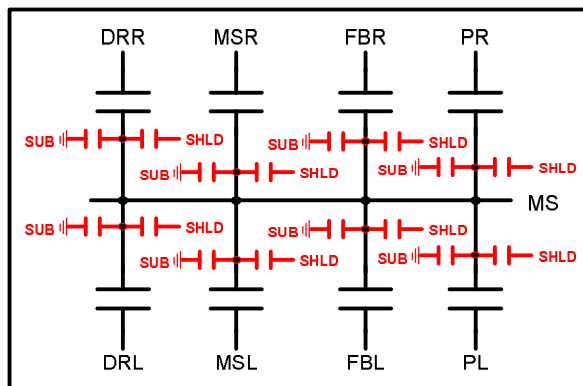


Fig. 38 Equivalent electric circuit for the z-gyroscope under study. The parasitic capacitances are reported in red

The equivalent electric circuit for the gyroscope under study is made up of the ideal symmetric functional capacitances (driving and sensing capacitances needed for the gyro working) and the parasitic capacitances as shown in Fig. 38.

The main parasitic capacitances are the capacitances between each pin connection and the substrate and the capacitances between each pin connection and the shield connection, consequently the tool has been developed to extract these parasitic capacitances.

Each parasitic capacitance is due to two capacitive contributes, a vertical capacitance (due to the overlap between different connections) and a lateral capacitance (due to the lateral distance between two different connections).

Up to now the tool allows the extraction of vertical parasitic capacitances only (which have the higher impact on the sensor), but in future will be extended to lateral parasitic capacitances too. This means that the ASSURA tool extracts the parasitic capacitances due to the overlap of each pin connection and the shield connection and the parasitic capacitances due to the overlap of each pin connection and the substrate.

3.3.1. Shield parasitic capacitances

The strategy followed to calculate the parasitic capacitances between each pin and the shield connection is the following: for each pin the vertical parasitic capacitance is due to the overlap area between the pin connection and the shield connection; then knowing this overlap area the capacitance can be calculated by using the well known expression:

$$C_{pin_shield} = \epsilon_0 \frac{A}{d_0} \quad (1)$$

where A is the overlap area (expressed in μm^2), $\epsilon_0=8.854\text{e-}18$ [F/ μm] is the vacuum permittivity, and d_0 is the distance between the pin connection and the shield ($d_0=1.6 \mu\text{m}$, is the distance between epi poly layer and buried poly, indeed with reference to the process description of section 2.4 we can have an overlap between different connections only in the case of the epi poly path of one connection is over the buried poly path of another connection, otherwise we would have a shortcut).

Again, as for the tools described in section 3.1, the ASSURA tool for calculating the parasitic capacitances has been developed in Cadence™ environment by using the same tool already existing to perform the DRC of an electronic circuit and customizing this tool with an appropriate rules file and RSF file.

In particular the rules file defines for each pin connection a new layer which represents the overlap area, while the RSF file generates a GDSII file (e.g. "LATMAX_areaSHLD.gds") in which these layer are output.

Finally a skill procedure uses the produced GDSII file to calculate the area of each layer and then the capacitance by applying equation (1)

3.3.2. Substrate parasitic capacitances

Again the parasitic capacitances between each pin and the substrate are due to the overlap area between the pin connection and the substrate. In this case we have to take into account that the substrate is the lowest layer spanning all sensor area and that each pin connection is made of epi poly and buried poly connected through "vias", so in this case each parasitic capacitance is due to two contributes:

the first due to the overlap between the epi poly part of the connection and the substrate and the second due to the overlap between the buried poly part of the connection and the substrate.

Then in this case the rules file defines for each pin two new layers: the first layer represents the overlap area between the epi poly part of the pin connection and the substrate; the second layer represents the overlap area between the buried poly part of the pin connection and the substrate.

Moreover for each connection we have to take into account the PAD capacitance, so the rules file defines also another layer which represents the overlap area between the pad region and the substrate.

Again these layers are output in a GDSII file (e.g. "LATMAX_areaSUB.gds") and the skill procedure for the parasitic capacitance extraction calculates the area of each layer and calculates the capacitance value by applying equation (2).

$$C_{pin_SUB} = \epsilon_0 \frac{A_{EPI}}{d_{EPI}} + \epsilon_0 \epsilon_r \frac{A_{BP}}{d_{BP}} + C_{pad} \quad (2)$$

Where A_{EPI} is the overlap area between the epi poly part of the pin connection and the substrate, $d_{EPI}=(1.6+2.45)=4.05\mu\text{m}$ (distance between epi poly layer and substrate), A_{BP} is the overlap area between buried poly of the pin connection and substrate, $d_{BP}=2.45\mu\text{m}$ (thickness of the oxide between the buried poly and the substrate), ϵ_r is the relative permittivity of the oxide under the buried poly and C_{pad} is the pad capacitance.

3.3.3. Tool working principle

The ASSURA tool working principle is the following: starting from the sensor layout two DRC runs are performed. Each DRC run is performed by using the same rules file (the file "cap_extraction_rules.txt" which defines layers for substrate capacitance and shield capacitance calculation), but different RSF files (the RSF file is used to configure the DRC run and its output). Each DRC run generates a GDSII file which will be used for the calculation of the capacitance values. More in detail two GDSII files are generated:

- a GDSII file containing the information needed to calculate the parasitic capacitances between each pin and the substrate (e.g. "LATMAX_areaSUB.gds" mentioned in section 3.3.2);
- a GDSII file containing the information needed to calculate the parasitic capacitances between each pin and the shield (e.g. "LATMAX_areaSHLD.gds" mentioned in 3.3.1);

Once the GDSII files have been created they must be imported in a proper library so creating two different cells, one for each class of capacitances (parasitic capacitances versus substrate and parasitic capacitances versus shield). At this point the user must load and run a skill procedure which calculates the capacitance values by using these cells. Basically the skill file selects all layers of an open layout cell view and for each layer performs the operation needed for the capacitance calculation.

CHAPTER 4

MEMS SYSTEMS: CASE STUDIES

As seen in Chapter 2 modelling is a key step in a MEMS design flow, and having a MEMS model as close as possible to the real device is fundamental also in the study and design of MEMS reading out and conditioning systems.

The modelling in MEMS design flow is the topic addressed in this chapter using two case studies which belong to two leading MEMS applications: optical MEMS (MOEMS) and MEMS for automotive applications.

Indeed section 4.1 describes the development of the model of a torsional micromirror for laser projection systems while section 4.2 shows the study of a new system developed for shock immunity enhancement in gyroscopes for automotive applications.

The micromirror modelling of section 4.1 is presented in an exhaustive and complete way. Starting from the FEM simulations needed to extract the characteristic device parameters and finishing with the description of the Simulink™ model developed and the integration of the model itself in a larger system aiming at design/tuning the read out electronic.

The control loop for shock immunity enhancement presented in section 4.2 is an innovative and effective method to improve the performance of a micro mechanical gyroscope. The design of control loop starts from the theoretical study of its working principle, continues with the development of the Simulink™ model of the adopted control solution and finishes with the verification based on simulation results.

4.1. Micromirror for laser projection system

Continuous progress in MicroElectroMechanical System (MEMS) technology has led to the development of MicroOptoElectroMechanical System (MOEMS) which can be used in a wide variety of applications such as: telecommunication systems, projection displays and barcode scanners.

Micro mechanical scanning mirrors are one of the key microstructure in MOEMS and are wide diffused in laser projection systems where they are used as scanners to deflect a laser beam modulated in according to a video signal.

The first scanning micromirror was proposed by K.E. Petersen in 1980 [26]. In his work Petersen presents an electrostatically actuated torsional scanning mirror, which is made of single-crystal silicon and is characterized by a deflection angle of about 0.02 degrees.

Since the first work of Petersen many other mirror designs that are characterized by different driving principles have been proposed. In literature we can find several examples of magnetic, thermal or piezoelectric mirror actuation, nevertheless electrostatic actuation is the widest diffused because it presents several advantages with respect to others actuation principles as detailed in the following.

A magnetically actuated mirror is deflected by exploiting the Lorentz Force: a winding coil is fabricated around the mirror plate and this coil interacts with an in-plane magnetic field [27]. The principal drawbacks of this approach are the generation of the magnetic field and the heating of the micromirror structure due to the current that flows in the coil.

Thermal actuation is achieved by using layers with different thermal coefficients. These layers are heated with a current and their deformation produces a bending of the mirror. In these actuators the problem is the significant influence of the ambient temperature.

In a piezoelectric actuated mirror, the mirror plate is backed up an array of piezoelectric unimorph microactuators [28]. An applied electric field produces the deformation of the piezoelectric actuators and these provide the mirror to be deflected of several tens degrees. As drawback the fabrication process of a piezoelectric actuated micromirror is rather complicated.

On the other hand, electrostatic actuators can be easily fabricated using micromachining techniques compatible with standard IC technology and they produce a highly efficient electrostatic force in microscale dimensions, offering the chance of using driving voltages that can be provided by standard Integrated Circuits.

Electrostatically actuated micromirrors require a solid characterization and modelling from both a mechanical and an electrical point of view. In next sections the study of a torsional micromirror fabricated at the Fraunhofer ISIT Institute for Silicon Technology [29] is presented.

The study is organized as follows: FEM simulations are used to extract the electrical and mechanical characteristic parameters of the device (section 4.1.2), then a complete Simulink™ model that describes the device from both a mechanical and an electrical point of view is developed (section 4.1.3) and the comparison between simulation results and measurement results is presented, and finally the integration of the model in a higher system model to design the micromirror read out stage is presented (section 4.1.4).

4.1.1. Micromirror working principle

The electrostatically driven scanner micromirror under study is fabricated in a novel fabrication technology that is bridging the gap between bulk and surface micromachining. It is based on state-of-the-art MEMS technologies using thick epi poly silicon layers and high rate anisotropic dry etch processes (DRIE) [30].

The micromirror is made up by a 60 μm thick circular polysilicon mirror plate which is covered by a gold layer (to enhance the reflectivity) and is connected to a gimbal frame by a pair of polysilicon torsion springs, as shown in Fig. 39. Also the gimbal frame is supported by a pairs of polysilicon springs which connect the frame to the substrate.

The structure is a dual axis micromirror: the slow axis works at the resonance frequency of 300 Hz while the fast axis works at the resonance frequency of 30 KHz. The fast axis allows the micromirror to be tilted around y direction while the slow axis allows the micromirror to be tilted around x direction.

Both the two axis are actuated by electrostatic vertical comb drives. Vertical comb drives provide a motion in and out of the plane and present several advantages if compared to lateral comb drives [31], then they achieve larger scan angle at high resonance frequencies [32] and finally they directly apply the torque to the mirror without needing any hinges to couple their linear motion into torsional mirror motion.

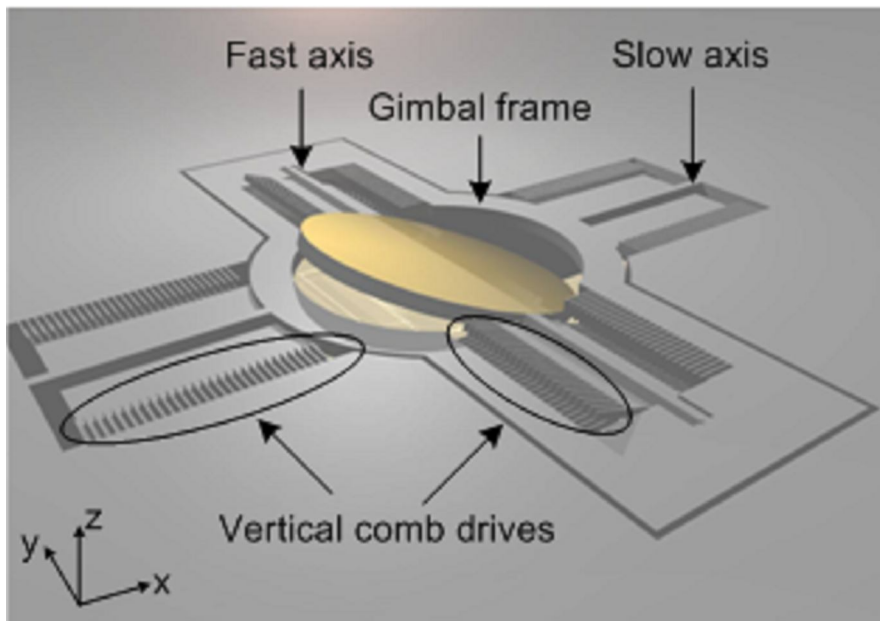


Fig. 39 Micromirror working principle

Each vertical comb drive consists of a set of moving mechanical polysilicon electrodes and a set of rigid electrodes suspended over an etched pit. The rigid electrodes are bound to the substrate, while the movable electrodes are linked to the axis.

When a voltage is applied between the fixed fingers and the movable ones, an electrostatic torque arises between the two electrodes. Consequently the movable fingers rotate around the torsional axis until the Electrostatic Torque (T_e) and the Mechanical restoring Torque (T_m) of the springs are equal. These two torques can be expressed by (3) and (4).

$$T_e = \frac{1}{2} N_f V^2 \frac{dC}{d\theta} \quad (3)$$

$$T_m = K \theta \quad (4)$$

where N_f is the total number of fingers of the axis comb drive, V is the applied voltage, C is the capacitance between a single fixed finger and a movable finger, K is the torsional stiffness of the springs and θ is the rotational angle.

Combining (3) and (4) the equation that describes the micromirror motion at equilibrium is obtained (5).

$$\frac{1}{2} N_f V^2 \frac{dC}{d\theta} = K \cdot \theta \quad (5)$$

From (5) is evident that the characteristic micromirror parameters, needed to have a complete device description, are: the torsional stiffness, the curve capacitance versus rotation angle and the resonance frequency of each axis. These parameters have been extracted by performing electrostatic and mechanical simulations with a Finite Element Method tool (Comsol MultiphysicsTM), as shown in the following section.

4.1.2. FEM simulations

Electrostatic Simulations

As said in the previous section the micromirror is actuated by means of vertical comb drives whose electrostatic analysis is described in the following.

In contrast with the analysis of parallel plate actuators, the analysis of vertical comb drive actuators is more complicated due to the presence of strong fringe fields. Consequently, the relationship between the capacitance and the rotation angle is extracted performing electrostatic simulations with a FEM tool.

Instead of performing the electrostatic simulations of the whole micromirror structure, a simplified model is adopted in order to reduce the computational load of the simulator without losing in generality and accuracy. This simplified structure is a single functional comb drive unit made of a single movable finger between two fixed fingers, as shown in Fig. 40.

Typically, in applications that use vertical comb drive actuators, the voltages applied are in the range of tens Volts (when the micromirror is in the vacuum), thus in our electrostatic simulations the voltage applied is 30V.

More in detail each fixed comb finger is made up of two epi poly silicon layers (each 30 μ m thick) isolated by an intermediate oxide, the upper layer is biased at 30V while the lower layer is biased at 0V. On the contrary each movable finger is made up of only one 30 μ m thick layer biased at 0V.

This biasing configuration and the staggered position of the movable fingers allow an electrostatic torque to be generated which causes the micromirror axis motion.

The capacitance versus angle relationship is extracted by using the results of electrostatic simulations.

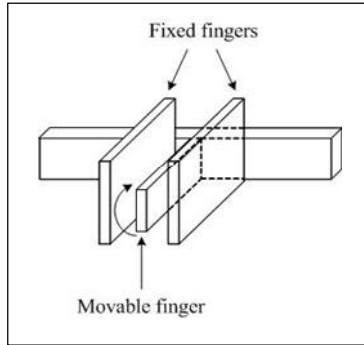


Fig. 40 Simplified model used in electrostatic simulations

Indeed the FEM simulator calculates the electric field distribution and the electrostatic energy (W_{es}) stored between the fixed and the movable fingers from which the capacitance value can be extracted (6).

$$C = \frac{2W_{es}}{V^2} \quad (6)$$

To obtain the capacitance versus angle relationship, different capacitance values for different rotational angle must be extracted. In order to automate this procedure a Matlab routine has been developed that elaborates simulation results and automatically extracts the capacitance values. This routine performs a rotation of 20 degrees of the movable finger (from -10° to $+10^\circ$) with steps of 1 degree, calculates the capacitance value for each step and writes the results in an output file.

Since Comsol Multiphysics™ is Matlab™ compliant, the routine can be directly imported in Comsol™ environment and the capacitance versus angle characteristic for each axis can be extracted in an automatic way (Fig. 41).

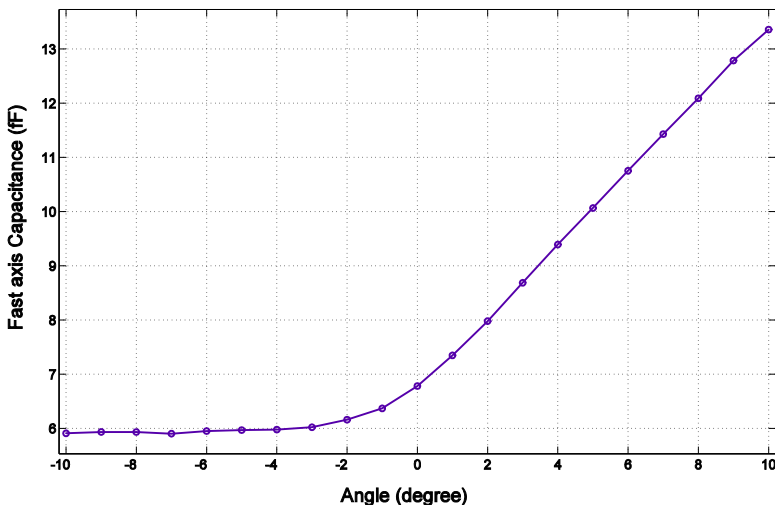


Fig. 41 Capacitance versus angle curve for the micromirror fast axis

The relationship between the capacitance and the rotation angle (θ) is extracted by fitting the curve of Fig. 41 in Matlab™ environment, and is fundamental for the development of the Simulink™ micromirror model as shown in section 4.1.3. The relationship between capacitance and angle is a sixth order polynomial expression as shown in (7).

$$C(\vartheta) = p_1 \cdot \vartheta^6 + p_2 \cdot \vartheta^5 + p_3 \cdot \vartheta^4 + p_4 \cdot \vartheta^3 + p_5 \cdot \vartheta^2 + p_6 \cdot \vartheta + p_7 \quad (7)$$

where C is the capacitance expressed in femto-Farad, θ in the rotation angle expressed in degrees, and p_i are the coefficients reported in Tab. 4 and expressed in (femto-Farad/degree).

p_1	p_2	p_3	p_4	p_5	p_6	p_7
2.3×10^{-6}	7.4×10^{-6}	-5.4×10^{-4}	-1.5×10^{-3}	5.9×10^{-2}	0.45	6.83

Tab. 4 Coefficients for the capacitance versus rotation angle relationship

An identical procedure has been followed to calculate the capacitance versus angle characteristic for the micromirror slow axis.

Mechanical Simulations for the resonance frequency extraction

A key issue, in order to perform a correct driving of the micromirror, is the study of the resonance frequencies of the structure.

In fact each micromirror axis must be driven at the resonance frequency because in this condition each axis reaches the maximum rotation angle for a given driving voltage amplitude.

The eigenfrequency analysis is performed by means of a mechanical simulation in which no loads are applied to the structure and the fixed boundaries are set with appropriate constrains.

In order to improve the convergence of the simulator some tricks are adopted. One of the main problems of FEM simulations is the mesh complexity of the structure, thus in order to reduce it the micromirror mesh has been performed with a 2-D model first and then the obtained planar mesh has been extruded to simulate the 3-D structure. Furthermore the micromirror has been simulated without considering the fixed fingers of each comb drive because they have no relevance in the calculation of the resonance frequency.

As results of the eigenfrequency analysis, the six lowest resonance frequencies and their corresponding shape modes have been obtained. The value of the resonance frequencies are reported in Tab. 5

f_1 (Hz)	f_2 (Hz)	f_3 (Hz)	f_4 (Hz)	f_5 (Hz)	f_6 (Hz)
10938^{-6}	18597	29945	36889	55249	65730

Tab. 5 Six lowest resonance frequencies for the micromirror fast axis

The resonance frequency f_3 (Tab. 5) is related to a torsional motion of the micromirror fast axis in and out the xy plane, as shown in Fig. 42. Experimental

results, concerning a real torsional micromirror sample fabricated at the Fraunhofer ISIT Institute, confirm the aforementioned value. Again an identical procedure has been followed to calculate the slow axis resonance frequency

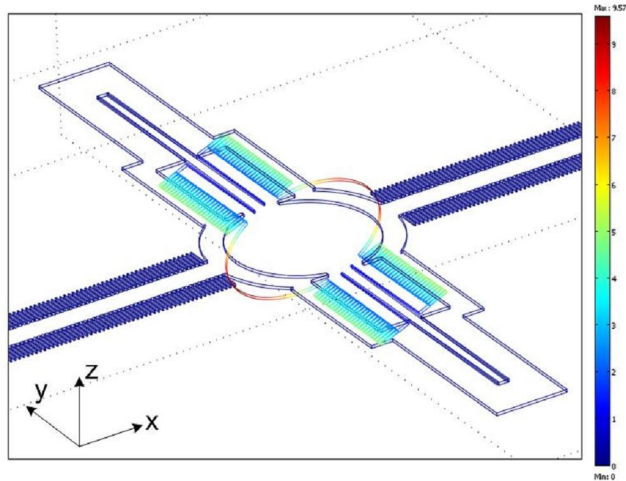


Fig. 42 Fast axis motion at its the resonance frequency

Mechanical Simulations for the torsional stiffness extraction

The torsional constant of each micromirror axis can be calculated performing mechanical simulations. For simplicity in this section we only show how to calculate the torsional constant of the micromirror fast axis, the procedure is similar for the slow axis.

The strategy adopted is the following: two opposite forces ($\pm F_z$) have been applied at the two opposite sides of the mirror plate in the direction of the z-axis, as shown in Fig. 43.

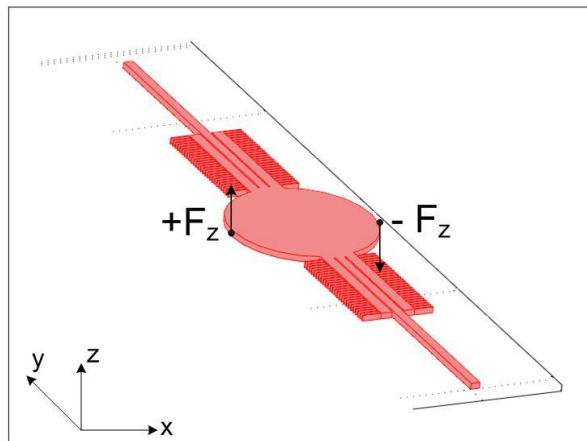


Fig. 43 Model for the calculation of the fast axis stiffness: two opposite force F_z are applied to the micromirror plate

The forces applied produce a torsion motion from which the torsional stiffness can be extract. In fact by performing a parametric simulation (in which F_z is the variable parameter), different values of the z-displacement (z_{displ}) are extracted for different values of the applied force. The data extracted are used to find the relationship between F_z and the z-displacement, and consequently the relationship between mechanical torque (T_m) and rotation angle (θ), as shown in (8) and (9).

$$T_m = r \times F_z \quad (8)$$

$$\theta = \sin^{-1}\left(\frac{z_{displ}}{r}\right) \quad (9)$$

where r is the micromirror plate radius

By sweeping the force module between 0 and 12mN, the curve torque versus angle of Fig. 44 is obtained. Fitting this curve in Matlab™ environment the relationship between torsional torque and angle is extracted (10).

$$T_m(\theta) = K_{nonlin} \cdot \theta^3 + K_{lin} \cdot \theta + T_0 \quad (10)$$

where $K_{nonlin}=7.458e-9$ [$N \cdot m / rad^3$], $K_{lin}=1.358e-5$ [$N \cdot m / rad$] and $T_0=-9.903e-14$ [$N \cdot m$]. From the comparison between the magnitude of the K values and the constant term T_0 we can gather that T_0 can be neglected without loosing in accuracy.

Even if (10) shows that the fast axis has a non linear behaviour due to the cubic term, the graph of Fig. 44 shows that the effect of the cubic term is not appreciable and consequently can be neglected in the micromirror model.

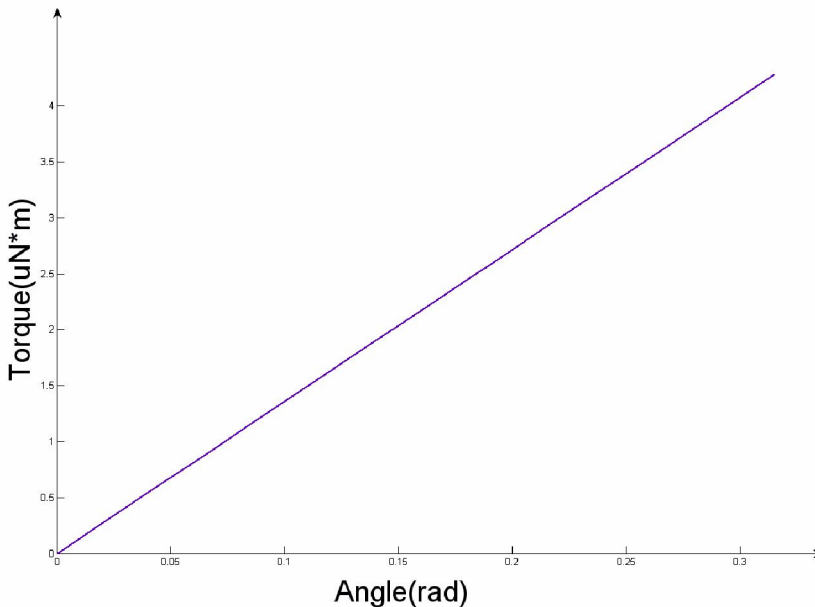


Fig. 44 Mechanical Torque versus rotation angle .for the micromirror fast axis

4.1.3. Simulink™ model

The characteristic micromirror parameters extracted as shown in previous sections are used to build up a Simulink™ model of each micromirror axis (Fig. 45) which has been successfully verified via experimental measurements and has proved its effectiveness in the development of the relevant electronic conditioning circuitry.

In this section only the model of the fast axis is shown, the model of the slow axis has been developed by following a similar procedure.

The model represents the micromirror behaviour from both a mechanical and an electrostatic point of view.

The micromirror fast axis is driven by applying two opposite voltages (11) and (12) to the fixed fingers respectively of the right and the left comb drives which control the axis motion (the movable fingers are kept to a constant voltage value which is the polarization of the moving structure (V_{MS})).

$$V_{drive_right} = V_{BIAS} + V_A \sin(2\pi f_R t) \quad (11)$$

$$V_{drive_left} = V_{BIAS} - V_A \sin(2\pi f_R t) \quad (12)$$

where V_{BIAS} is the DC polarization voltage, V_A is the amplitude of the sinusoidal actuation voltage signals and f_R is the resonance frequency of the axis.

The torque momentum which causes the micromirror fast axis rotation is the difference of the two electrostatic torques that arise from the application of voltage V_{drive_right} and V_{drive_left} as shown in (13).

$$T_e = \frac{1}{2} \left(\frac{dC_{dr}}{d\theta} (V_{drive_right} - V_{MS})^2 - \frac{dC_{dl}}{d\theta} (V_{drive_left} - V_{MS})^2 \right) \quad (13)$$

where C_{dr} and C_{dl} are respectively the capacitances that correspond to the right driving capacitance and to the left driving capacitance of the fast axis, and V_{MS} is the moving structure polarization voltage.

T_e is the electrostatic torque which drives the axis at its resonance frequency and the axis responds with a rotational motion which depends on its mechanical characteristics (such as the torsional stiffness (K) and the quality factor (Q)).

As said before the Simulink™ model of Fig. 45 describes the fast axis from both a mechanical and an electrostatic point of view and can be divided in four main blocks:

1. a first block implements the expression (13), it receives as input the two driving voltages and produces as output the electrostatic torque;
2. a second block implements the expression of the derivate of the capacitance (that is obtained by deriving the capacitance expression of (7));
3. a third block implements the transfer function of the micromirror fast axis (which is the transfer function of a resonant system);
4. a fourth block implements the expression of the capacitance.

The torque generated by implementing expression (13) is the input of the block that represents the transfer function of the micromirror axis thus describing the mechanical response of the axis itself. The output of this block is the rotation angle of the fast axis (Angle in Fig. 45) and it becomes the input of two blocks: the block that implements the derivative of the capacitance versus angle relationship and the block that implements the capacitance versus angle relationship. The first block is used to produce the derivative terms which appear in the torque expression while

the second one is used to extract the two capacitive sensing signals (C_{sr} and C_{sl} of Fig. 45) whose values are used in the read out electronic circuit.

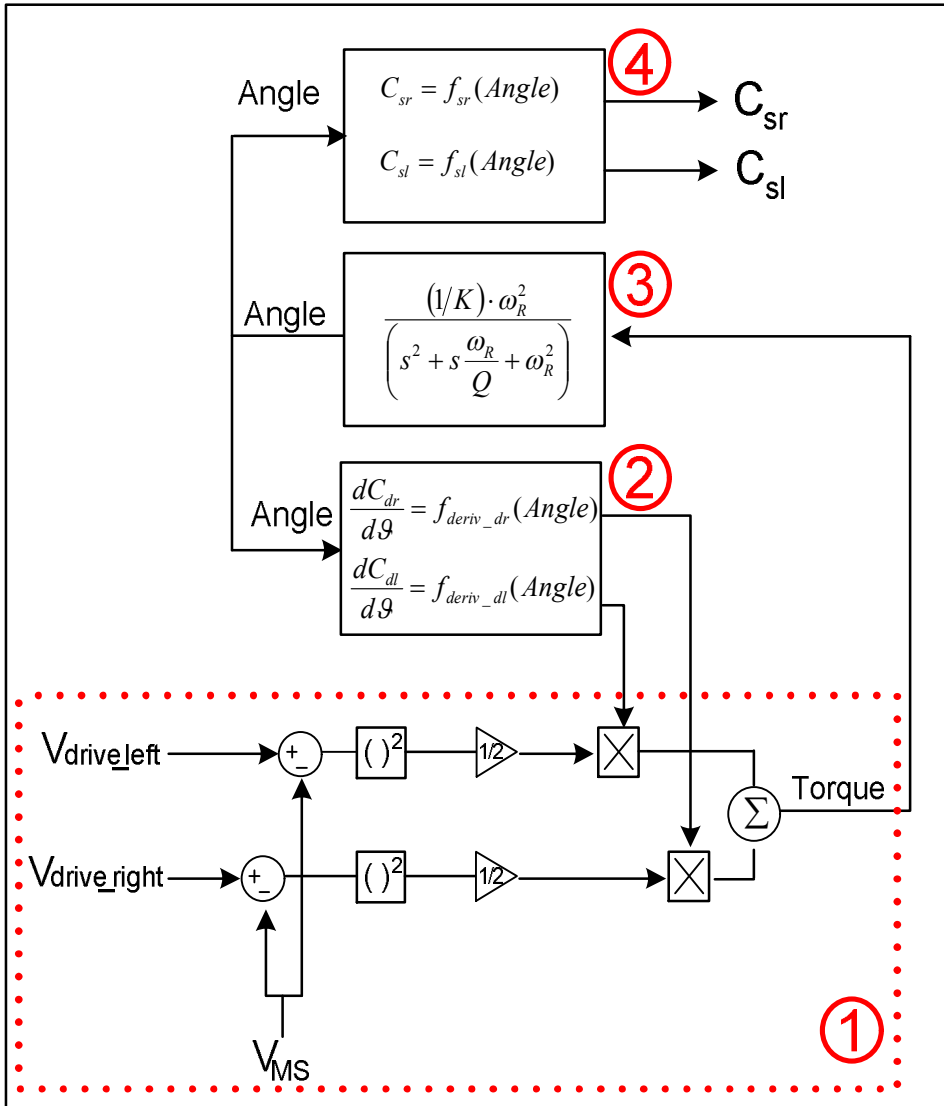


Fig. 45 Block diagram of the electro mechanical Simulink™ model for the micromirror fast axis. The block which generates the electrostatic torque starting from driving voltages together with the block which implements the derivate of the capacitance describes the electrostatic fast axis behaviour, while the block which implements the fast axis transfer function represents the axis mechanical behaviour.

Simulation results show a sinusoidal rotation angle with amplitude of 7.8 degrees as shown in Fig. 46. This result is in accordance with experimental measurements performed in Sensordynamics AG laboratories and shows the effectiveness of the developed model.

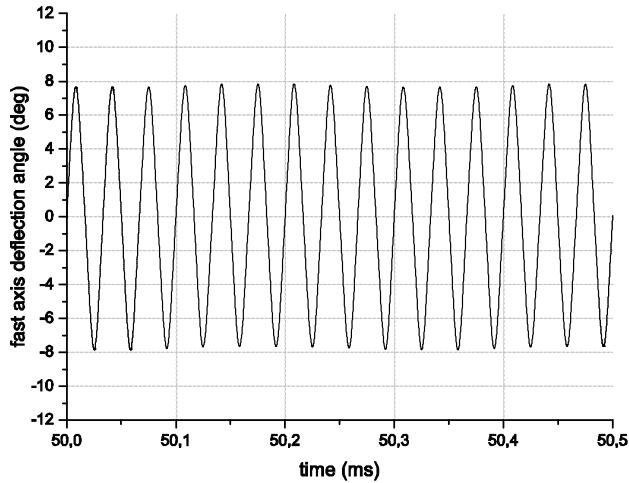


Fig. 46 Simulated angle versus time curve for the micromirror fast axis

Indeed the fast axis rotation angle has been measured [33] for a micromirror sample provided by Fraunhofer Institute for Silicon Technology (Itzehoe) and the measurement results confirm the rotation angle expected as shown in Fig. 47

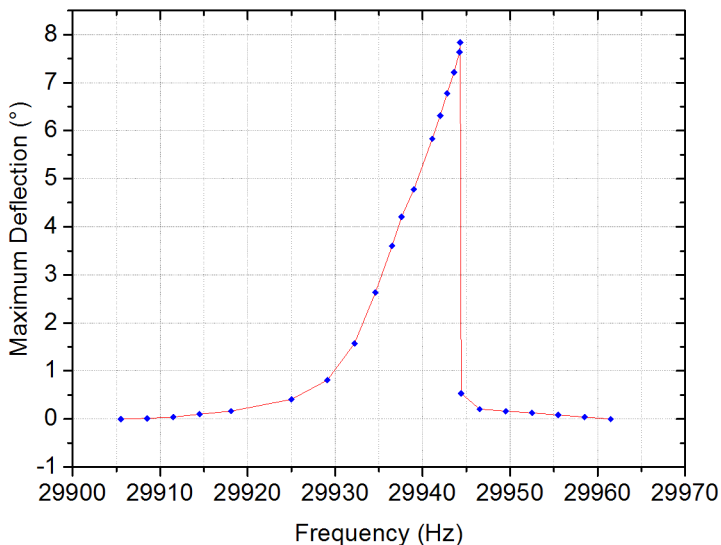


Fig. 47 Maximum deflection angle versus driving frequency extracted from the open loop measures on fast axis (from [33]).

The environment used to test the micromirror is based on a platform for sensor interface developing called Intelligent Sensor Interface (ISIF).

ISIF platform can be used as a complete solution for sensor signal conditioning as well as an actuation electronic driver for MEMS and MOEMS [34, 35]. The test environment has been customized thanks to the large programmability of the ISIF platform (input channels, signal conditioning blocks). All these customizations have been achieved using a simple graphical interface developed with LabView™.

The rotation angle has been measured by driving the micromirror fast axis with an open loop method and by using a laser source incident on the micromirror plate. From the deflection of the laser beam with trigonometric formulations is possible to extract the rotation angle of the plate. Of course the maximum rotation angle is in correspondence of the fast axis resonance frequency (29945Hz as extracted from FEM eigenfrequency simulations).

4.1.4. Model integration

The micromirror model described in the previous section has been used to perform the system study of the SD4K platform [36].

The SD4K is a flexible platform aimed to interface to a great number of MEMS sensors, with a specified focus over MOEMS sensors. In particular one of the goals of this platform is the realization of a laser-based projection system by using a bi-dimensional scanning micromirror. In this system the micromirror is used as a scanner to deflect a laser beam modulated in accordance with a video signal.

The micromirror model has been fundamental for the modelling and sizing of the platform input channel. In fact the device model has been integrated in a Simulink™ model of the whole input channel thus allowing to perform a complete simulation of the channel behaviour.

More in detail the capacitive signals (check Csr and Csl of Fig. 45) at the output of the micromirror model provide information on the micromirror position (since the capacitive signals are related to the rotation angle). These signals are detected by means of a charge amplifier and are processed through the input channel of the platform (essentially made up of a differential amplifier, a low pass filter, a level shifter and finally an ADC converter).

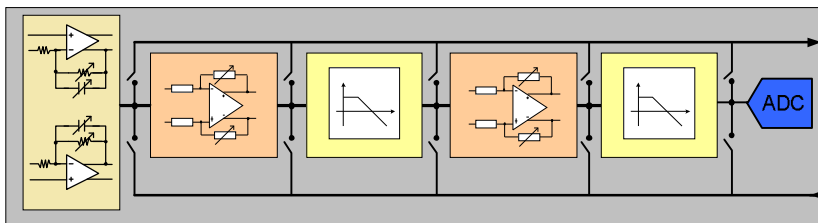


Fig. 48 Generic platform input channel

The Input Channel provide us with the information of the mirror position and this information is used in two way:

1. to realize a phase locking loop needed for a correct mirror driving;
2. to read from the memory the pixel information and drive the lasers accordingly to the mirror position

Thanks to the micromirror model the closed loop control can be simulated with high accuracy, where the capacitive signal from feedback electrodes of the mirror is

used trying to maintain the resonance frequency although it varies with temperature or external condition.

Moreover the memory reading can be simulated as well. In fact the capacitive signal from the electrodes is used to detect what pixel is actually covered and read from memory the relative colour information. This can be done only when the system is locked because in this way the phase error of the sensing will be constant.

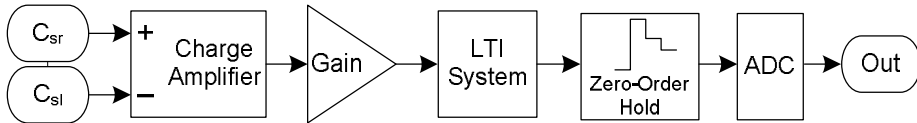


Fig. 49 . Input channel model: Csl and Csr are the sensing capacitance at the output of the mirror model. The channel has been modeled as a Linear Time-Invariant system (LTI), followed by a converter from analog to digital (Zero-Order Hold).

The output of the input channel is demodulated using the same sine signal that stimuli the mirror.

The starting parameters used to characterize the model of the input channel are deduced from Cadence simulations of the SD4k input channel itself. Then thanks to numerous simulations performed on the model, great feedbacks on the correct values of the parameter at the variation of the operating condition and environment constraints. have been collected thus allowing a properly input channel design to be performed.

4.2. Immunity enhancement in gyroscope for automotive applications

Micro mechanical gyroscopes are key elements in several automotive systems like roll over detection and mitigation, navigation systems, Electronic Stability Program (ESP) and other systems for vehicle stabilizing and dynamic controlling [37].

Automotive systems are demanding gyroscopes characterized by high accuracy as well as high robustness and immunity against external perturbations (shocks and vibrations). In fact they have to provide an accurate output rate even in presence of environmental shocks and vibrations. One example is the roll over detection: some roll over events are triggered by impact with another object, such a curb, if the resulting shock saturates the gyro system, the airbag may not deploy. In a similar way, if a bump on the road causes a shock or a vibration which is translated into a rotational signal the airbag might deploy when it is not needed.

The vibration immunity can be enhanced by damping the sensing quality factor of the gyro. Indeed an electromechanical gyro is composed by two coupled mechanical systems: a driving system and a sensing system. For the driving system a high quality factor is required in order to have high mechanical excitation with limited driving signals, on the contrary for the sensing system high quality factor involves long settling time, high response overshoot and high sensitivity to unwanted shocks and vibrations. This means that a key point to reduce the shock sensitivity is to control and reduce the gyroscope sensing quality factor.

In literature several quality factor control techniques have been proposed in the last year. For example, in laterally driven micro mechanical resonators [38] the quality factor is reduced by applying an electrostatic force between the planar resonant structure and the substrate in order to reduce the air damping gap. While in disk drive servo systems [39] an adaptive notch filter is usually used to suppress the mechanical resonance of the actuators.

Aim of this section is to present an effective quality factor control strategy which can be applied to different gyroscope types (not only to laterally driven) and without exactly knowing the resonance frequency of the structure. The solution proposed is an electrostatic velocity feedback technique and performs the reduction of the quality factor by applying a “virtual damping” to the system.

The technique developed is presented as follows: section 4.2.1 describes the working principle of a generic micromachined gyroscope, section 4.2.2 presents the working principle of the control loop for immunity enhancement, sections 4.2.3 and 4.2.4 show the feedback implementation, and finally section 4.2.5 presents the simulation results comparing with the state of the art.

4.2.1. Micromachined gyroscope working principle

A vibratory gyroscope measures an angular rate and is based on the transfer of energy between two vibration modes caused by Coriolis acceleration.

The operating principle of a single axis vibratory gyroscope is the following: the driving mass oscillates at resonance frequency around a driving axis (for example the z axis orthogonal to the xy plane of Fig. 50), assuming that the sensing axis is the y axis, any angular rate about the x axis induces a Coriolis acceleration and in turn an oscillation of the sensing mass about the y axis. The applied angular rate (input rate) can be measured by processing the displacement signal in the direction of the sensing axis.

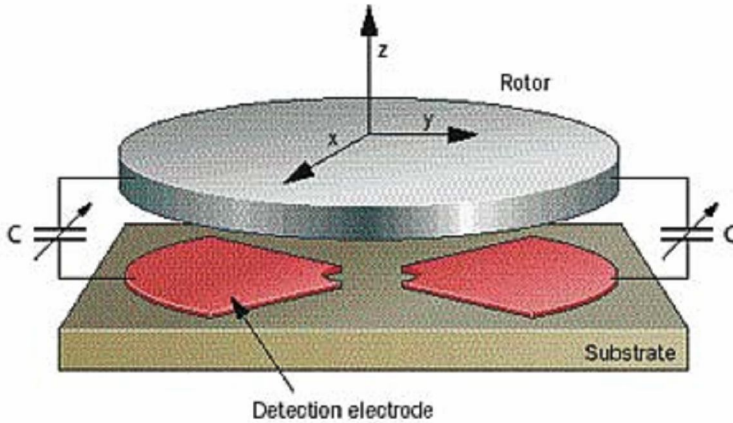


Fig. 50 Vibratory gyroscope principle of working

The sensing mass is a mechanical second order resonant system [40] and its transfer function in the Laplace domain is given by (14).

$$G(s) = \frac{\Omega_s(s)}{M_C(s)} = \frac{\gamma}{\left(s^2 + s \frac{\omega_s}{Q_s} + \omega_s^2 \right)} = \frac{1/I}{\left(s^2 + s \frac{D}{I} + \frac{K}{I} \right)} \quad (14)$$

where Ω_s is the displacement whose amplitude is proportional to the applied mechanical rate, and M_C is the Coriolis momentum, while ω_s and Q_s are respectively the resonance frequency and the quality factor of the sensing system. The following definitions for ω_s and Q_s correlate the resonance frequency and the quality factor to the mechanical characteristics of the sensing system:

$$\omega_s = \sqrt{\frac{K}{I}} \quad \text{and} \quad Q_s = \sqrt{K \cdot I} \frac{1}{D} \quad (15)$$

where K is the spring stiffness, I is the mechanical momentum of inertia and D is the damping factor.

From equation (15) is evident that the quality factor Q_s is inversely proportional to the damping factor D and can be reduced by adding a "virtual damping" (D_v) to the system.

4.2.2. Closed loop control for shock immunity enhancement

This section describes the working principle of an innovative and effective method to improve the performance of a micro mechanical gyroscope by introducing the damping of its sensing quality factor.

Indeed the quality factor of the sensing system is a key parameter for the micromechanical gyroscope dynamic; particularly high sensing quality factor means long settling time, high response overshoot and high sensitivity to external disturbances (shocks and vibrations) that are typical of harsh automotive environment. Gyroscopes employed in automotive systems require high immunity to external shock and this section proposes a new method to reach this goal based on the sensing quality factor damping.

The method here proposed for shock immunity enhancing is based on the reduction of the sensing quality factor by adding a “virtual damping” to the system. Indeed from the study of the sensing system transfer function of the previous section we have seen that the sensing quality factor is inversely proportional to the system damping (15) and consequently can be reduced by increasing the damping by means of a “virtual damping”.

A “virtual damping” can be added with a derivator ($K(s)$) of gain equal to the virtual damping itself (D_v) used in a feedback structure to close the loop on the sensing system, as shown in Fig. 51.

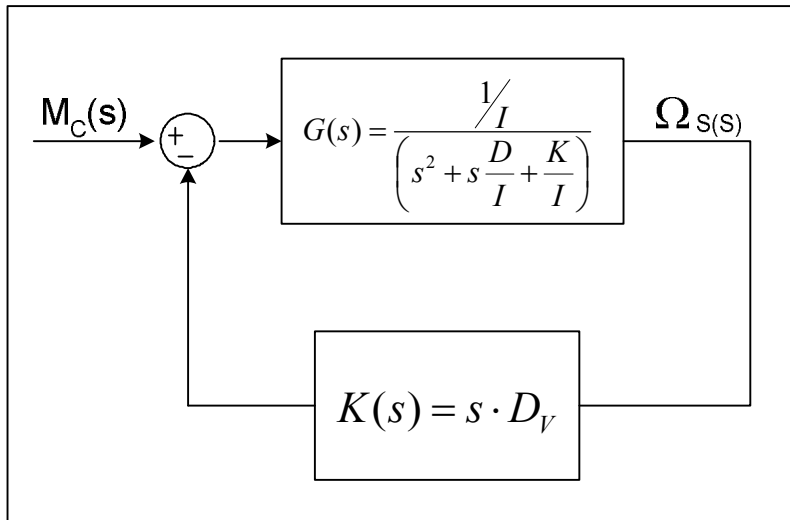


Fig. 51 Closed loop working principle

The transfer function of the closed loop becomes:

$$\frac{\Omega_s(s)}{M_C(s)} = \frac{G(s)}{(1 + K(s)G(s))} = \frac{1}{\left(\frac{1}{G(s)} + K(s)\right)} \quad (16)$$

Replacing $G(s)$ with the sensing system transfer function and $K(s)$ with the derivator transfer function ($K(s) = s \cdot D_v$) the closed loop transfer function is obtained (17).

$$\frac{\Omega_s(s)}{M_C(s)} = \frac{1/I}{\left(s^2 + s \frac{(D + D_v)}{I} + \frac{K}{I} \right)} \quad (17)$$

where D_v is the “*virtual damping*” added to the system.

From (17) we can deduce the quality factor of the closed loop system (Q_{SV}).

$$Q_{SV} = \sqrt{(K \cdot I)} \cdot \frac{1}{(D + D_v)} \quad (18)$$

As expected the quality factor Q_{SV} of the closed loop system has been reduced by applying the feedback and can be controlled trimming the gain D_v of the derivator block.

Stability issue

The stability issue must be considered in order to properly choose the D_v value, in fact in the case of an ideal derivator the system is stable for any value of D_v and the quality factor can be damped without any limitation, but for a real derivator the situation changes.

The stability issue can be addressed by studying the system root locus as shown in the following. Let's suppose to have an ideal derivator ($K(s) = s \cdot D_v$); the resulting root locus (Fig. 52) shows that the system is stable for any D_v value.

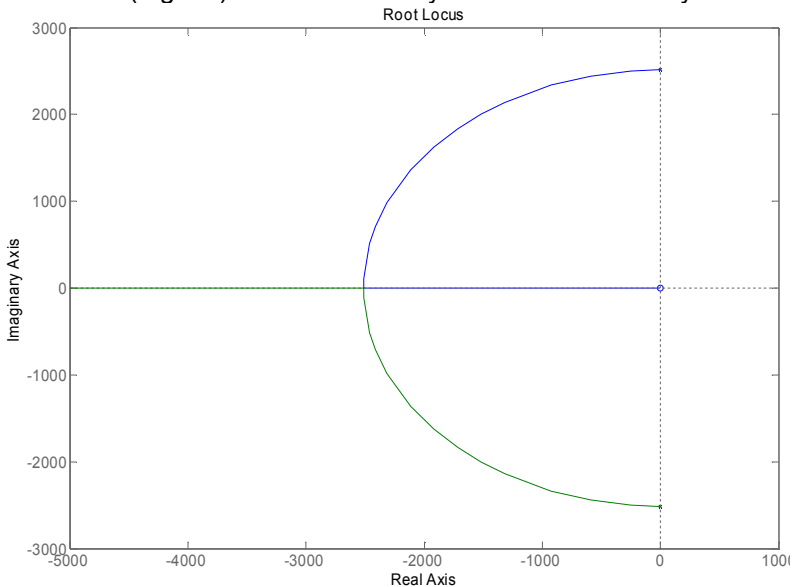


Fig. 52 Root locus of the loop gain $G(s) \cdot K(s)$ for $K(s)$ ideal derivator

In fact the system is characterized by two complex poles and one zero in the origin, when D_V increases the first complex pole moves towards the zero in the negative semi plane (blue line in Fig. 52) while the second one moves towards infinite but remaining in the negative semi plane (green line in Fig. 52) then the system is always stable.

Unfortunately an ideal derivator is not realizable, then in order to have a real system we need a real derivator which has at least one pole and the introduction into the system of one or more poles could lead to instability.

Let's suppose to have a derivator transfer function characterized by two coincident poles as shown in (19).

$$K(s) = \frac{s \cdot D_V}{(s + s_p)^2} \quad (19)$$

where $s_p = \frac{f_D}{10} \cdot 2\pi$ (f_D is the resonance frequency of the driving system).

The resulting root locus is shown in Fig. 53.

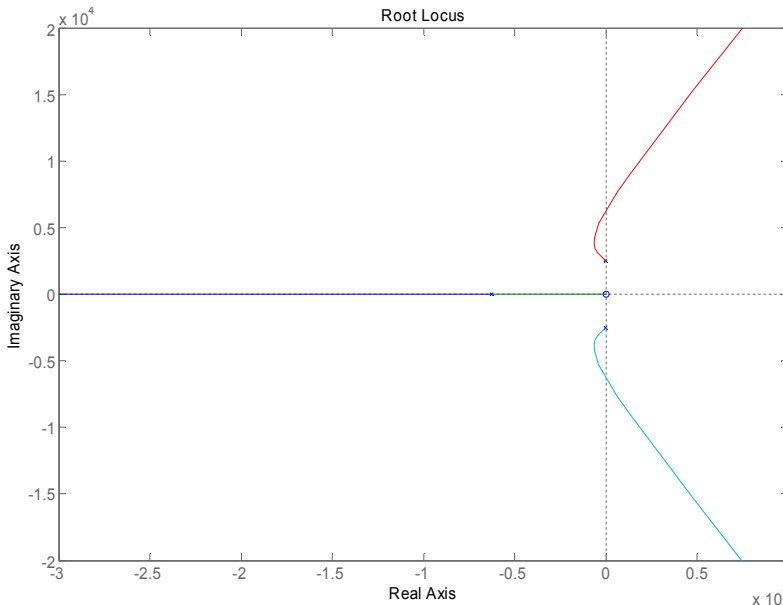


Fig. 53 Root locus of the loop gain $G(s) \cdot K(s)$ for $K(s)$ with 2 poles

In this case the system is characterized by a zero in the origin, two complex poles and two real poles placed in the negative semi plane.

When D_V increases the loop gain increases too and one real pole moves towards the zero (green line in Fig. 53), the other real pole moves towards infinite (blue line in Fig. 53) in the negative semi plane while the two complex poles come across the imaginary axis and move towards infinite in the positive semi plane making the system unstable. In conclusion, there is a range of D_V values in which the system is stable but when D_V overcomes this gap the system becomes unstable.

When the poles number for $K(s)$ transfer function increases the situation changes again; Fig. 54 shows the system root locus when $K(s)$ is characterized by three poles.

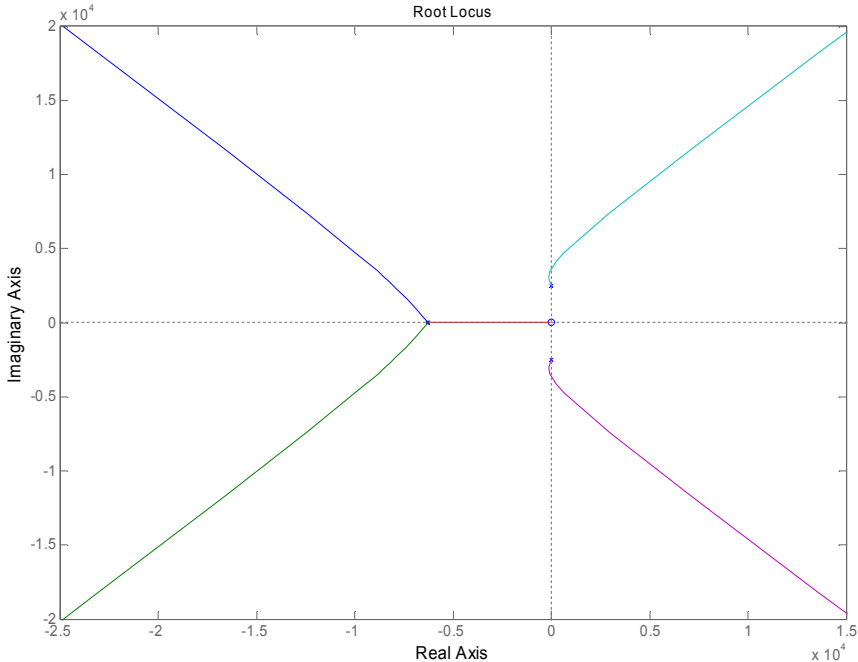


Fig. 54 Root locus of the loop gain $(G(s)*K(s))$ for $K(s)$ with 3 poles

Now the loop is characterized by a zero in the origin, two complex poles and three real poles placed in the negative semi plane. When D_v increases, two real poles move towards infinite in the negative semi plane, one real poles moves towards the zero in the origin and finally the two complex poles come across the imaginary axis and move towards infinite in the positive semi plane making the system unstable. As in the previous case there is a range of D_v values in which the system is stable but when D_v overcomes this range the system becomes unstable. With respect of the case in which $K(s)$ has two poles now the range of D_v value is smaller.

In conclusion the stability problem is a key issue in the design of the control loop, and the value of D_v has to be chosen properly to guarantee the system stability.

In our model a three poles feedback derivator has been chosen because even if the stability range is smaller, simulation results show that this solution is more efficient since the same quality factor reduction is obtained applying a smaller feedback momentum.

4.2.3. Closed loop control implementation: Simulink™ model

Possible feedback solutions

In a capacitive gyroscope the Coriolis momentum induces a mechanical displacement of the sensing mass that causes a variation in the capacitance of the sensing electrodes. The feedback chain described in the previous section (Fig. 51) adds to the Coriolis momentum a feedback momentum which damps the transient response due to the natural modes of the system.

This feedback momentum is generated by applying a voltage to the gyro by means of dedicated capacitive electrodes that in the following will be called “feedback electrodes”.

In literature an electrostatic feedback technique based on the principle described above has been already presented [40] and Fig. 55 shows the solution adopted for its implementation.

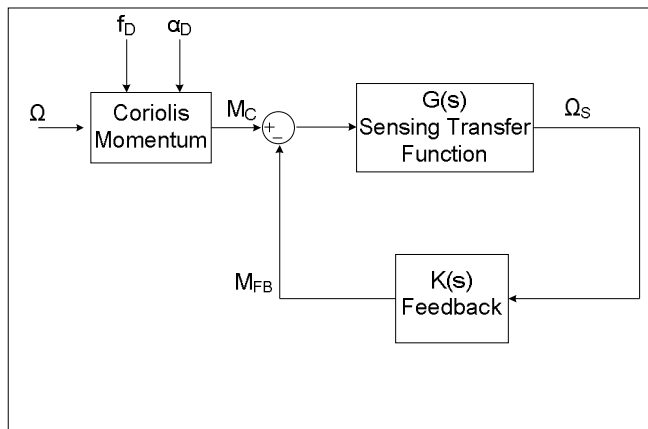


Fig. 55 Pass band solution presented in [40]

In the solution of Fig. 55 the input of the feedback chain is directly the sensor output, then the loop must work in the frequency domain imposed by the gyroscope (pass band frequency domain). Consequently the loop works at high frequencies and this can be a drawback if the whole read out system employs digital blocks. In fact high frequency means high power consumption and thereby a base band solution is more desirable instead of a pass band solution.

The new solution developed is a base band approach for the implementation of the feedback technique.

In fact in the proposed solution the feedback chain includes a demodulation stage (already used for the rate detection in the whole system) and a modulation stage (used to produce a feedback momentum which can be added to the Coriolis momentum) as shown in Fig. 56. Consequently the loop works in base band frequency domain. The use of a modulator and a demodulator stage does not involve a higher employment of electronic circuitry with respect to the previous solution. In fact the modulator stage can be implemented by the same digital block already used for rate demodulation in time sharing.

Please note that this solution does not involve latency problems because the sampling frequency for the signal processing in the digital part of the system is

much lower than the system clock. Both solutions have been implemented and simulated in Simulink™ environment to perform an objective comparison, but in following sections we focus on our base band proposal.

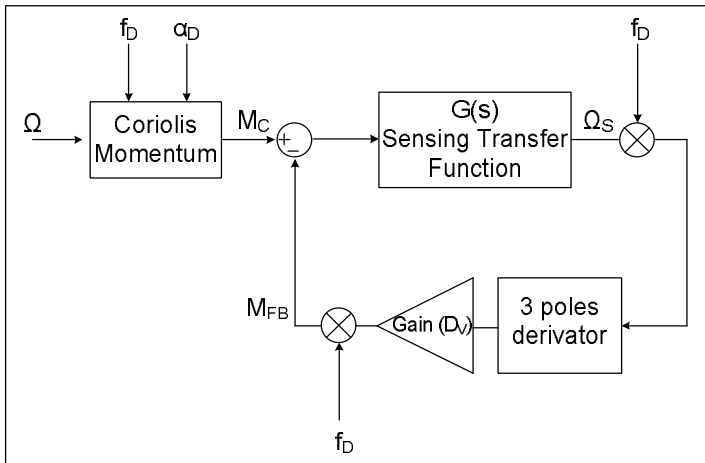


Fig. 56 Base band proposed solution

Base band solution Simulink™ model

The block diagram of the Simulink™ model developed for the base band feedback study is shown in Fig. 57.

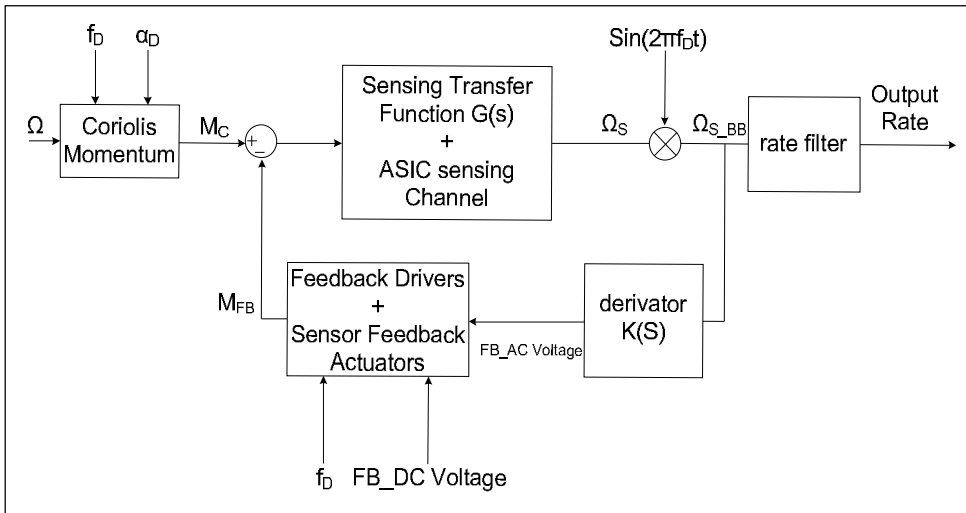


Fig. 57 Block diagram of the Simulink™ model

The model consists of a vibratory gyroscope model, a demodulation stage and a feedback loop. The input rate Ω together with the oscillation of the driving system (characterized by a frequency f_D and a phase α_D) produces a Coriolis momentum that causes the motion of the sensing mass. This motion is detected and elaborated to obtain the output rate. The block “Sensing Transfer Function+ASIC

sensing channel" of Fig. 57 models both the gyro transfer function and the electronic needed to readout the capacitive sensing signal.

The Coriolis momentum ($M_C(t)$) is modelled by implementing the well note expression:

$$M_C(t) = -2I\Omega(t) \times v_D(t) \quad (20)$$

where $\Omega(t)$ is the input rate, I is the driving system momentum of inertia and $v_D(t)$ is the angular velocity of the driving system that oscillates at the resonance frequency.

The demodulation stage is composed of the demodulator and a low pass filter (rate filter). And finally the feedback loop is composed of a three poles derivator ($K(s)$) of gain equal to D_V followed by a modulation stage and the model of the electronic circuitry for the actuation of the feedback electrodes.

The feedback momentum responsible for the sensing quality factor damping arises from the application to the feedback gyro electrodes of two opposite voltages (V_{FB_R} and V_{FB_L}) given by:

$$V_{FB_R} = V_{FB_DC} + V_{FB_AC} \sin(\omega_D t) \quad (21)$$

$$V_{FB_L} = V_{FB_DC} - V_{FB_AC} \sin(\omega_D t) \quad (22)$$

where $\omega_D = 2\pi f_D$ with f_D driving resonance frequency, V_{FB_DC} is the DC feedback voltage and V_{FB_AC} is the AC feedback voltage generated by the control loop.

The feedback momentum (M_{FB}) is the difference between the two electrostatic momenta generated by the voltages expressed in (21) and (22).

$$\begin{aligned} M_{FB} &= M_{FB_R} - M_{FB_L} = \frac{1}{2}(V_{FB_R}^2 - V_{FB_L}^2) \frac{dC_{FB}}{d\alpha_{FB}} = \\ &= \frac{1}{2} \frac{dC_{FB}}{d\alpha_{FB}} (4V_{FB_DC}V_{FB_AC} \sin(\omega_D t)) = 2K_{fdbk}(V_{FB_DC}V_{FB_AC} \sin(\omega_D t)) \end{aligned} \quad (23)$$

where C_{FB} and α_{FB} are respectively the capacitance and the rotation angle of the feedback electrodes.

In the Simulink™ model (Fig. 58.) the feedback momentum is implemented with the product expressed by (23).

Indeed the derivator output (V_{FB_AC}) is multiplied to three factors:

- a constant value equal to the DC feedback voltage (V_{FB_DC});
- a constant factor equal to 2;
- a sinusoidal wave which is the same wave used to model the driving velocity ($\sin(\omega_D t)$), this is the modulation stage.

The product obtained is finally multiplied for the constant term K_{fdbk} thus obtaining the feedback momentum.

In order to have a model as close as possible to a real system the physical sensor parameters ($2I$ and $dC_{FB}/d\alpha_{FB}$) have been extracted from laboratory

measurements on a real automotive yaw gyro (developed by Sensordynamics AG) and are included respectively in the parameters K_{Cor} and K_{fdbk} of the model.

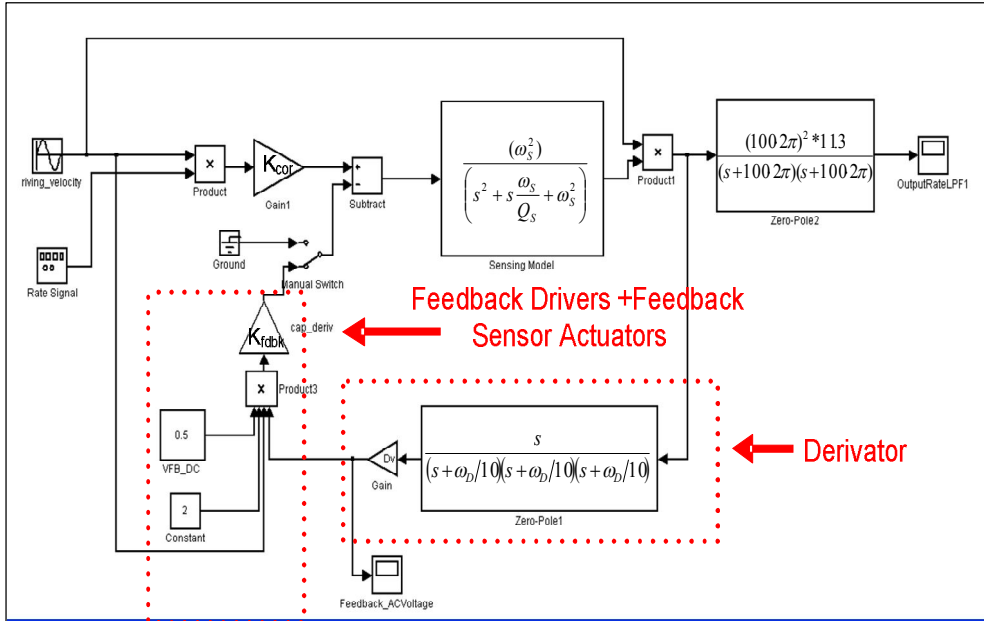


Fig. 58 Simulink™ model of the feedback loop applied to a real yaw gyro readout system.

An analytical study of the system has been performed in order to find an analytical expression for the amplitude A and the phase φ of the output rate thus verifying from a theoretical point of view the closed loop control effectiveness.

To perform the analytical study, let's consider the block diagram of Fig. 59.

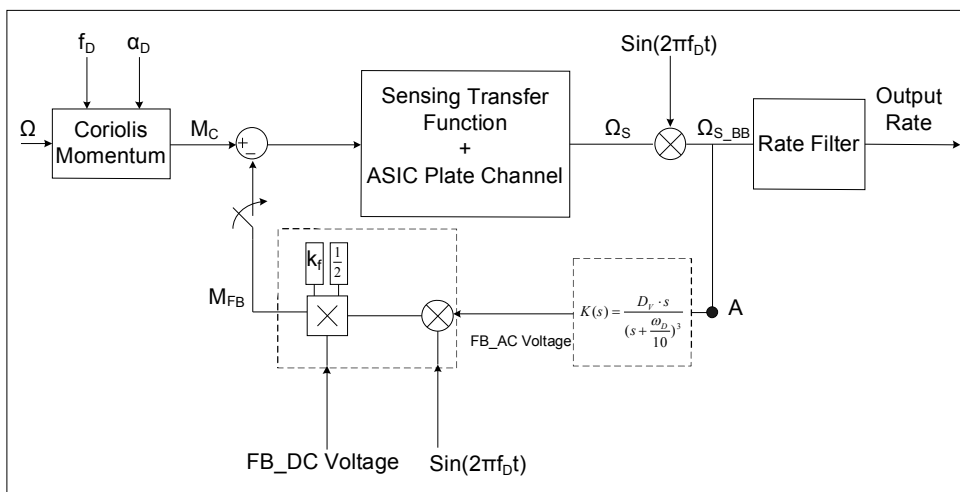


Fig. 59 Block diagram of the Simulink™ model for the analytical study

Assuming that in the point A of the loop we have a signal equal to (24).

$$x = A \sin(\omega_{\Omega} t + \varphi) \quad (24)$$

After the derivator block we have the following signal:

$$V_{FB_AC} = D_V |K(j\omega_{\Omega})| A \sin(\omega_{\Omega} t + \varphi + \angle K(j\omega_{\Omega})) \quad (25)$$

With the assumption that $|K(j\omega_{\Omega} t)|$ and $\angle K(j\omega_{\Omega} t)$ are respectively the amplitude and the phase of the transfer function $K(s)$ at the frequency ω_{Ω} and normalized for D_V .

The feedback momentum responsible for the resonance damping can be deduced directly from the block diagram of Fig. 59 and is:

$$M_{FB} = \frac{K_f V_{FB_DC}}{2} \cdot \sin(\omega_D t) \cdot V_{FB_AC} \quad (26)$$

where $K_f = 4 \cdot (dC_{FB} / d\alpha_{FB})$. Substituting in (26) the expression found for V_{FB_AC} at (25) we have the following feedback momentum expression.

$$M_{FB} = A_{loop} A |K(j\omega_{\Omega})| [\cos(\omega_{diff} t - \varphi - \angle K(j\omega_{\Omega})) - \cos(\omega_{sum} t + \varphi + \angle K(j\omega_{\Omega}))] \quad (27)$$

where $A_{loop} = \frac{K_f V_{FB_DC}}{2} D_V \frac{1}{2}$, $\omega_{diff} = \omega_D - \omega_{\Omega}$ and $\omega_{sum} = \omega_D + \omega_{\Omega}$.

While, remembering the definition of (20) and assuming to have an input rate $\Omega = \Omega \sin(\omega_{\Omega} t)$ and a driving velocity $v_D = \omega_D A_D \sin(\omega_D t + \alpha_D)$ with $\alpha_D = 0$, the Coriolis momentum module is:

$$M_C = 2I\Omega A_D \omega_D \cdot \sin(\omega_D t) \cdot \sin(\omega_{\Omega} t) \quad (28)$$

Developing the sines product:

$$M_C = K_{COR} (\cos(\omega_{diff} t) - \cos(\omega_{sum} t)) \quad (29)$$

where $K_{COR} = I\Omega A_D \omega_D$ and again $\omega_{diff} = \omega_D - \omega_{\Omega}$, $\omega_{sum} = \omega_D + \omega_{\Omega}$.

From the expression of the Coriolis and the feedback momentum the total momentum (M_t) applied to the gyroscope can be calculated.

$$M_t = M_C - M_{FB} = K_{COR} (\cos(\omega_{diff} t) - \cos(\omega_{sum} t)) - [A_{loop} A |K(j\omega_{\Omega} t)| \cos(\omega_{diff} t - \varphi - \angle K(j\omega_{\Omega} t)) - \cos(\omega_{sum} t + \varphi + \angle K(j\omega_{\Omega} t))] \quad (30)$$

Consequently the rate at the output of the sensing system will be:

$$\Omega_S = |G(j\omega_{diff})| \left[\frac{K_{COR} \cos(\omega_{diff} t + \angle G(j\omega_{diff})) - A_{loop} A |K(j\omega_{\Omega})| (\cos(\omega_{diff} t - \varphi - \angle K(j\omega_{\Omega} t)) + \angle G(j\omega_{diff}))}{2} \right] + |G(j\omega_{sum})| \left[\frac{-K_{COR} \cos(\omega_{sum} t + \angle G(j\omega_{sum})) + A_{loop} A |K(j\omega_{\Omega})| (\cos(\omega_{sum} t + \varphi + \angle K(j\omega_{\Omega} t)) + \angle G(j\omega_{sum}))}{2} \right] \quad (31)$$

The signal Ω_S is demodulated by using the signal $\sin(\omega_D t)$. Then the signal after the demodulation stage is the base band:

$$\Omega_{S_BB} = \Omega_S \cdot \sin(\omega_D t) \quad (32)$$

The demodulated signal has components at different frequency values but the components at the ω_Ω frequency are:

$$\Omega_{S_BB}(j\omega_\Omega) = \frac{|G(j\omega_{sum})|}{2} \left[\begin{array}{l} -K_{COR} \sin(\omega_\Omega t + \angle G(j\omega_{sum})) + \\ A_{loop} |K(j\omega_\Omega)| \sin(\omega_\Omega t + \varphi + \angle K(j\omega_\Omega) + \angle G(j\omega_{sum})) \end{array} \right] \quad (33)$$

We know that:

$$\begin{aligned} & \sin(\omega_\Omega t + \varphi + \angle K(j\omega_\Omega) + \angle G(j\omega_{sum})) = \\ & = \sin(\omega_\Omega t + \varphi) \cos(\angle K(j\omega_\Omega) + \angle G(j\omega_{sum})) + \cos(\omega_\Omega t + \varphi) \sin(\angle K(j\omega_\Omega) + \angle G(j\omega_{sum})) \end{aligned} \quad (34)$$

and we can write that:

$$\begin{aligned} & \sin(\omega_\Omega t + \angle G(j\omega_{sum})) = \\ & = \sin(\omega_\Omega t + \varphi - \varphi + \angle G(j\omega_{sum})) = \\ & = \sin(\omega_\Omega t + \varphi) \cos(\angle G(j\omega_{sum}) - \varphi) + \cos(\omega_\Omega t + \varphi) \sin(\angle G(j\omega_{sum}) - \varphi) \end{aligned} \quad (35)$$

Substituting (34) and (35) in expression of the demodulated angular rate Ω_{S_BB} we obtain an elaborated expression which must be equal to $x = A \sin(\omega_\Omega t + \varphi)$, since we have started from the hypothesis that in the point A the signal is equal to x.

Then in order to have a consistent system the following equality must be respect.

$$\Omega_{S_BB}(j\omega_\Omega) = A \sin(\omega_\Omega t + \varphi) \quad (36)$$

From which the analytical expression of the amplitude A and the phase φ of the base band rate can be extracted:

$$A = \frac{-\frac{|G(j\omega_{sum})|}{2} \cdot K_{COR}}{1 - \frac{|G(j\omega_{sum})|}{2} A_{loop} |K(j\omega_\Omega)| \cos(\angle G(j\omega_{sum}) + \angle K(j\omega_\Omega))} \cos(\angle G(j\omega_{sum}) - \varphi) \quad (37)$$

$$\varphi = \angle G(j\omega_{sum}) - \text{tg}^{-1} \left(\frac{K_2}{K_{COR}} \right) \quad (38)$$

with the following definitions:

$$K1 = \frac{-\frac{|G(j\omega_{sum})|}{2} \cdot K_{COR}}{1 - \frac{|G(j\omega_{sum})|}{2} A_{loop} |K(j\omega_{\Omega})| \cos(\angle G(j\omega_{sum}) + \angle K(j\omega_{\Omega}))} \quad (39)$$

$$K2 = K1 \cdot A_{loop} |K(j\omega_{\Omega})| \sin(\angle K(j\omega_{\Omega}) + \angle G(j\omega_{sum})) \quad (40)$$

Plotting the analytical amplitude expression of (37) as a function of the input frequency ($0 \leq f_{\Omega} \leq 2000 \text{ Hz}$) and for different D_V values we have a theoretical confirmation that the loop effectively damps the resonance.

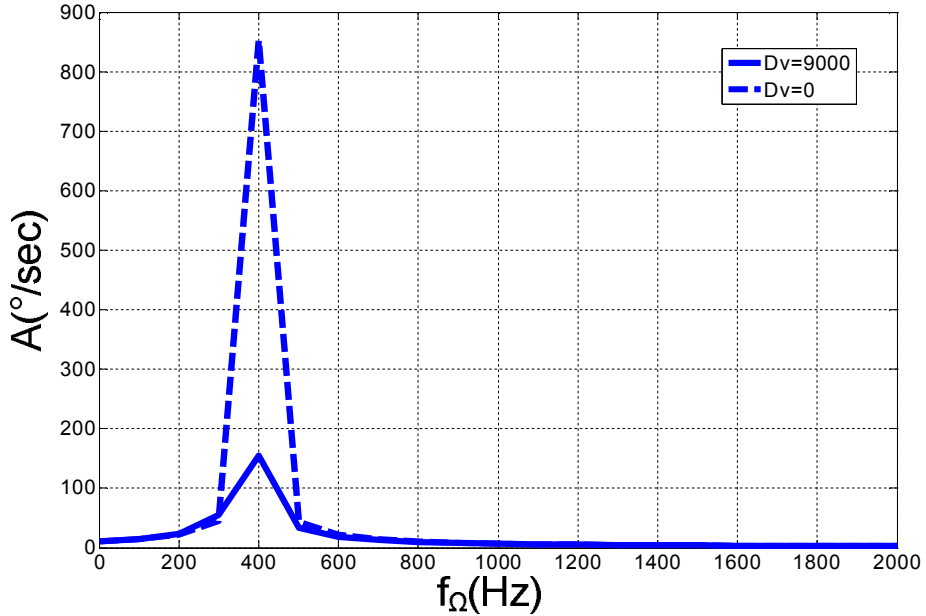


Fig. 60 Output rate amplitude versus input rate frequency for feedback disabled (broken line), and feedback enabled (unbroken line)

As expected the resonance peak is lowered by the feedback loop. The peak of the frequency response is in correspondence of $f_{\Omega}=400 \text{ Hz}$ because the simulations have been performed by assuming a resonance frequency for the driving system $f_D=10 \text{ KHz}$, and a resonance frequency for the sensing system $f_S=10.4 \text{ KHz}$.

For $D_V=0$ the feedback is disabled and the resonance peak is around $850 \text{ }^\circ/\text{sec}$, while for $D_V=9000$ the feedback is enabled and the resonance peak is lowered to $150^\circ/\text{sec}$.

The D_V value has been chosen equal to $9000A$ because this is the maximum D_V value which guarantees the system stability.

4.2.4. Closed loop control implementation: enhanced model

In order to studies secondary effects that can heavily affect the closed loop control technique an *enhanced model* has been developed that take into account the most important of this effects: the variation of the gyro resonance frequency due to the voltage applied to the feedback electrodes.

Experimental measurements performed on the real yaw gyro used in the close loop control model show that the sensing resonance frequency depends on the feedback voltage. Particularly the variation of the resonance frequency (Δf_s) is given by (41).

$$\Delta f_s = -50 \left(V_{FB_DC}^2 + \frac{1}{2} V_{FB_AC}^2 \right) \quad (41)$$

where V_{FB_DC} and V_{FB_AC} are respectively the DC component and the AC component of the feedback voltage applied to the gyro.

In order to see how this phenomenon affects the feedback technique, an enhanced model has been developed in which the transfer function of the sensing system has been implemented taking into account the resonance variation. The transfer function $G(s)$ of (14) can be elaborated as follows:

$$\begin{aligned} \Omega_s(s) \cdot \left(s^2 + s \frac{\omega_s}{Q_s} + \omega_s^2 \right) &= M_c(s) \cdot \gamma \\ \Omega_s(s) \cdot \left(1 + \frac{\omega_s}{Q_s} \frac{1}{s} + \omega_s^2 \cdot \frac{1}{s^2} \right) &= M_c(s) \cdot \gamma \frac{1}{s^2} \\ \Omega_s(s) &= M_c(s) \cdot \frac{\gamma}{s^2} - \Omega_s(s) \cdot \frac{\omega_s}{Q_s} \cdot \frac{1}{s} - \Omega_s(s) \cdot \frac{\omega_s^2}{s^2} \end{aligned} \quad (42)$$

where γ depends on the momentum of inertia and isn't affected by the resonance variation. In our model γ has been set to the square value of the nominal resonance frequency.

The block diagram of the resulting model is shown in Fig. 61.

In the enhanced model a new block has been added ("variable ω_s generator" of Fig. 61) which generates the variable sensing pulsation by adding the variation $\Delta\omega_s = 2\pi\Delta f_s$ to the nominal resonance pulsation. Where Δf_s is the variation obtained by experimental results and expressed by (41).

The gyro model is a Simulink™ block that implements the expression of (42) where ω_s is the variable pulsation obtained as output of the new block added.

The results of simulations performed by using the enhancement model, show that the feedback loop keeps working properly also taking into account secondary effects such as the variation of the resonance frequency due to applied feedback voltage, as will be discussed in the next section.

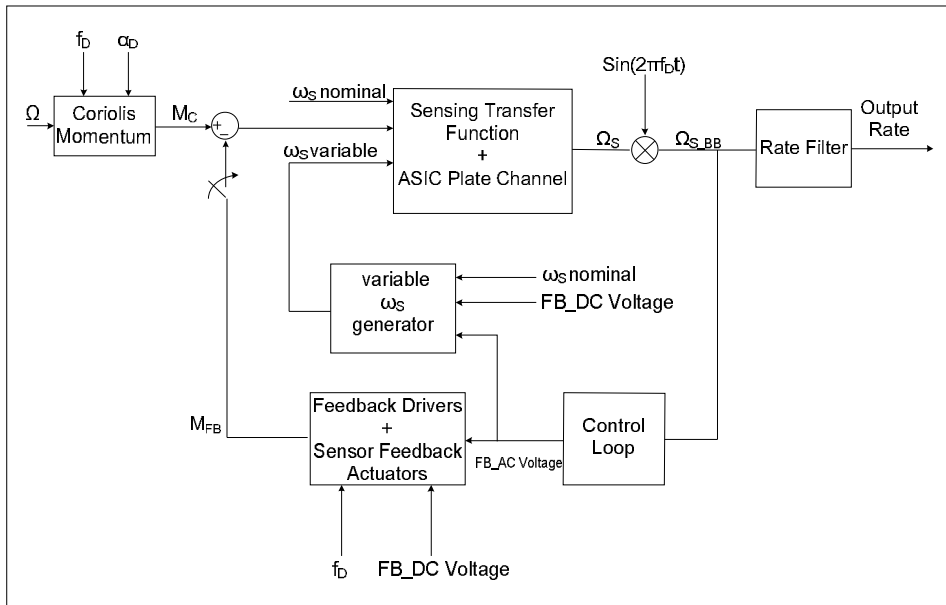


Fig. 61 Block diagram of the enhanced base band feedback model

4.2.5. Simulation results

In this section the results of the feedback models previously described are presented. More in details, a first section shows the simulation results related to the simple base band feedback implementation, a second section presents the simulation results related to the enhanced base band model and finally a third section compares the pass band solution proposed in this research work and the base band feedback implementation already presented in the state-of-the-art..

Simulation results of the base band feedback model

The feedback model is simulated by applying the following model setup:

- Input square wave characterized by:
 - amplitude $\Omega=100^\circ/\text{sec}$;
 - frequency $f_D=6.1$ Hz.
- Gyroscope physical characteristic:
 - sensing quality factor : $Q_S=1000$;
 - driving resonance frequency: $f_D=10$ KHz;
 - sensing resonance frequency: $f_S=10.4$ KHz;
- Model parameters:
 - experimental coefficients: $K_{Cor}=3.419, K_{fdbk}=1.284 \times 10^3$;
 - rate filter: second order low pass filter (cut frequency equal to 100 Hz);
 - feedback chain: $D_V=9000$ (maximum value to keep the system stable).

In order to see the effect of the control loop on the output rate, the simulation is performed starting from the condition in which the loop is disabled and enabling the

loop after a certain delay. The following figure shows the output rate resulting from simulation when the feedback chain is enabled after a delay of 0.2 sec.

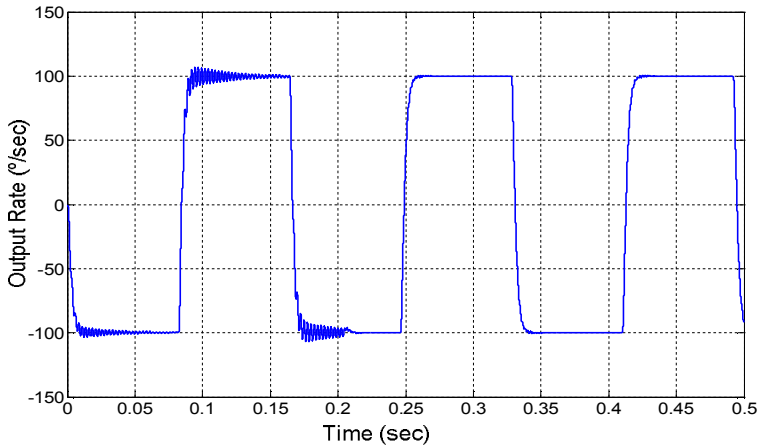


Fig. 62 Output rate. The feedback chain is enabled after 0.2 seconds.

As long as the feedback is disabled there is a residual oscillation, due to the 400 Hz component of the input square wave, which is completely suppressed when the loop is enabled. The residual oscillation could be suppressed by using a more selective low pass filter on the output rate but this approach entails two drawbacks:

1. the system bandwidth is limited;
2. the oscillation inside the system is not suppressed (this could be a problem for a correct system working).

In the simulations of the control loop technique we have to consider an important limitation of the real system which is the *maximum feedback voltage* that the system can apply to the gyroscope. This condition involves a further limitation on the D_V value, since the feedback voltage amplitude is mainly due to the D_V value itself which represents the gain of the derivator used for the resonance suppression.

Consequently the D_V value must be chosen taking into account not only the system stability (as said in section 4.2.2) but also the maximum feedback voltage supported by the system.

In order to see how this limitation of the real system affects our model the base band feedback control has been simulated by increasing the input square wave amplitude until reaching the maximum feedback voltage amplitude.

In fact when the amplitude of the input square wave (Ω) increases the feedback voltage needed to perform the damping arises too. Assuming that the maximum feedback voltage allowed by the system is 0,5V (saturation limit) and keeping D_V equal to the maximum value for the stability of the system ($D_V=9000$), the maximum amplitude of the input square wave for which there isn't any saturation effect is roughly 200°/sec.

This value has been extracted by including a saturator block in the model and varying Ω between 0 and 1000°/sec (Fig. 63) with a step of 100°/sec.

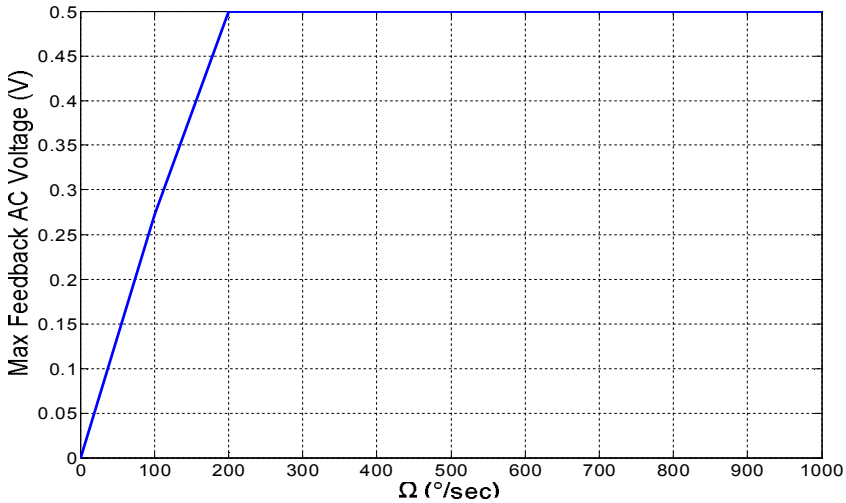


Fig. 63 Maximum feedback voltage applied to the gyroscope versus input rate amplitude

When the amplitude of the input rate reaches 200°/sec the feedback voltage saturates at 0,5V and we expect a worse residual oscillation suppression.

A residual oscillation suppression involves a higher overshoot on the output rate, then in order to see the impact of the system saturation on the control loop performance, the overshoot on the output rate has been calculated varying Ω from 0 to 1000°/sec with step of 100°/sec.

Simulation results show that the saturation of the feedback voltage does not appreciably affect the output overshoot.

When Ω exceeds 200°/sec the slope of the overshoot curve slightly increases as expected but this does not significantly change the effectiveness of the feedback loop.

The ideal behaviour of the model (without any saturation effect) is compared with the real behaviour in Fig. 64. Indeed the curve drawn with a broken line in shows overshoot on the output rate when any saturator block is included, while the straight line curve represents the overshoot on the output rate when the inclusion of a saturation block in the model limit the feedback voltage applied .

Starting from an input amplitude of 200°/sec the two curves are not coincident any more, but in any case the maximum overshoot on the output rate is equal to 0.03°/sec.

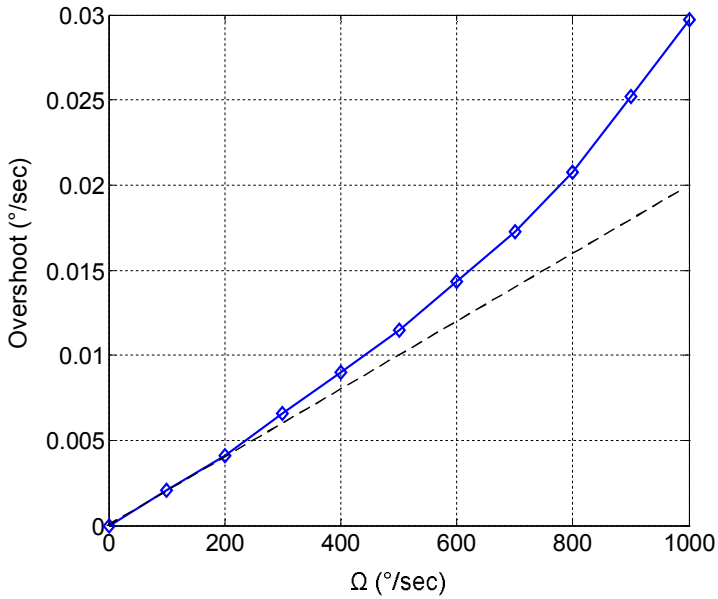


Fig. 64 Output rate overshoot versus input rate amplitude

The advantages due to the introduction of the feedback loop are evident from the overshoot analysis in the two cases of feedback disabled and feedback enabled. Fig. 65 shows that the feedback for the resonance damping significantly reduces the output overshoot with the benefit of higher vibration immunity.

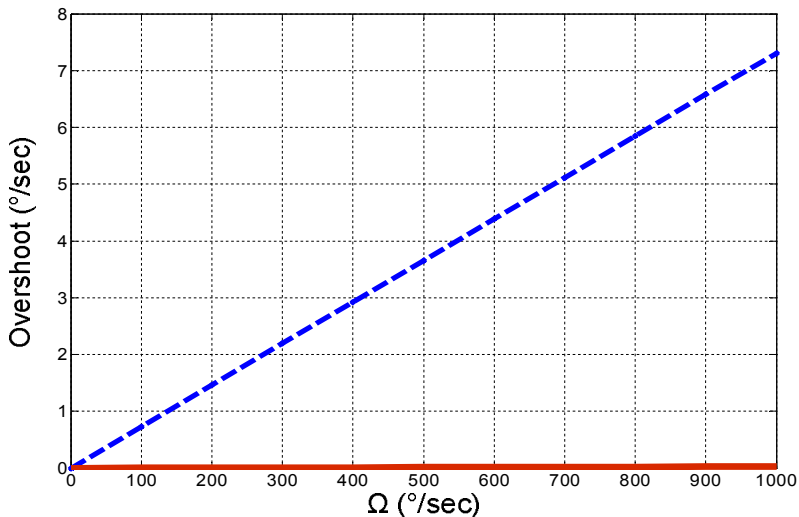


Fig. 65 Output rate overshoot with (unbroken red line) and without (broken blue line) feedback loop

The maximum overshoot in the case of feedback enabled is $0.03^\circ/\text{sec}$, against a maximum overshoot of $7^\circ/\text{sec}$ when the feedback is disabled.

Simulation results of the enhanced base band feedback model

The system still works properly when taking into account the variation of the resonance frequency due to the feedback voltage. In fact simulation results show that the overshoot resulting from the enhanced model is even lower than the overshoot resulting from the simple model (Fig. 66).

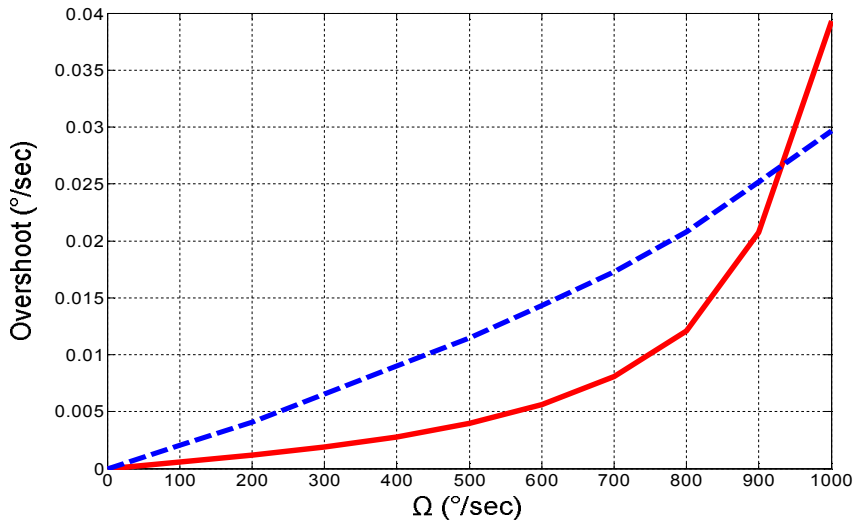


Fig. 66 Output overshoot for base band simple model (broken blue line) and for enhanced base band model (unbroken red line)

In Fig. 66 the overshoot for the enhanced base band model (red line) is compared with the overshoot for the base band simple model (blue line).

We can see that taking into account the dependence of the sensing frequency f_s from the feedback voltage the overshoot doesn't increase. In fact when the input rate amplitude belongs to the interval ($0^\circ/\text{sec}$ - $920^\circ/\text{sec}$) the overshoot for the enhanced model is even lower the overshoot for the simple model. When the input amplitude overcomes $920^\circ/\text{sec}$ the overshoot for the enhanced model becomes higher but in any case is much lower the overshoot in the case of loop disabled ($0.039^\circ/\text{sec}$ against $7^\circ/\text{sec}$).

Comparison between the base band and the pass band model

The control loop technique proposed is a base band solution, as said in section 4.2.3 in literature an analogue technique exists which adopts a pass band solution and does not take into account the real effects already mentioned regarding the sensing frequency variation and the saturation of the feedback voltage.

In order to perform an objective comparison the pass band feedback technique has been modelled and simulated too.

The analysis of the obtained results shows that the pass band implementation has a lower efficiency, in fact a higher feedback voltage is needed to perform the resonance damping. Consequently the saturation of the feedback voltage occurs

for lower value of the input rate amplitude. In fact the feedback saturation voltage is in correspondence of an input rate of $120^\circ/\text{sec}$ instead of $200^\circ/\text{sec}$ Fig. 67.

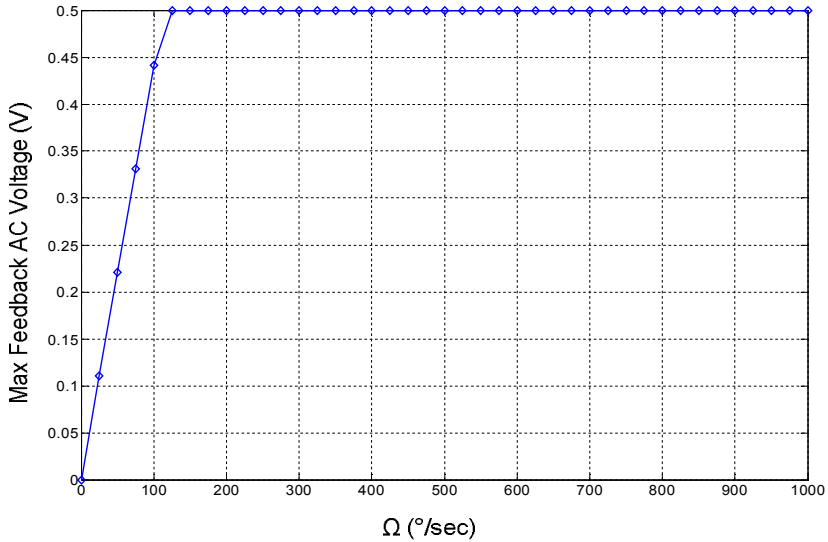


Fig. 67 Maximum feedback voltage versus amplitude for pass band implementation

One of the drawback of a lower efficiency is that the saturation voltage is reached for lowest input rate amplitude and consequently the interval of input rate amplitude in which the system work without saturating is smaller.

Moreover while for the base band solution once the saturation is reached the system continues working properly, in the case of pass band solution after the saturation the system does not work properly.

CONCLUSIONS

This work addressed the study of MEMS design flow by focusing on two key design factors: the first is the developing of tools and methodologies to enhance a generic MEMS design flow and the second is MEMS modelling.

The research work started with a deep study an analysis of a generic MEMS design flow which has allowed to put in evidence which are the fundamental steps and the ultimate goal of a successful design flow as well as they key issues that must be addressed in order to reach it.

In order to have a design flow as close as possible to the optimum one, two steps must be added before the production, the *layout verification* and the *layout simulation*.

Check of the layout performed in layout verification is a fundamental step before the production, and in the same way layout simulations are very useful to guarantee a successful MEMS design, since in simulating the layout the designer can often better determine the mechanical properties thus allowing a fine tuning of the system level sensor model.

Moreover, to reach the goal to have a sensor model that reflects the real sensor behaviour, some secondary effects, which can only be known after the layout realization, must be taken into account, such as the parasitic capacitances. Algorithms tools for MEMS layout verification, post layout simulations and parasitic capacitance extraction are active area of research, but currently no off-the-shelf tools are available, hence custom tools must be developed.

In the first part of this research work these issues have been addressed by developing a tool to perform LVS (layout versus schematic check) of MEMS sensor and a methodology for post layout simulations together with a further tool for the automatic parasitic capacitances extraction.

The automatic tool for performing LVS check of MEMS has been developed within the same environment usually adopted to realize the MEMS layout (Cadence™ environment) and its working principle is based on the comparison between the sensor layout and a schematic which represents the sensor itself. In addition the tool can generates a GDSII file where sensor regions characterized by different electric potentials are highlighted with different colours thus providing a quick way for checking shortcuts.

As mentioned before another crucial step in MEMS design flow is the elaboration of a model as close as possible to the real device. In order to reach this goal, a methodology to perform post layout simulations has been developed and presented. Post layout simulations are FEM simulations performed on the real sensor layout. The methodology developed extracts information from a GDSII file which represents the real sensor and then uses this information to build a FEM model that can be then simulated. The methodology proposed overcomes the traditional issues of post layout simulations (which are mainly the complexity of the sensor structure that must be simulated and the compatibility problem between the FEM simulation environment and MEMS layout environment) thus showing the

possibility to have a linear, quick and reliable flow for performing post layout simulations.

Moreover in order to have an exact MEMS model also secondary effects must be considered such as parasitic capacitances, then a tool has been developed that starting from the sensor layout automatically extracts its parasitic capacitances thus allowing to have a quick and reliable way to determine the parasitic capacitance for a generic MEMS sensor.

Both LVS tool and post layout simulations together with the tool for parasitic capacitance extraction were successfully applied to the design flow of real gyroscopes manufactured at Fraunhofer Institute for Silicon Technology (Itzehoe, Germany). From these design experiences the effectiveness of LVS tool emerged in detecting layout errors before the production, while the benefit of post layout simulations was clear in tuning the sensor model and then allowing, if required, the redesign of the sensor before manufacturing. Also the knowledge of the parasitic capacitances extracted with the custom toll has proved to be very effective in completing the sensor high level model employed then in the development of the sensor conditioning system.

From the analysis of a generic MEMS design flow a fundamental observation comes out: MEMS modelling is a key step in MEMS design.

For this motivation the second part of this research work has been dedicated to MEMS modelling with reference to two applications studies: a micromirror for laser projection systems and a closed loop control for shock immunity enhancement in gyroscopes for automotive applications.

The first case study refers to the model of a torsional micromirror for laser projection systems fabricated at Fraunhofer Institute for Silicon Technology. Starting from FEM simulations needed to extract the physical characteristic micromirror parameters, a Simulink™ model has been developed which describes the device in a complete way from both a mechanical and an electrostatic point of view. The effectiveness of the model has been proved by laboratory measurements performed on a real micromirror sample. And the model has proven to be very useful in the design of the read out circuitry, indeed the model has been included in the high level model of the whole mirror conditioning systems and has been fundamental in the defining of the system itself.

The second case study is the design and development of an innovative and effective control loop to improve the performance of a micro mechanical gyroscope for automotive applications. Starting from a theoretical study of the control loop working principle, a Simulink™ model has been developed which integrates together the gyroscope model and the loop model. Simulation results show that the control loop developed involves an effective enhancement of the shock immunity and that the proposed solution outperforms similar solutions already presented in the state of the art.

BIBLIOGRAPHY

1. C.S. Smith, "Piezoresistive effect in germanium and silicon", *Phys. Rev.*, Vol. 94, no. 1, Apr. 1954, pp. 42-49.
2. Yole market research, "Global MEMS market forecast 2007-2012", (www.yole.fr).
3. A. Selvakumar, N. Yazdi and K. Najafi, "A wide-range micromachined threshold accelerometer array and interface circuit", *Journal of Micromechanics and Microengineering*, Vol. 11, no. 2, Mar 2001, pp. 118-125.
4. Lynn F. Fuller, Steven Sudirigo, "Bulk Micromachined Pressure Sensor", http://people.rit.edu/lffeee/Fuller_Bulk_MEMS_Pressure_Sensor.pdf
5. Lucas NovaSensor, Data Sheet: NPC-107 Series Disposable Medical Pressure Sensor, <http://www.novasensor.com/>.
6. A. P. Lee, D. R. Ciarlo, P. A. Krulevitch, S. Lehw, J. Trevino and M. A. Northrup, "A Practical Microgripper by Fine Alignment, Eutetic Bonding and SMA Actuation", *Proc. of International Solid-State Sensors and Actuators Conference (Transducers '95)*, 1995, pp. 368-371
7. U.S. Patent 5,629,577, " Piezoelectric microactuator useful in a force-balanced scalpel."
8. G. M. Rebeiz, " RF MEMS, Theory, Design and Technology ", *John Wiley & Sons*, 2003.
9. X. Ding, W. Czarnocki, J. P. Schuster and B. Roeckner " DSP-Based CMOS Monolithic Pressure Sensor for High Volume Manufacturing ", *The 10th International Conference on Solid-State Sensors and Actuators (Transducers '99)*, 1999, pp. 2B3.5.
10. M. Yasushi et al, "Development of Intelligent Parking Assist", *Journal of the Society of Automotive Engineers of Japan*, Vol. 60, no. 10, 2006, pp. 47-52.
11. C. J. Murray, "Lexus LS 460 Parking System Grabs the Wheel", *Design News*, 2007.
12. M. Douglass, " DMD reliability: a MEMS success story ", *Proc. of SPIE*, Vol. 4980, 2003, pp. 1-11.
13. J.F. Lo, Shin-Jui Chen Hongyu Yu Chi, D. Chuang-Yuan Lee Marcu, L. Eun Sok Kim, M. Gundersen, " Multi-Cantilever-Driven Rotational Micrograting for MOEMS Spectrometer ", *Solid-State Sensors, Actuators and Microsystems Conference*, 2007, pp. 2421-2424.
14. W. O. Davis, R. Sprague, J. Miller, " MEMS-based pico projector display", *Optical MEMs and Nanophotonics, 2008 IEEE/LEOS International Conference*, August 2008, pp. 31-32.
15. <http://www.microvision.com>
16. G.K. Fedder, "Structured Design of Integrated MEMS", *Proc. MEMS '99*, 1999, pp. 1-8.
17. S.D. Senturia, "CAD Challenges for Microsensors, Microactuators, and Microsystems", *Proc. IEEE*, Vol. 86, no. 8, Aug. 1998, pp. 1611-1626.
18. <http://www.ansys.com> .
19. <http://www.coventor.com> .
20. <http://www.corningintellisense.com> .
21. U. Triltsch , S. Buttgenbach, " Next generation of TCAD environments for MEMS design", *Proc. Symposium on Design, Test, Integration and Packaging of MEMS/MOEMS 2008*, 2008, pp. 91-95.

22. R. Ardito, L. Baldassarre and A. Corigliano, "On the Numerical Evaluation of Capacitance and Electrostatic Forces in MEMS", *Issue of EuroSimE 2009*, April 2009, pp. 1-8.
23. F. Jr. Williamson, "Richard Courant and the Finite Element Method: A Further Look", *Historia Mathematica Toronto*, Vol. 7, no. 4, 1980, pp. 369-378.
24. M. Lagouge, "Matthieu Lagouge's PhD project - Microprobes", http://matthieu.lagouge.free.fr/phd_project/microprobes.html
25. <http://www.matlab.com>
26. K.E. Petersen, B. Noble and I.N. Sneddon, " Silicon Torsional Scanning Mirror", *IBM Journal of Research and Development*, Vol. 24, no. 5, Sept. 1980, pp. 631-637.
27. R. Sprague, T. Montague, D. Brown, "Bi-axial magnetic drive for Scanned Beam Display mirrors", *Proc. of MOEMS Display and Imaging Systems III, Proc. of SPIE*, Vol. 5721, 2005, pp. 1-13.
28. E.H. Yang, Y. Hishinuma, J.G. Cheng, S.T. McKinstry, E. Bloemhof, B. Martin Levine, " Thin-Film Piezoelectric Unimorph Actuator-Based Deformable Mirror with a Transferred Silicon Membrane ", *IEE Journal of Microelectromechanical Systems*, Vol. 15, Oct. 2006, pp. 1214-1225.
29. U. Hofmann et al, "Wafer-level vacuum packaged micro-scanning mirrors for compact laser projection displays", *Proc. of SPIE 2008*, Vol. 68-87, 2008, pp. 110-114.
30. M. Oldsen, U. Hofmann, H.-J. Quenzer, B. Wagner, "A Novel Fabrication Technology for Waferlevel Vacuum Packaged Microscanning Mirrors", *Proc. 9th Electronics Packaging Technology Conference*, 2007.
31. A. Selvakumar, K. Najafi, " Vertical Comb Array Microactuators ", *IEEE Journal of microelectromechanical systems*, Vol. 12, no. 4, Aug. 2003, pp. 440-449.
32. R.A. Conant, J.T. Nee, K.Y. Lau, R.S. Muller, "A Flat High-Frequency Scanning Micromirror", *Solid-State Sensor and Actuator Workshop Technical Digest*, 2000, pp 6-9 .
33. F. Battini, E. Volpi, E. Marchetti, T. Cecchini, F. Sechi, L. Fanucci, U. Hofmann, "A fast developing and low cost characterization and test environment for a double axis resonating micromirror", *Proc. of IWASI 2009*, 2009, pp. 25-26
34. F. D'Ascoli, M. Tonarelli, M. Melani, M. De Marinis, A. Giambastiani, L. Fanucci, " Intelligent sensor interface for automotive applications ", *Proc. of ICECS 2005*, Gammarth, Tunisia, Dec. 2005.
35. F. Iozzi, L. Fanucci, A. Giambastiani, " Fast prototyping flow for sensor interface ", *IEEE Ph.D. Research in Microelectronics and Electronics*, Otranto (Lecce), Italy, Jun. 2006.
36. L. Bacciarelli, "Platform-Based Design for Next Generation System on Chip for Sensor Interfacing and Conditioning", *PhD Thesis*, Chapter 5, 2009.
37. R. Neul et al, "Micromachined Gyros for Automotive Applications", *Sensors 2005 IEEE*, 2005, pp. 527-530.
38. K.B. Lee, Y.-H. Cho, " An electrostatic quality factor control for surface-micromachined lateral resonators", *Proc. of the Seventh International Symposium on Micro Machine and Human Science* , Oct 1996, pp. 143-147.
39. C.-I. Kang, C.-H. Kim, " An adaptive notch filter for suppressing mechanical resonance in high track density disk drives ", *Microsystem. Technology*, Vol. 11, 2005, pp. 638-652.

40. C. Jeong, S. Seok, B. Lee, H. Kim and K. Chun , " A study on resonant frequency and Q factor tunings for MEMS vibratory gyroscopes ", *Journal of Micromechanics and Microengineering*, Vol. 14, 2004, pp. 1530-1536.